RADIOSCIENCE LABORATORY

STANFORD ELECTRONICS LABORATORIES
DEPARTMENT OF ELECTRICAL ENGINEERING
STANFORD UNIVERSITY · STANFORD, CA 94305

MODIFICATION OF THE IONOSPHERE BY VLF WAVE-INDUCED ELECTRON PRECIPITATION

By

J.H. Doolittle

January 1982

Technical Report E4-21301318

Prepared under

Division of Polar Programs of the National Science Foundation
Grants NSF-DPP80-22282 and DPP80-22540

Atmospheric Sciences Section of the National Science Foundation
Grants NSF-ATM78-05746, ATM78-20967 and ATM80-18248

National Science Foundation contract to Utah State University
Subcontract Number SC-78-034

ABSTRACT

Very low frequency (VLF) waves propagating in the whistler mode in the magnetosphere are known to cause precipitation of energetic electrons at middle latitudes. The interactions between the waves and electrons trapped in the magnetic field are believed to occur through cyclotron resonance. As a monochromatic wave propagates along a field line, the condition for resonance can be satisfied by electrons of a minimum energy at the equator and higher energies at increasing latitudes. Resonant interactions occurring in a field aligned region extending several thousand kilometers on both sides of the equator can therefore result in a precipitation flux with a wide range of energies. Electrons which are scattered into the loss cone will collide with the constituents of the ionosphere, causing additional ionization, optical emissions, x-rays and heating.

A computational technique is introduced which allows the temporal shape of a pulse of precipitation to be modeled. A realistic energy distribution is used to weight the contribution to the total precipitation energy flux resulting from resonant interactions in each segment of the duct. Wave growth along the path is found to affect the shape of the pulse. In its simplest application, the model sets limits on the time window in which a precipitation event can occur. The model arrival times are shown to agree with experimental correlations of VLF waves and effects of precipitation occurring on three occasions, thus supporting the assumption that the precipitation results from cyclotron resonant scattering.

Various techniques that have been employed for detecting wave-induced precipitation are compared. A quantitative analysis of the use of an HF radar for this purpose is introduced, based on the changes in the phase and group paths of the radar signals that are reflected from the perturbed ionosphere. The effects are modeled by first using an ionospheric simulation program to compute the height profile of the electron density at consecutive steps in time. An additional term is introduced in the continuity equation to account for production due to corpuscular ionization. The refractive index height profile is then obtained and used to find the phase and group paths for vertically incident HF signals. Long enduring precipitation of 1 keV electrons with an energy flux of 0.01 erg per centimeter squared per second is found to cause noticeable changes in the group delay measured from an ionogram. For burst-like precipitation, the energy flux threshold for detection by the HF radar phase monitoring technique is determined to be about 0.002 erg per centimeter squared per second.

ACKNOWLEDGEMENT

This research was supervised by Professors R.A. Helliwell and D.L. Carpenter. The author is sincerely grateful for their continual support and encouragement. Their interest, advise and critical reading have helped shape the content of this work. Discussions with Drs. C.G. Park, P.A. Bernhardt and U.S. Inan have been important in defining the topic.

I wish to express deep appreciation to Professor J.P. Katsufrakis, through whom the opportunity of my involvement in this research was made possible. His coordination of the scientific activities at Siple Station, Antarctica and Roberval, Quebec has contributed materially to the successful observation of precipitation effects correlated with VLF wave events. Bill Armstrong collaborated with the author in acquiring the Siple photometric correlations discussed in chapter 3. I also wish to thank the other members of the 1977 Siple winterover crew, Peter Harding, Ron Marsh and Jim Logan, for their operational support.

I gratefully acknowledge the assistance of Bill Trabucco and Evans Paschal in designing parts of the photometer used to obtain correlations with VLF events at Roberval. I thank Richard Taillefer for operating the instrument in the field and Jerry Yarbrough for expert data processing. Satellite data has been provided through the courtesy of Dr. Gordon James of the Canadian Department of Communications.

I am particularly grateful to my wife Marie for her patience and dedication throughout the course of this work. The manuscript is largely the result of her diligence in mastering the skill of word processing. Thanks are also due to Stephenie Williams for drawing the

Various techniques that have been employed for detecting wave-induced precipitation are compared. A quantitative analysis of the use of an HF radar for this purpose is introduced, based on the changes in the phase and group paths of the radar signals that are reflected from the perturbed ionosphere. The effects are modeled by first using an ionospheric simulation program to compute the height profile of the electron density at consecutive steps in time. An additional term is introduced in the continuity equation to account for production due to corpuscular ionization. The refractive index height profile is then obtained and used to find the phase and group paths for vertically incident HF signals. Long enduring precipitation of 1 keV electrons with an energy flux of 0.01 erg per centimeter squared per second is found to cause noticeable changes in the group delay measured from an ionogram. For burst-like precipitation, the energy flux threshold for detection by the HF radar phase monitoring technique is determined to be about 0.002 erg per centimeter squared per second.

TABLE OF CONTENTS

TABLE OF CONTENTS (cont.)

TABLE OF CONTENTS (cont.)

LIST OF TABLES

ILLUSTRATIONS

ILLUSTRATIONS (cont.)

ILLUSTRATIONS (cont.)

ILLUSTRATIONS (cont.)

Chapter I

INTRODUCTION

This research examines the modification of the ionosphere by VLF wave-induced precipitation of energetic electrons from the magnetosphere. A calculational procedure is introduced which allows the temporal shape of a pulse of precipitation to be modeled. The model is applied to several sets of geophysical data which show a correlation between VLF waves and observed evidence of electron precipitation. A numerical simulation of the ionosphere is used to investigate the temporal change in the height profile of the electron concentration for various fluxes of precipitation. The simulation results then are used to predict the perturbations that wave-induced electron precipitation will cause to the group and phase heights of HF radar echoes.

A. The Magnetosphere

The phenomenon of wave-induced electron precipitation results from cyclotron resonant pitch angle scattering of electrons initially trapped in the magnetosphere. The magnetosphere is the region of space surrounding the earth in which the motion of charged particles is controlled by the planetary magnetic field. The shape of the magnetic field at distances up to about 6 earth radii (6 r_o) can be represented by a dipole located at the center of the earth. The dipole axis is tilted with respect to the spin axis by about 11.5 degrees. At greater distances the solar wind distorts the field so that it is no longer well described by a tilted dipole.

As the solar wind particles approach the earth's magnetic field,

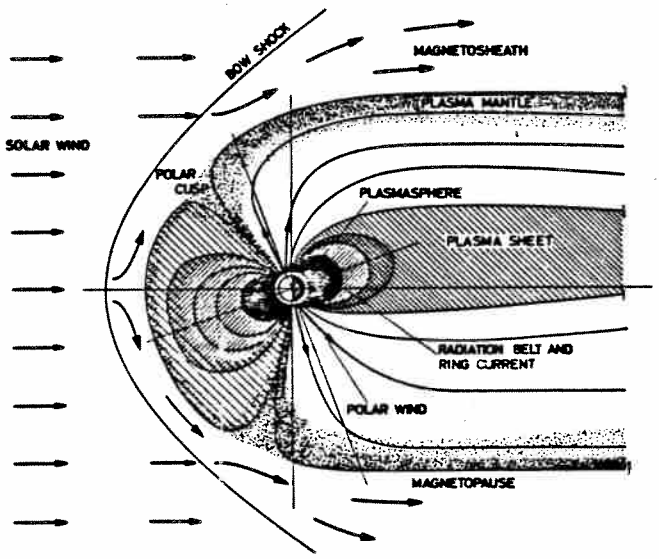

Figure 1.1 General configuration of the geomagnetic field shown in a noon-midnight meridian section (NASA, OPEN Mission Synopsis, February, 1979).

currents are induced which set up a boundary known as the magnetopause. In the direction towards the sun, the magnetopause has the approximate form of a hemispherical bow shock. It is located at a distance of about 10 to 12 r_o where the kinetic pressure of the solar wind equals the magnetic pressure of the earth's total magnetic field. In the anti-solar direction the field is swept by the solar wind into a long tail. The general configuration of the geomagnetic field is shown in a noon-midnight meridian section in figure 1.1.

In the inner magnetosphere where dipole geometry applies, a line of force in the magnetic field can be identified by the point where it crosses the magnetic equator. The parameter L describes the equatorial

radius (r_{eq}) of a field line in units of earth radii.

$$L = \frac{r_{eq}}{r_o} \tag{1.3}$$

A location on a dipole field line can be uniquely specified by giving the geomagnetic latitude (λ) and L or the geocentric distance (r) as shown in figure 1.2.

The magnetic field strength at any location is given by

$$B_o(r,\lambda) = 3.12 \times 10^{-5} \left(\frac{r_o}{r}\right)^3 (1 + 3 \sin^2\lambda)^{\frac{1}{2}} \quad \text{wb/m}^2 \tag{1.1}$$

where r_o = 6370 km. The distance from the dipole center to the point on

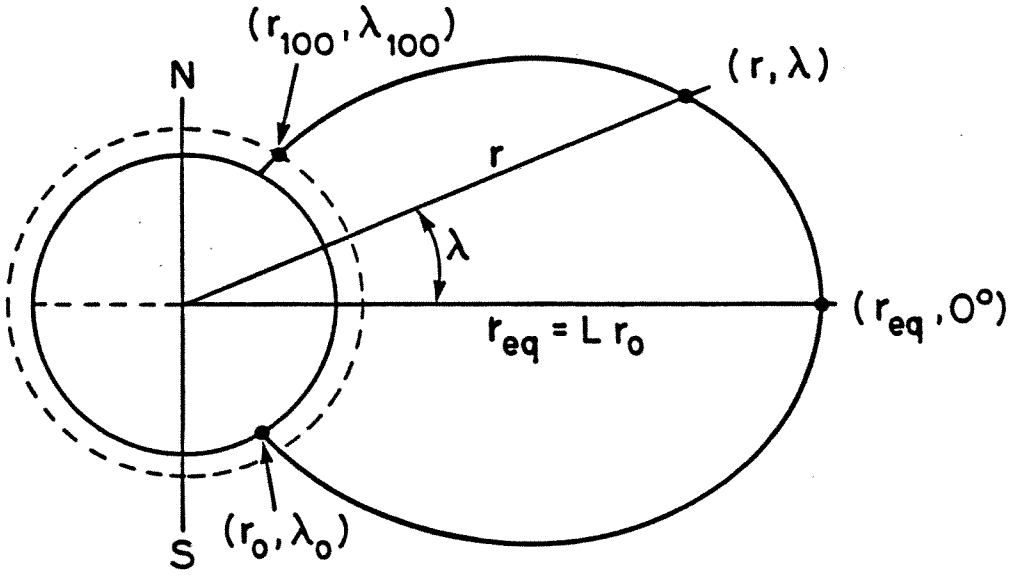

Figure 1.2 The geomagnetic coordinate system.

the field line as given by

$$r = r_o \left[\frac{\cos \lambda}{\cos \lambda_o} \right]^2 \qquad (1.2)$$

and λ_o is the latitude of the point where the field line intercepts the earth surface.

The particles which populate the magnetosphere are electrons and positive ions in a neutral mixture. The dominant ion is H^+, while smaller numbers of He^+ and O^+ are also present. The principal source of these particles is ionization of the neutral constituents of the atmosphere due to solar EUV radiation. During the daytime, particles flow upward into the magnetosphere. At night, in the absence of solar ionization, the net flow is from the magnetosphere to the ionosphere.

The magnetospheric plasma can be considered as occupying two distinct regions. In the inner magnetosphere, often called the plasmasphere, the plasma rotation closely follows the rotation of the earth. Plasmaspheric densities measured at the equator gradually decrease with increasing L. Under normal conditions a sharp density gradient known as the plasmapause (Carpenter, 1963) exists at about L=4. Inside the plasmapause densities are of the order of 10^3 cm^{-3}, while outside the plasmapause they are of the order of 10 cm^{-3}. The plasmapause can be more or less sharply defined, depending on geomagnetic conditions, but often the steep density gradient occurs within about 0.3 L. The location of the plasmapause during geomagnetic quiet conditions is often near L=5. During magnetic storms the outer portions of the plasmasphere tend to be convected away such that the

plasmapause moves inward to about L=3 (Carpenter, 1966).

The distribution of the cold plasma particles of energies less than a few electron volts (eV) within the plasmasphere can be modeled by assuming diffusive equilibrium in which the force of gravity and centripetal force acting on a unit volume equals the pressure gradient along the field line. Near the magnetic equator where the gravity gradient along the field line is small, the plasma density varies slowly. The variation of the cold plasma density with magnetic latitude is shown in figure 1.3 for the L=3, 4 and 5 field lines. Outside the plasmapause the densities are quite low and a collisionless plasma model better describes the distribution (Angerami, 1966).

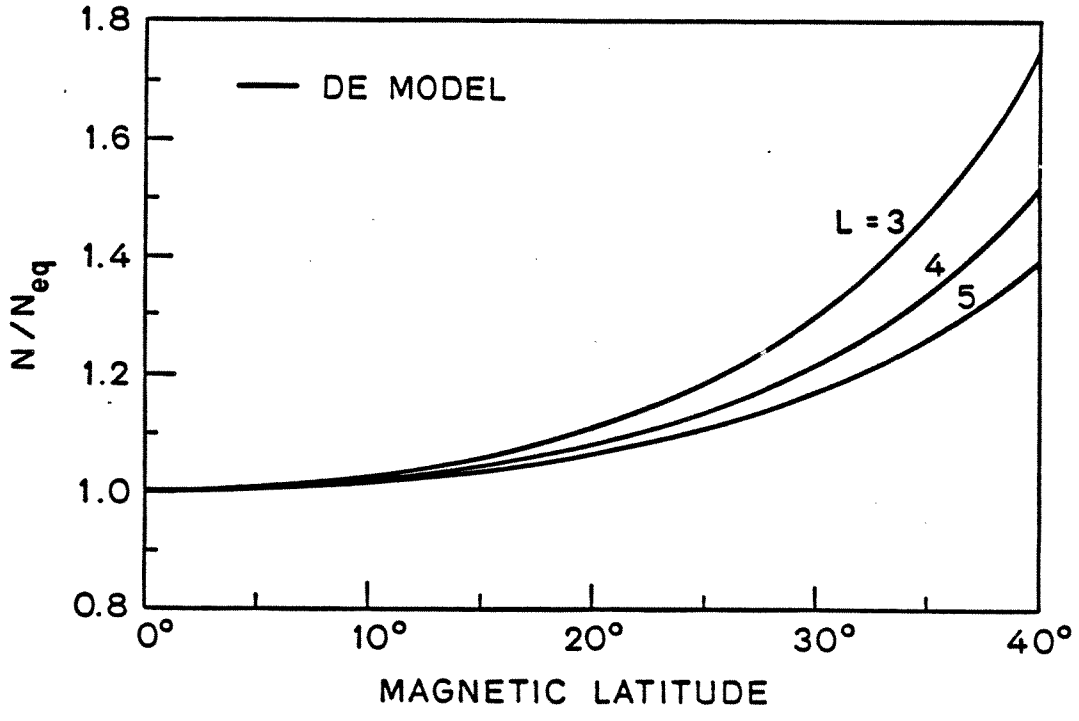

Figure 1.3 Variation of cold plasm density with latitude along field line

In addition to the cold plasma, fewer particles of greater kinetic energy (up to several MeV) also are present in the magnetosphere. While the cold plasma is important as a medium for VLF wave propagation, the more energetic particles can satisfy the conditions for cyclotron resonant interactions with VLF waves and therefore will be of great interest in this report

The charged particles in the magnetosphere move along the field lines in helical trajectories due to the Lorentz force ($\vec{F} = q\vec{v} \times \vec{B}_0$) which acts on them. The motion can be considered to be the sum of a translational component directed along the field line with a parallel velocity ($v_{\parallel}$) and a perpendicular component ($v_{\perp}$) which causes the particle to gyrate around the field line. The angular frequency of gyration (ω_H) and radius (r_H) of the circular motion both depend on the magnetic field strength B_0 and the particle mass (m) and are given by

$$\omega_H = \frac{qB_0}{m}$$

and

$$r_H = \frac{mv_{\perp}}{qB_0}$$

where q is the charge of the particle. As a particle spirals down the field line from the equator, the field strength increases. This causes the gyrofrequency to increase and the gyroradius to decrease. For a dipole field model, the gyrofrequency (kHz) of an electron is given by

$$f_H = 2\pi\omega_H = \frac{880(1 + 3\sin^2\lambda)^{\frac{1}{2}}}{L^3 \cos^6\lambda} \qquad (1.4)$$

The circular motion of a charged particle is equivalent to a current loop with a resulting magnetic moment of

$$\mu = \frac{mv_\perp^2}{2B_o}$$

where $\frac{1}{2}mv_\perp^2$ is the transverse kinetic energy. The magnetic moment can be shown to remain constant (e.g. Ratcliffe, 1972) as the field strength varies and therefore is refered to as the "first adiabatic invariant". An increase in field strength is therefore accompanied by an increase in the transverse velocity ($v_\perp$). Since the force exerted on the particle by the static magnetic field is perpendicular to the direction of motion, no work is done. The total kinetic energy will therefore be conserved,

$$E_{total} = \tfrac{1}{2}m\vec{v}^2 = \text{constant}$$

where

$$\vec{v} = \vec{v}_\parallel + \vec{v}_\perp$$

An increase in the transverse velocity is thus accompanied by a decrease in the longitudinal velocity. The field therefore affects the direction of the particle momentum while conserving the total energy. When the magnetic field strength is large enough to reduce the longitudinal velocity to zero, the translational motion is reversed and the particle spirals back up the field line with the same sense of gyration.

The location where the translational motion ceases is known as the "mirror point". Figure 1.4 shows that there are mirror points at

conjugate ends of a closed field line. Particles which spiral back and forth between conjugate mirror heights are said to be trapped.

The trajectory of a charged particle in the geomagnetic field can be described by (α_{eq}) the equatorial pitch angle. This is the angle between the total velocity vector and the field direction, measured at the equator. The pitch angle at any other location depends on the relative field strength and can be obtained from

$$\frac{\sin^2\alpha}{B_o} = \text{constant}$$

Thus the equatorial pitch angle associated with a given mirror point is given by

$$\sin^2\alpha_{eq} = \frac{B_{eq}}{B_m} \tag{1.5}$$

where B_{eq} and B_m are the equatorial and mirror point field strengths, respectively. The position of the mirror point depends on the distribution of the geomagnetic field and on the equatorial pitch angle of the particle. It does not depend on the particle mass or energy.

The equatorial pitch angle of a particle which mirrors at a height h_m is given by (Inan, 1977)

$$\sin^2\alpha_{eq} = \frac{(1 + \frac{h_m}{r_o})^3}{L^2\left[4L^2 - 3L(1 + \frac{h_m}{r_o})\right]^{\frac{1}{2}}} \tag{1.6}$$

For small pitch angles a particle will mirror at a height which may be located in the denser regions of the lower ionosphere. The probability

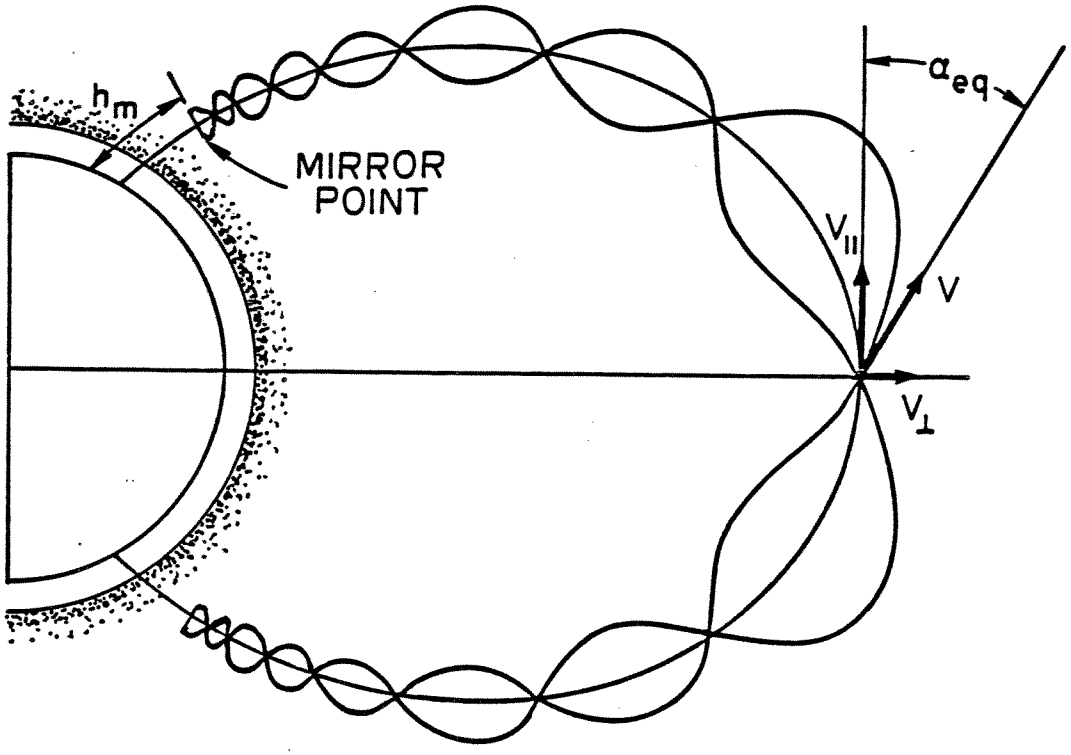

Figure 1.4 Spiral trajectory of particle trapped between conjugate mirror points.

for collisions with the atmospheric constituents will be greater there. A momentum change resulting from a collision may cause the particle to become untrapped. Such particles are said to have precipitated from the magnetosphere. It is reasonable to assume that any particle which penetrates to a height of 100 km will certainly be deviated by collisions. The equatorial pitch angle associated with a mirror height of 100 km can be used to define the "loss cone". Particles whose equatorial pitch angle is inside of the loss cone would mirror below 100 km. Since collisions are highly likely at such low heights, particles inside of the loss cone are removed from the trapped population.

In a study of the world contours of conjugate mirror point locations, Barish and Wiley (1970) pointed out that the mirror heights at conjugate ends of a field line can in some instances be quite different for a given pitch angle. The mirror height at Roberval, Quebec, for example, is about 300 km higher than at the conjugate point at Siple station. Thus the Roberval loss cone lies inside of the Siple loss cone.

The distribution in energy of the number density (cm^{-3}) of the trapped population of electrons, measured at the equator, can be expressed by the inverse power function

$$f_{eq}(E) = A\ E^{-p} \qquad cm^{-3} \qquad (1.6)$$

Measurements of typical spectrums (e.g. Schield and Frank, 1970; Westerlund, 1969) show general agreement to the power law when p=2.

B. The Ionosphere

The ionosphere is the region of the atmosphere where sufficient numbers of free electrons exist such as to influence the propagation of radio waves. Historically the term ionosphere has included everything above about 60 km. As space science has evolved, however, it has become useful to further divide the regions of the earth's atmosphere. The ionosphere can be divided into regions in which various processes dominate. These are usually refered to as the D (60-90 km), E (90-130 km), F_1 (130-200) and F_2 (above 200 km) regions. We shall refer to the region above about 500 km as the plasmasphere. The dominant ionic

species in the plasmasphere is H^+ and thus the region is sometimes also called the protonosphere. The plasmasphere continues to about L=4 where a steep gradient in the plasma density is found at the plasmapause.

The term magnetosphere is used to describe the entire region of planetary space where the motion of charged particles is dominated by the force exerted by the geomagnetic field. Below a height of about 250 km, collisions have an increasing effect on the motion of ions and electrons, thus the term inner magnetosphere refers to the upper ionosphere and the plasmasphere. The outer magnetosphere generally refers to the region between the plasmapause and the magnetopause.

Solar EUV radiation absorbed by the neutral constituents of the upper atmosphere results in molecular dissociation, ionization, optical emissions and heating. The rate at which these effects occur depends on the intensity of the radiation and concentration of the atmospheric gases. The height profile of the free electron density reaches a maximum at about 300 km. Less ionization occurs above that height because the density of the neutral atmosphere is small. Below the maximum, the intensity of the solar radiation is reduced because of the effect of absorption in passing through the overlying layers.

Particle bombardment of the upper atmosphere also results in ionospheric effects similiar to those caused by solar EUV radiation. Energetic protons and electrons which penetrate the ionosphere may have come from the distant reaches of the galaxy (i.e. cosmic rays) or from solar flares. Another source which is of particular interest in this report is the precipitation of energetic particles from the trapped population in the magnetosphere. Corpuscular ionization is usually

several orders of magnitude less than that caused by solar radiation, yet at night it can be important.

The processes of ionization and optical emissions are similar in that they both result from the excitation of ionospheric atoms and molecules. Some of the radiative (solar EUV) or kinetic (corpuscular) energy absorbed by the atom or molecule is imparted to the outermost electron. Ionization occurs if the absorbed energy is greater than the minimum ionization potential. Energy in excess of the minimum ionization potential is shared as kinetic energy between the ion and freed electron and has the effect of heating the plasma. If the absorbed energy is less than that needed for ionization, then the outermost electron may be excited to a higher energy quantum state. Again, the energy absorbed in excess of that required for the quantum state transition will result in plasma heating. Electrons orbiting in unstable excited states will eventually make a spontaneous quantum transition to some stable lower energy state. The average time that the atom or molecule remains in the excited state is refered to as the state lifetime. Excited state life times for the principal ionospheric auroral transitions are shown in table 1.1.

The quantum energy given up by the orbiting electron during the transition is emitted as a photon of light. The total integrated columnar intensity of auroral optical emissions observed from the ground depends both on the energy flux (erg cm^{-2} s^{-1}) and the energy spectrum of the particles penetrating the ionosphere. Typical intensities during a medium-to-bright (IBC 2-3) aurora are shown relative to the brightness of the atomic oxygen line at 5577 Angstroms in table 1.1.

Table 1.1 PRINCIPAL AURORAL EMISSIONS

Atomic or Molecular Species	Emission Wavelength (Angstroms)	Relative Intensity I/I_{5577}	Excited State Lifetime	Suitability for Detection of Transient Events
N_I	3466	1.2 *	12 s **	too slow
N_2^+	3914	1.5 *	14 μs **	fast and strong
N_2^+	4278	0.4 *	70 ns **	fast
O_I	5577	1.0 *	0.7 s **	strong, but slow
O_I	6300-6364	0.4 *	110 s **	too slow
O_{II}	7319-7330	0.1 *	5 s **	too weak
O_I	7774	0.1 **	---	too weak
O_I	8447	0.1 **	---	too weak
N_I	8680	0.1 **	---	too weak

* D.R. Bates, 307-310, 1960.
** A.V. Jones, 86-119, 1974.

Optical emissions resulting from wave-induced electron precipitation have been observed with durations of the order of a few seconds (Helliwell et al., 1980). Since excited state lifetimes are statistical averages, long lifetimes will result in a spread in time of the optical response to a burst of precipitation. Species with long lifetimes therefore would not be suitable for detecting transient events. Emission of weak relative intensity would also be less suitable for that purpose. A comparison of these factors for the various species in table 1.1 suggests that the Meinel transition of N_2^+ at 3914 Angstroms would be the best choice for optically detecting wave-induced

electron precipitation. However, optical interference filters at such short wavelengths tend to have low transmission coefficients (S.B. Mende, private communications) and thus emissions from the first negative transition of N_2^+ at 4278 Angstroms are more easily detected.

The radiance of an auroral emission is measured in units called Rayleighs, R, (Hunten, Roach and Chamberlain, 1956), whereby

$$1\ R = 10^6\ \text{photons cm}^{-2}\ \text{s}^{-1}\ \text{sphere}^{-1}$$

The threshold of visual detection of auroral emissions at 5577 Angstroms is about 10^3 R or 1 kR (Omholt, 1971).

C. Wave-Induced Electron Precipitation

Precipitation of an energetic electron from the magnetosphere will occur whenever the particle's pitch angle falls inside the loss cone. The equatorial value of the pitch angle will remain constant until a perturbing force acts on the electron. A source of perturbation exists in the magnetosphere in the form of electromagnetic waves which can alter the trajectories of trapped electrons through cyclotron resonance interactions (e.g. Thorne, 1975).

The refractive index in the magnetosphere varies with direction. At very low frequencies this anisotropy is such that the direction of energy flow, or ray path, tends to follow the magnetic field line. Field-aligned density enhancements, or ducts, which extend between conjugate ends of a field line can further constrain the wave. Trapping of a VLF wave in an enhancement duct can occur if the wave normal makes

a sufficiently small angle with respect to the field direction and the wave frequency is less than half of the local electron gyrofrequency ($f/f_H < 0.5$). Propagation of a whistler-mode wave in a duct is analogous to the guiding of light in an optical fiber. Cyclotron resonance can occur when the doppler shifted frequency of a circularly polarized wave, as seen in the particle frame of reference, is equal to the electron gyrofrequency. The resonance condition is described in detail in chapter 2.

Observations at mid-latitudes ($L \simeq 4$) have shown that discrete bursts of electron precipitation can be found in association with whistlers and whistler triggered VLF emissions. As an example, one-to-one correlations between discrete bursts of triggered emissions and x-rays were first observed by Rosenberg et al. (1971) using a balloon-borne detector launched from Siple station, Antarctica. Similar observations have been made at the Siple conjugate point at Roberval, Quebec (Rosenberg et al., 1981). Correlations have also been made between whistler events and bursts of ionospheric optical emissions (Helliwell et al., 1980; Doolittle, 1980). In another experiment, Helliwell et al. (1973) observed perturbations in the amplitude of VLF signals propagating in the earth-ionosphere wave guide in direct correlation with whistlers. These phenomena were attributed to precipitation resulting from scattering of energetic electrons into the loss cone through magnetospheric cyclotron resonance interactions with whistler mode waves near the equator.

D. Detector Sensitivities

Precipitation of energetic electrons from the magnetosphere can cause additional ionization, optical emissions, bremsstrahlung x-ray emissions and heating in the ionosphere. Various techniques are available for observing the effects of wave-induced electron precipitation. In this section we will consider the sensitivity of some of these and then express this in terms of the minimum precipitation energy flux which would be detectable with each technique. The results are summarized in table 1.2 in order of increasing sensitivity.

Wave-induced electron precipitation will generate ionization and optical emissions over an extended vertical column in the ionosphere. As an electron penetrates into the upper atmosphere it loses kinetic energy through repeated collisions with the ionospheric constituents. It becomes most effective in producing ionization or optical emissions at the end of its path when the time spent near an atom is comparable to the period of the outermost Bohr orbit. Higher energy particles will penetrate further than lower energy particles. The vertical distribution of ionization or optical emissions will therefore depend on the energy spectrum of the precipitation flux.

Optical observations usually measure the integrated brightness of an entire column of emissions. Precipitating electrons with initial energies in the range of about 0.1 to 500 keV will contribute to the observed brightness. If the total brightness exceeds about 1000 Rayleighs, then the event should be just visible to the unaided eye (Omholt, 1971). The emission rate of 4278 Angstrom radiation per unit incident energy flux is about 200 Rayleighs per erg cm^{-2} s^{-1} (Rees and

Table 1.2

MINIMUM PRECIPITATION ENERGY FLUX
DETECTABLE BY VARIOUS TECHNIQUES

Detector	Instrumental Threshold	Energy Range (keV)	Precipitation Energy Flux Threshold ($erg/cm^2/sec$)	Reference
Human eye	1000 Rayleighs	0.1 - 500	5.0	A. Omholt, Optical Aurora
Photography	500 Rayleighs	0.1 - 500	2.5	A.V. Jones, Aurora
Rocket particle scintillation detector	0.006 $erg/cm^2/s$ per steradian	0.08-500	3.8×10^{-2}	J.K. Hargreaves and R.D. Sharp Planet. Space Sci., 13, 1171, 1965
Photometer 4278 Å	5 Rayleighs	0.1 - 500	2.5×10^{-2}	S.B. Mende, private communications
Balloon X-ray scintillation detector	0.25 photons/cm^2/s	>30	5.0×10^{-3}	T.J. Rosenberg et al., J. Geophys. Res., 76, 130, 1971.
Riometer	0.02 dB	>30	2.5×10^{-3}	Rosenberg, op cit., Hargreaves and Sharp, op cit.
Kinesonde Phase	45 degrees/s	0.1 - 100	2.0×10^{-3}	This report, Chapter 6
SEEP satellite particle detector	1.6×10^{-5} $erg/cm^2/s$ per steradian	3 - 30	1.0×10^{-4}	U.S. Inan, SEL Tech. Report, E477-1, 1981

Luckey, 1974) for a maxwellian distribution of precipitating electrons with a peak energy of about 5 keV. The precipitation energy flux threshold for visual detection is therefore about 5 erg cm^{-2} s^{-1}.

Photographic film is about twice as sensitive as the human eye (Jones, 1974) for exposure times of the order of a few seconds. Photoelectric photometers and image intensifiers give a gain of about 100 over photography (Jones, 1974). Instrumental thresholds of the order of 5 Rayleighs (S.B. Mende, private communications) allow these devices to detect precipitation energy fluxes down to about 2.5×10^{-2} erg cm^{-2} s^{-1}.

Electrons of energies greater than about 30 keV penetrate to heights below 100 km where they produce bremsstrahlung x-rays. Since x-rays are absorbed by the lower atmosphere, it is necessary to use balloon-borne detectors to observe them. Typical scintillation detectors have sensitivities of about 0.25 x-ray photons cm^{-2} s^{-1}. A detector used by Rosenberg et al.(1971a) had a precipitation energy flux threshold of about 5×10^{-3} erg cm^{-2} s^{-1}.

Ionization in the D region causes absorption which can decrease the received amplitude of HF radio noise generated by cosmic sources. A riometer is an instrument which measures the relative ionospheric opacity by monitoring cosmic noise absorption (CNA). Riometers often have sensitivities of about 0.02 dB and can detect energy fluxes down to about 2.5×10^{-3} erg cm^{-2} s^{-1} for electrons of initial energy greater than 30 keV (Rosenberg et al., 1971a).

Precipitation of electrons with energies greater than about 100 keV can cause an increase in the D region ionization which perturbs the

amplitude of VLF waves propagating in the earth-ionosphere wave guide (Helliwell et al., 1973). While the energy flux is not known, a value of 0.03 erg cm^{-2} s^{-1} has been inferred (Dingle and Carpenter, 1981) by analogy to observations of x-rays correlated with VLF waves.

In situ measurements of precipitation can be made by rocket and satellite particle detectors. A rocket-borne detector described by Hargreaves and Sharp (1965) was sensitive to initial energy fluxes greater than about 4×10^{-2} erg cm^{-2} s^{-1}. A much more sensitive particle detector is planned for the SEEP satellite. It will be sensitive to precipitation of 3-30 keV electrons with energy fluxes of the order of 10^{-4} erg cm^{-2} s^{-1} (Inan, 1981).

The ionization in the E and F regions produced by precipitation can also affect the propagation of HF radio waves. In chapter 6 of this report we investigate the sensitivity of monitoring the phase of a fixed frequency sounder signal. It is found that the energy flux threshold for detection of precipitation using that technique is about 2×10^{-3} erg cm^{-2} s^{-1}.

E. Contributions of the Present Work

We have modeled the relative arrival time of VLF waves and wave-induced electron precipitation at the foot of the field line. While previous studies had considered scattering which occurred only at the equator (e.g. Rosenberg et al., 1971), we have included interactions in an extended region along the entire field line. The results demonstrate that electrons in a range of energies which are scattered into the loss cone at slightly different times over the extended

equatorial region can converge on the ionosphere in a short interval of time.

A procedure is developed to calculate the shape in time of the precipitating energy flux. The results predict for the first time the temporal relationship between precipitation events occurring at conjugate ends of the field line. A comparison of the temporal behavior of the energy fluxes due to precipitation by the direct and mirrored modes at the wave echo site shows that the two modes usually occur at about the same time. The July 24, 1977 correlation of optical emissions and whistlers recorded at Siple station, which were previously attributed to the direct mode of precipitation (Helliwell et al., 1980), can now also be explained by mirrored precipitation. The latter is consistent with the model adopted to explain the January 2, 1971 correlation between x-rays and chorus bursts at Siple station.

At the wave injection site the direct and mirrored precipitation fluxes are widely separated in arrival time. In order to determine which mode is dominant, we have built and operated a photometer at Roberval, Quebec. Observations on August 30, 1979 provided the first evidence of optical emissions correlated with VLF waves at the wave injection site. These results conclusively demonstrate that direct precipitation is the observed mode. The August 30, 1979 Roberval, and re-evaluated July 24, 1977 Siple, photometer cases support the indication given by x-ray data (Rosenberg et al., 1971; Rosenberg et al., 1981) that precipitation observed at either end of the field line can be attributed to scattering during the first pass of the wave through the interaction region.

We have modified an existing ionospheric simulation program to include additional production of ionization due to electron precipitation. For 1 keV electrons, the results show that the energy fluxes of the order predicted by Inan et al. (1977) can cause significant ionization enhancements in the F_1 region. Time constants and saturation densities for the buildup of ionization at 170 km height due to 1 keV electron precipitation at night are determined as a function of energy flux. The decay of ionization after an enhancement by 1 keV electron precipitation is found to proceed at a faster rate than the normal diurnal decay after sunset. The difference is explained by diffusion and transport associated with the localization of the ionization enhancement. The determination of the rates of buildup and decay of ionization are important for designing experiments to detect modifications of the F region induced by VLF transmitters.

We examine the possibility of detecting precipitation effects using a ground based HF radar. F region density enhancements which build up and decay over periods of several minutes, due to slow changes in the activity of scattering VLF waves, are found to cause detectable changes in ionograms. For transient events, the phase of an HF radar signal is found to give a very sensitive means of detecting modifications of the ionosphere. We have estimated an energy flux threshold of about 0.002 erg cm^{-2} s^{-1} for the detection of 1 keV electron precipitation using the phase monitoring technique.

Chapter II

TRANSIENT PRECIPITATION FLUXES

A. Introduction

In this chapter we examine cyclotron resonance between a whistler mode wave and energetic electrons under various conditions of cold plasma density on different field lines. Our purpose is to determine the relative arrival times at the ionosphere of electrons scattered in an extended region near the magnetic equator and to sum all simultaneous components of the precipitation energy flux to obtain the pulse shape as a function of time. These results can be useful for interpreting observations of precipitation events. They also suggest a method of detection whereby a sensor can filter the characteristic signals out of a noisy background. In its simplest application, the arrival time results serve to set limits on the time window in which a precipitation event can be expected to be observed in the ionosphere following the injection of a natural or man-made VLF wave.

A calculation of the total precipitation energy flux as a function of time requires a detailed modeling of the momentum changes experienced by all resonant electrons. The results of such models are dependent on the electron energy and pitch angle distribution and on the wave intensity. The numerical technique of following statistically meaningful numbers of particles is costly in terms of computer time, yet necessary if absolute magnitudes of the loss cone energy flux are to be determined. The approximate shape of the precipitation pulse due to

scattering by monochromatic waves, however, can be obtained more directly by making some simplifying assumptions about the population of electrons which will be scattered. The flux from each segment of the interaction region can then be normalized such that the energy flux as a function of time can be expressed in relative units. Thus the shape of transient loss cone flux pulses can be compared for various conditions without resorting to the full numerical model.

B. Cyclotron Resonant Interactions

The assumed mechanism which results in pitch angle scattering of energetic trapped electrons is cyclotron resonance. Since propagating whistler waves are of a right-handed polarization, resonance occurs through a normal doppler shift mode in which electrons and waves travel in opposite directions. The wave frequency (f) as seen in the electron frame of reference (i.e. doppler shifted) must equal the electron gyrofrequency (f_H) in order for a momentum perturbation to occur, thus

$$f = f_H - \frac{v_{\parallel}}{\lambda}$$

where $v_{\parallel}$ is the longitudinal component of the electron velocity and $v_{\parallel} < 0$

λ is the wavelength

Solving for $v_{\parallel}$,

$$v_{\parallel} = \lambda (f_H - f)$$

Now $\lambda = v_p / f$, where v_p is the phase velocity,

thus

$$v_{\parallel} = v_p \frac{(f_H - f)}{f} \tag{2.1}$$

Assuming quasi-longitudinal propagation of the whistler mode wave, the dispersion relation obtained from the Appleton-Hartree equation is

$$n^2 = 1 - \frac{X}{1 \pm Y_L} \tag{2.2}$$

where n is the index of refraction

$X = (\frac{f_o}{f})^2$

$Y_L = (\frac{f_H}{f}) \cos \theta$

f_o is the plasma frequency = $9 N^{\frac{1}{2}}$ (kHz)

θ is the angle between the wave normal and the magnetic field

N is the electron density (cm^{-3})

For whistler mode waves the lower sign is associated with the propagating mode. If the waves are ducted by field-aligned density enhancements, then θ is very small and the dispersion relation becomes

$$n^2 = 1 - \frac{f_o^2}{f(f - f_H)} \approx \frac{f_o^2}{f(f_H - f)}$$

since $f_o^2 >> f_H^2$. The phase velocity then can be written as

$$v_p = \frac{c}{n} = c \frac{f^{\frac{1}{2}}(f_H - f)^{\frac{1}{2}}}{f_o}$$

where c is the speed of light.

Using this expression in equation (2.1), the parallel resonant velocity

becomes

$$v_{\parallel} = c \frac{(f_H - f)^{3/2}}{f_o f^{\frac{1}{2}}} \tag{2.3}$$

Since the gyrofrequency and plasma frequency are dependent on the coordinates (L, λ) of the interaction point, the electron parallel resonant velocity for a given wave frequency will also vary along the field line.

The longitudinal component of the electron kinetic energy at resonance, including the relativistic correction, can be expressed as

$$E_{\parallel res} = m_o c^2 \left\{ \frac{1}{\left[1 - \left(\frac{v_{\parallel}}{c}\right)^2\right]^{\frac{1}{2}}} - 1 \right\}$$

where m_o is the rest mass (511.006 keV/c^2). Solving this expression for $v_{\parallel}$ and equating with equation (2.2), we obtain

$$0 = f^3 - 3f^2 f_H + 3f f_H^2 + f f_o^2 \left\{ 1 - \left[\frac{m_o c^2}{E_{\parallel res} + m_o c^2}\right]^2 \right\} \tag{2.4}$$

The resonant frequency for a normal doppler shifted cyclotron resonant interacton can be obtained by solving this cubic expression when $E_{\parallel res}$, λ, L and N are specified.

The effect of varying the parallel resonant energy is shown in

figure 2.1 where the cubic is solved for the L=4.2 field line for an equatorial density of 100 cm^{-3}. The plots show resonant frequency as a function of parallel resonant energy, parametric in latitude. The "height of penetration" of the energetic electrons into the ionosphere is given in the figure to show the region of maximum ionization produced by monoenergetic precipitation, as described in chapter 4. The following features can be seen:

1) For electrons for any given $E_{\parallel res}$ the resonant frequency is minimum at the equator and increases with latitude.

2) At any latitude along the field line, higher energy electrons interact with lower frequencies.

3) As a monochromatic wave propagates along the field line it can resonate with electrons of increasing energies at increasing latitudes.

C. Electron Arrival Times

This last result is of particular interest when consideration is given to the time at which precipitated electrons arrive at the ionosphere. As a monochromatic VLF wave moves from the equator to higher latitudes it can resonate with electrons of greater parallel kinetic energies. While these electrons travel faster, those resonating near the equator are scattered earlier and with less distance to travel before arriving at the ionosphere. Thus a situation exists in which the faster electrons scattered later can catch up with the slower ones scattered earlier. An "arrival time convergence" can exist at the foot of the field line whereby electrons in a range of energies arrive together after being scattered in a 20,000 to 30,000 kilometer region

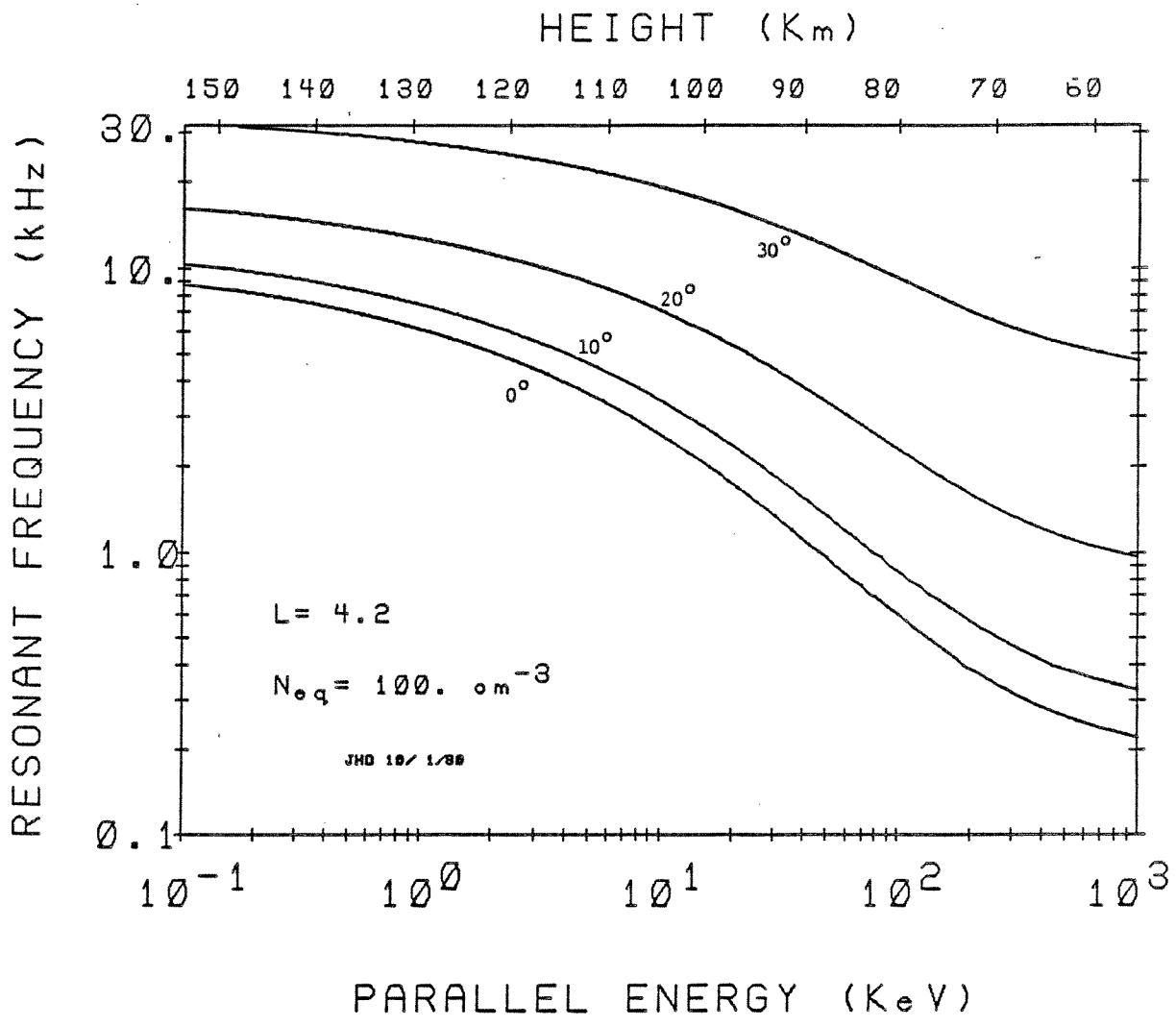

Figure 2.1 Resonant frequency as a function of parallel energy, parametric in latitude for L=4.2, N_{eq}=100 cm^{-3}

centered on the equator.

To determine the absolute magnitude of the precipitation energy flux as a function of arrival time at the ionosphere it is necessary to apply a detailed analysis of the physics of wave particle resonant scattering (e.g. Inan et al., 1978). However the approximate temporal response of a detector to the burst-like precipitation associated with

discrete VLF wave events can be found more directly by using a simplified model which assumes that precipitation results only from scattering of trapped electrons which are initially close to the edge of the loss cone. This assumption is appropriate to linear cyclotron resonant scattering by waves of field strengths less than about 7 milligamma (Inan, 1977). In the following analysis we define a mirror height of 100 km as corresponding to the edge of the loss cone and examine the precipitation of electrons which, prior to pitch angle scattering by a wave, initially mirrored at 1000 km. From equation 1.5 we see that the corresponding change in equatorial pitch angle at L=4.2 is about one degree, consistent with linear scattering theory.

The time of arrival at the ionosphere for a precipitating electron of a given energy as measured with respect to the time at which the wave was injected, is found by simply adding the time required for the wave to propagate to the point where the resonance condition is satisfied plus the time of flight for the scattered electron to reach the bottom of the field line. Once the wave frequency, equatorial field line radius and cold plasma density are specified, the wave and particle travel times can be found for any resonance point.

We have seen from equation 1.6 that a typical energy spectrum for trapped electrons follows a power law distribution. The energy spectrum for electrons scattered into the loss cone will be similar except that it will be modified by terms which account for the scattering efficiency of a perturbing wave. Since the relative number of particles diminishes as the energy per particle increases for a distribution which follows an inverse power law spectrum (see figure 2.2), the greatest

contribution to the total precipitation energy flux is made by low energy electrons. Figure 2.1 shows that for a monochromatic wave the more abundant lowest energy electrons resonate at the equator, while off-equator interactions with the same wave scatter less abundant electrons of higher energies. Thus the contribution to the total precipitation energy flux is greatest at the equator and falls off with increasing latitude. If we neglect energies greater than 100 keV then the typical interaction region is limited to about 20 to 30 degrees in latitude on either side of the equator. The equatorial distribution of the electrons which we will consider to be available for scattering into the loss cone is shown in figure 2.2 where the pitch angle dependence is chosen to be isotropic for simplicity.

A computational simplification is provided by considering as significant only those interactions which can occur in a region limited to 30 degrees about the equator. The wave group velocity is inversely proportional to the cold plasma density.

$$v_g = 2\,c\,\frac{f^{1/2}(f_H - f)^{3/2}}{f_o f_H}$$

where $f_o = 9\,N^{1/2}$

If it were necessary to integrate the wave group velocity from the source to the interaction point in order to find the propagation delay then the results would become quite sensitive to uncertainties in the

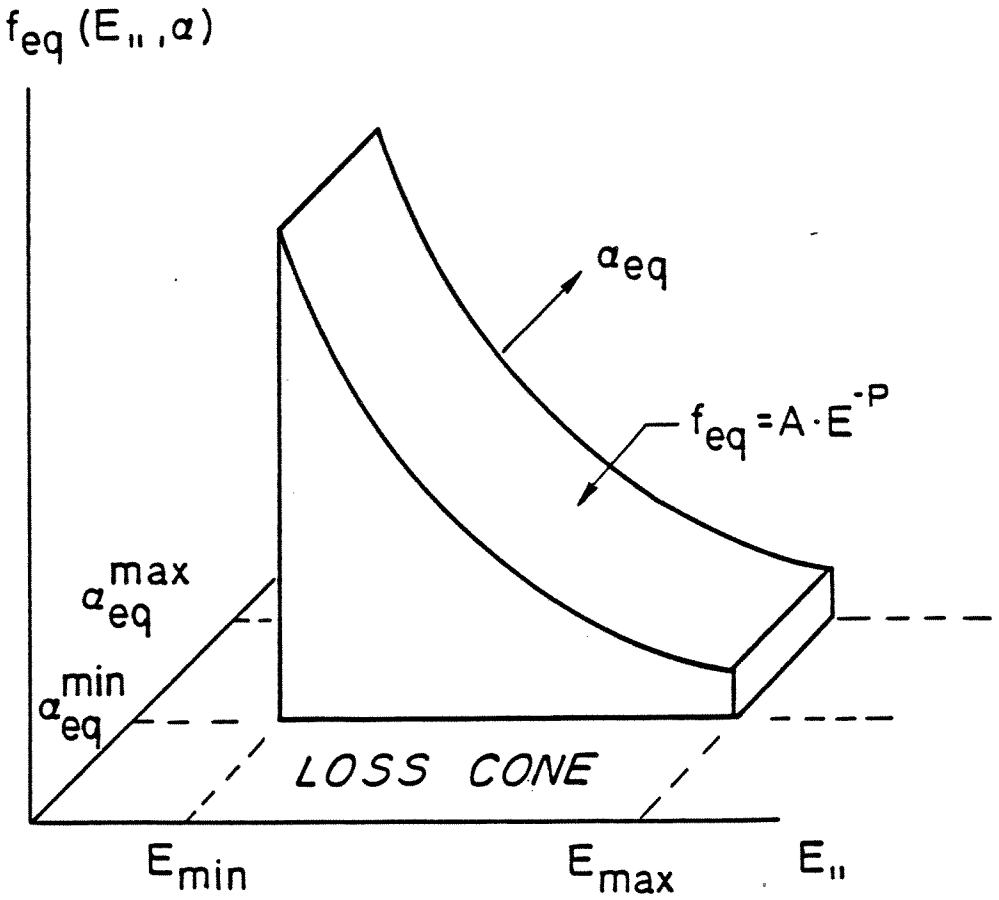

Figure 2.2 Equatorial distriburtion of electrons available for scattering into the loss cone

medium. This is particularly true close to the ionosphere where the cold plasma density shows a large gradient. In the equatorial region, on the other hand, the medium is slowly varying as can be seen in figure 1.3. The wave group velocity will therefore also be slowly varying near the equator, thus the group delay between the equator and an interaction point can be determined with confidence through integration. Assuming symmetry, the half-hop group delay to the equator can be found using an empirically derived method. The delay (t_w) to any point near the equator can then be found by correcting the half-hop delay (t_{hop}) by the propagation time between the equator and the interaction point.

$$t_w = \frac{t_{hop}}{2} \pm \int_s \frac{ds}{v_g}$$

where s is the distance from the equator to the interaction point. The sign of the correction will depend on whether the wave reaches the interaction point before (-) or after (+) passing the equator.

For a centered dipole magnetic field model with a constant density distribution, an empirical expression for the one-hop group delay has been derived by Smith (eq. 5.13, 1960), where the nose frequency is assumed to be one-third of the equatorial gyrofrequency. Through application of further formulation described by Park (1972) the one-hop group delay for a whistler mode wave is given in seconds by

$$t_{hop} = t_n \left\{ \frac{2(\frac{f_n}{f})^{\frac{1}{2}}}{3(1 - \frac{f}{3f_n})} \right\}$$

where f is the resonant wave frequency

f_n is the nose frequency $\approx f_n'(1 + \gamma(D_{ci}/t_n f'^{1/3}))$

D_{ci} is the dispersion (typically 5 at night)

and t_n is the one-hop travel time at f_n

$$t_n \approx t_n' + \frac{D_{ci}}{f_n'^{\frac{1}{2}}}$$

where

$$t_n' = \left[\frac{N_{eq} L^5}{C_1 f_n'} \right]^{\frac{1}{2}}$$

$$f_n' = \frac{f_{Heq}}{C_2}$$

$$f_{Heq} = \frac{8.74 \times 10^5}{L^3} \text{ Hz}$$

For a diffusive equilibrium model,

$\gamma = 0.17$

$C_1 = 24$

$C_2 = 2.7$

For a collisionless model,

$\gamma = 0.15$

$C_1 = 10$

$C_2 = 2.3$

Calculated one-hop delays as a function of frequency for L=4.2 and various cold plasma densities show the familiar whistler dispersion in figure 2.3 for the diffusive equilibrium and collisionless plasma models.

The time of flight (t_e) for a scattered electron to travel from a resonance point to the foot of the field line is also most easily found by making a correction for off-equator interactions. The flight time from the equator is simply one half of the bounce period. The bounce period (T_e) is given by a linear approximation (Hamlin et al., 1961) as

$$T_e = \frac{4Lr_o}{v}(1.30 - 0.56 \sin\alpha_{eq})$$

where $r_o = 6371$ km

v is the total velocity of the electron

α_{eq} is the electron equatorial pitch angle

The correction to the flight time is found by integrating the parallel

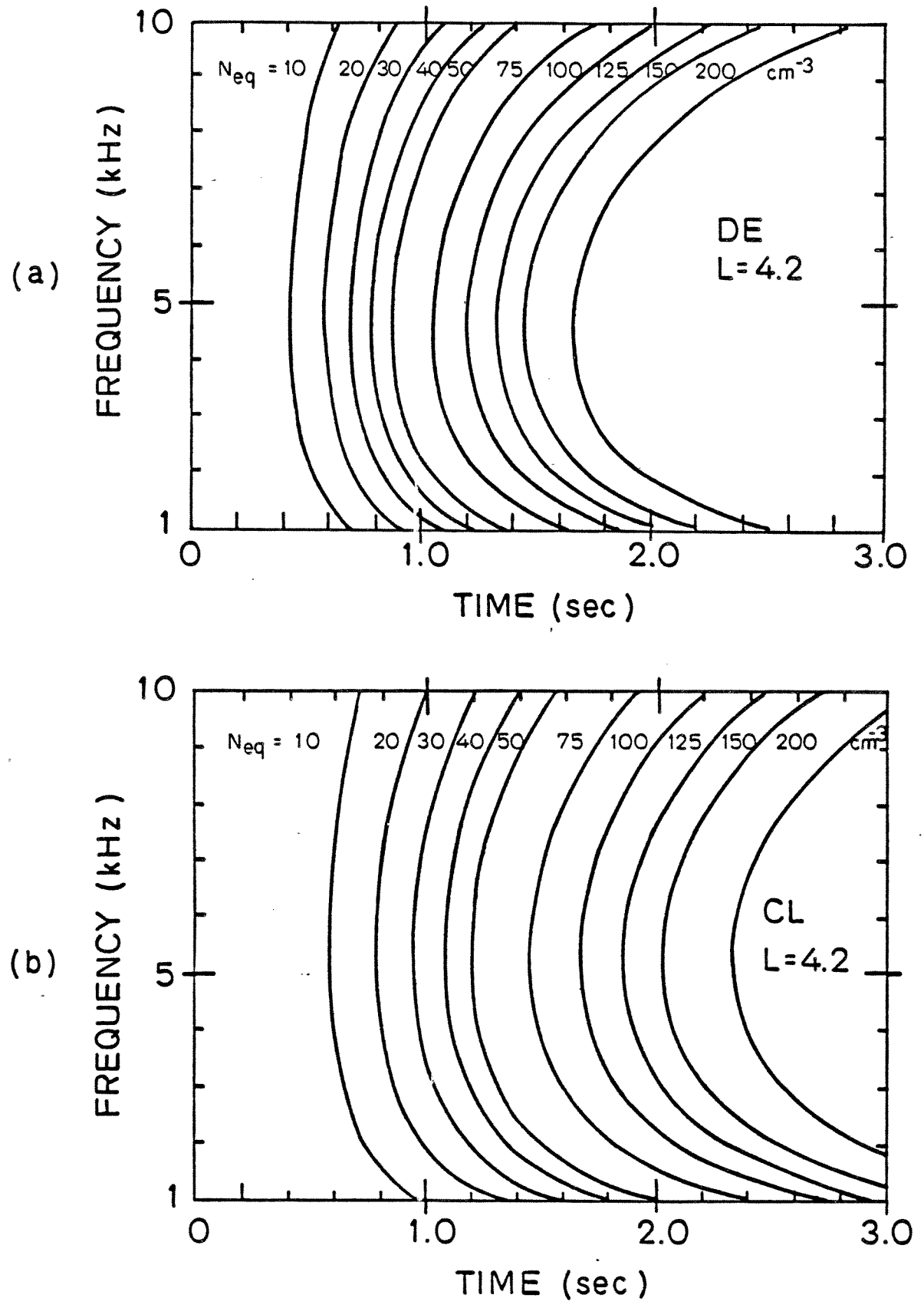

Figure 2.3 Whistler one-hop delays for L = 4.2, Neq = 10 to 200 cm^{-3} for a) diffusive equilibrium and b) collisionless plasma models.

velocity of the electron between the equator and the interaction point. Thus the time of flight for the electron becomes

$$t_e = \frac{T_e}{4} \pm \int_s \frac{ds}{v_{\parallel}}$$

The arrival time calculations proceed by adding the time for the wave to reach the interaction point to the time of flight for the electron to reach the foot of the field line. The model considers precipitation at both ends of the field line, i.e. the wave injection site and the wave echo site. At each site the arrival times are determined for 1) the case in which the electrons are directly precipitated after scattering in the equatorial region, and 2) the case in which the scattered electrons travel to the conjugate mirror point before making a final bounce. The latter case could result from either an asymmetry in conjugate mirror heights (Barish and Wiley, 1970) or from backscatter which has been estimated to be as much as 10 percent of the downward flux (Davidson and Walt, 1977). The cases of direct and mirrored precipitation are shown diagramatically for both ends of the field line in figure 2.4. For interactions occurring on the equator, the electron arrival times at the ionosphere result from the sum of either 1/2 or 3/2 wave hops and 1/2 or 3/2 electron bounces. The corrections to both the wave delay and electron delay for off-equator interactions are of the same sense, thus interactions occurring upstream of the equator result in increased arrival times while downstream interactions result in a decrease.

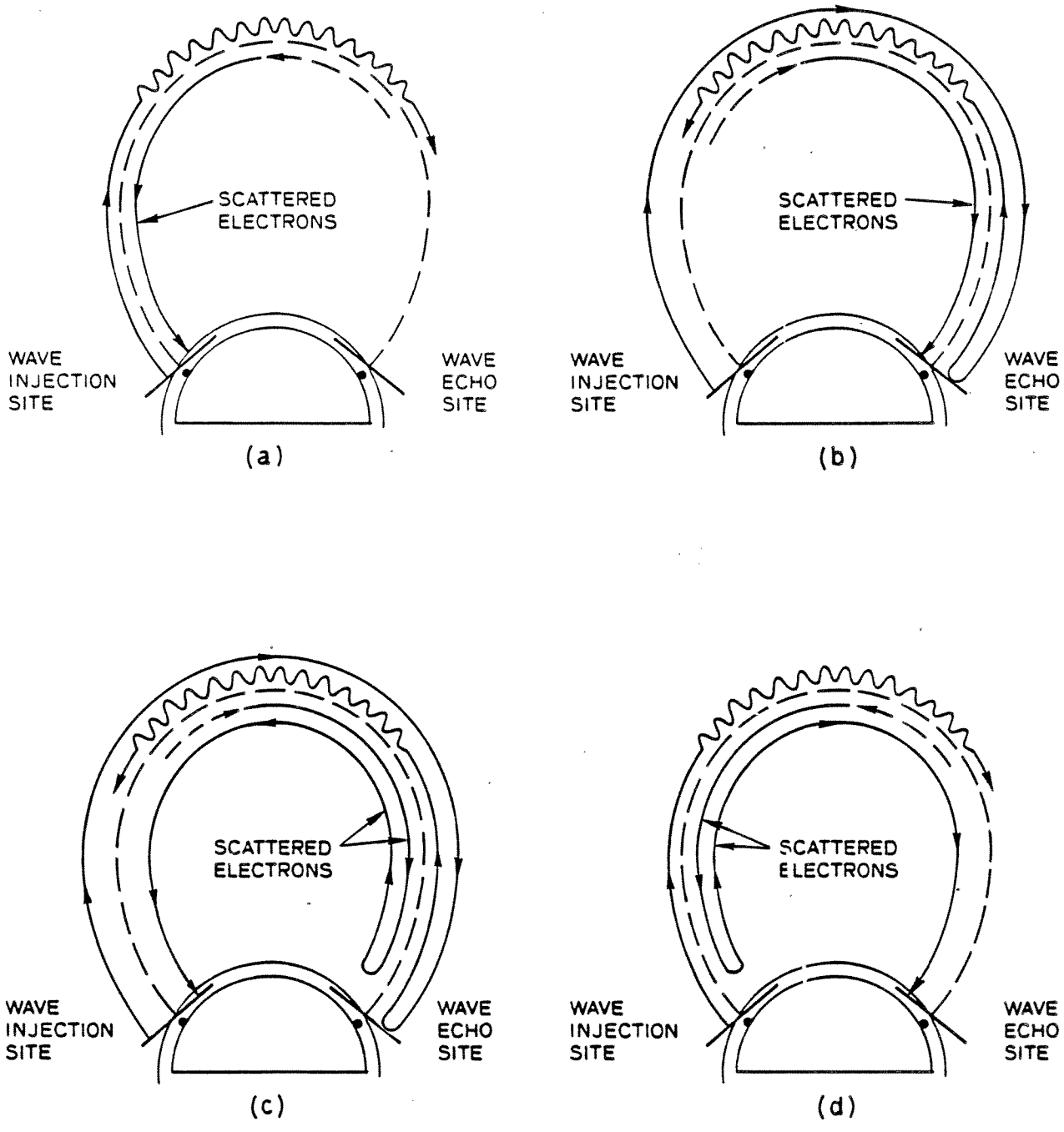

Figure 2.4 Schematic diagram of direct precipitation to (a) wave injection site and (b) wave echo site and mirrored precipitation to (c) wave injection site and (d) wave echo site

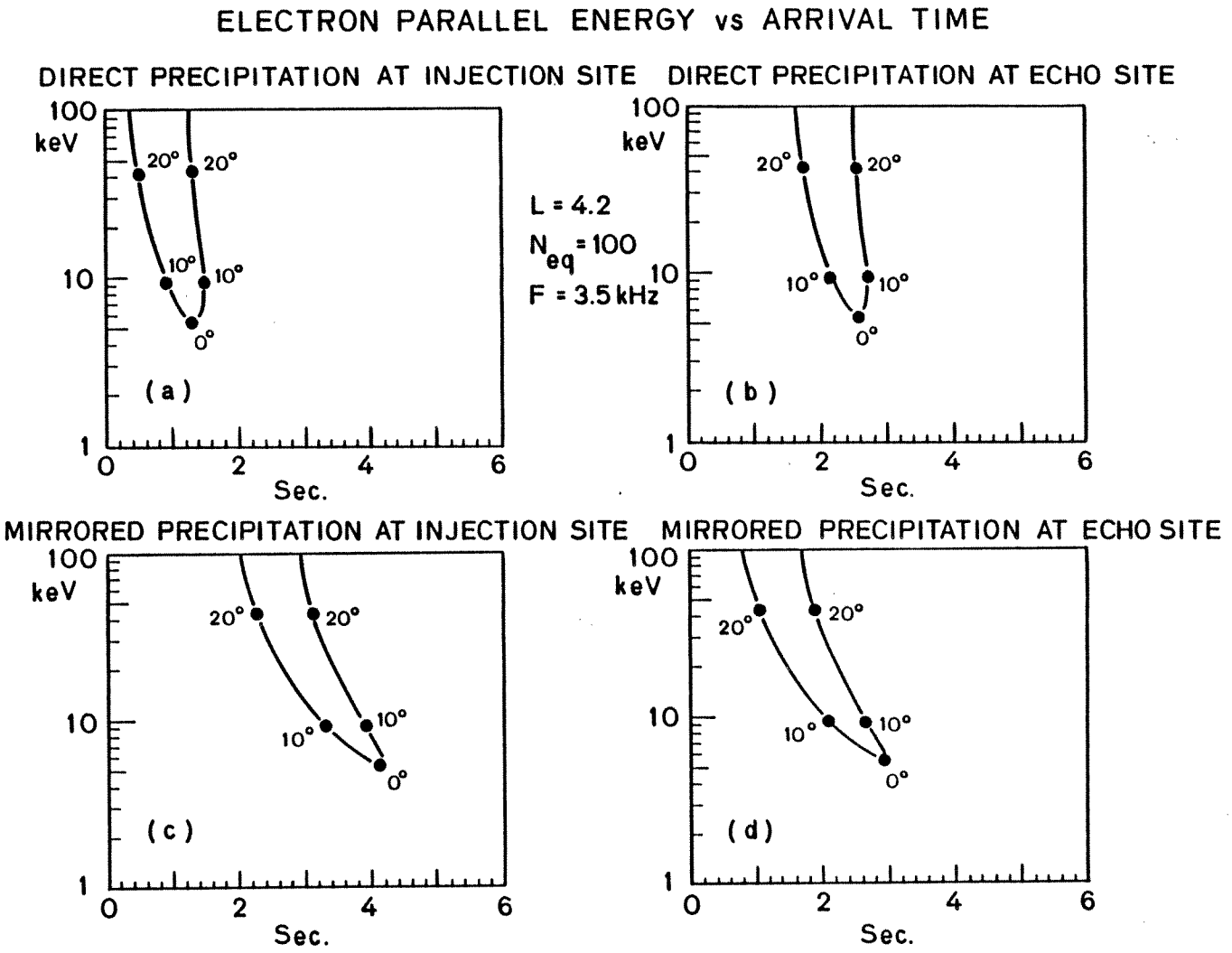

Figure 2.5 Parallel resonant energies as a function of arrival time for direct and mirrored precipitation at conjugate points.

The parallel resonant energies of precipitating electrons for the four cases are shown as a function of arrival time at the ionosphere in figure 2.5. The monochromatic wave frequency is chosen as 3.5 kHz and the equatorial electron density is 100 cm^{-3} on the L=4.2 field line. The first electrons to arrive are the high energy ones which are scattered on the near side of the equator. Next, the high energy electrons from the far side of the equator arrive, followed by the lower energy ones scattered nearest to the equator. Since electrons of different energies from separate segments of the interaction region can arrive at the same time, it is necessary to sum simultaneous fluxes from all contributing segments to determine the total flux at the ionosphere as a function of time.

D. Precipitation Energy Flux

In order to model the total energy flux precipitated from an extended region about the equator, it is useful to consider the region as consisting of successive segments along the field line, each making a local contribution to the total flux. The average number flux (number per unit area per second) of precipitating electrons scattered by a wave in any segment of the interaction region is found by multiplying the number of loss cone electrons per unit volume by the average parallel velocity per electron. The average energy flux for a segment is simply the number flux multiplied by the average energy per electron. In order to translate down to the ionosphere it is necessary to account for the compression of the field lines by multiplying the energy flux by the ratio of the cross-sectional area of the magnetic flux tube at the

interaction point to that at the ionosphere. Thus the average energy flux at the ionosphere from any segment of the interaction region can be expressed as

$$\mathcal{F}_i = \overline{\rho}_i \, \overline{v}_i \, \overline{E}_i \, \overline{A}_i$$

where $\overline{\rho}_i$ is the loss cone density due to scattering (number/cm^3)

$\overline{v}_i$ is the average parallel velocity (cm/sec)

$\overline{E}_i$ is the average electron energy (ergs)

$\overline{A}_i$ is the magnetic flux tube cross-sectional area which maps to unity at the ionosphere

For computational purposes these values are expressed as averages found between limiting values determined at the spatial extremes of each segment (e.g. $\overline{A}_i = (A_i + A_{i+1})/2$). If the length of each segment is made sufficiently small, then the averages become representative for the electrons scattered within the segments.

To find the magnetic flux tube cross-sectional area (A_i) at any point which maps to unity at the loss cone mirror height (i.e. $A_{100} = 1.0$), we recall from conservation of magnetic flux that

$$A_1 B_1 = A_2 B_2 = \text{constant}$$

where B is the magnetic flux density and therefore

$$A_i = B_{100} / B_i$$

We assume that the magnetic field is well represented by a centered dipole at the mid-latitudes being considered, thus the field strength at a location whose coordinates are (r,λ) can be expressed as

$$B(r,\lambda) = 3.12 \times 10^{-5} \left(\frac{r_o}{r}\right)^3 \left(1 + 3 \sin^2\lambda \right)^{\frac{1}{2}}$$

where $$r = r_o \left[\frac{\cos \lambda}{\cos \lambda_{100}}\right]^2$$

r is the distance from the dipole center to a given point on the field line

λ is the latitude of a given point of the field line

λ_o is the latitude of the point where the field line intercepts the earth

Thus

$$A_i = \left[\frac{\cos \lambda_i}{\cos \lambda_{100}}\right]^6 \left[\frac{1 + 3 \sin^2 \lambda_{100}}{1 + 3 \sin^2 \lambda_i}\right]^{\frac{1}{2}}$$

The loss cone density (ρ) depends on the availability of potentially resonant electrons and on how efficient a wave is in perturbing the pitch angle of the resonant electrons. The scattering efficiency terms embody the detailed physics of the momentum transfer during cyclotron resonance and are a function of the wave intensity and the amount of time in which the perturbing forces are significant as an electron travels through the wave train. The latter factor, referred to as the interaction time, depends on the relative velocity of the wave as seen in the electron frame of reference. In the equatorial region the wave phase velocity varies slowly with latitude while the parallel velocities of electrons which satisfy the resonance condition increase

rapidly for interactions occurring further from the equator. Therefore the scattering efficiency of a wave can be represented by the product of two terms, one a function (b) which varies inversely with the electron parallel kinetic energy, and the other (a) which depends on the wave intensity. The loss cone density can then be expressed as

$$\rho = a\, b\, E^{-p}$$

where the inverse power law distribution in energy which is typical for the trapped flux is also assumed to describe the loss cone flux.

A knowledge of the scattering efficiency is required if we wish to calculate the absolute magnitude of the precipitation energy flux. However if we need only to obtain the shape of the flux curve with time, then we can proceed by normalizing the contribution to the total preciptation energy flux from any segment of the interaction region by the energy flux from the segment that makes the greatest contribution, which as we have seen is the equatorial segment. Thus the normalized flux due to scattering in any segment is

$$\frac{\mathcal{F}_i}{\mathcal{F}_{eq}} = \frac{\overline{\rho}_i\ \overline{v}_i\ \overline{E}_i\ \overline{A}_i}{\overline{\rho}_{eq}\ \overline{v}_{eq}\ \overline{E}_{eq}\ \overline{A}_{eq}}$$

where the subscripts eq and i denote the equatorial and i-th segments, respectively. This eliminates the need to know the loss cone densities explicity since the normalized loss cone densities can be expressed in terms of normalized scattering efficiency terms (ξ and ζ).

$$\frac{\bar{\rho}_i}{\bar{\rho}_{eq}} = \frac{\bar{a}_i\ \bar{b}_i}{\bar{a}_{eq}\ \bar{b}_{eq}}$$

Next we define $\xi_i = \frac{\bar{a}_i}{\bar{a}_{eq}}$ and $\zeta_i = \frac{\bar{b}_i}{\bar{b}_{eq}}$

Now the normalized flux can be expressed as

$$\frac{\bar{\mathcal{F}}_i}{\bar{\mathcal{F}}_{eq}} = \xi_i \zeta_i \left(\frac{\bar{E}_i}{\bar{E}_{eq}}\right)^{1-p} \frac{\bar{v}_i\ \bar{A}_i}{\bar{v}_{eq}\ \bar{A}_{eq}}$$

The normalized scattering efficiency coefficients (ξ and ζ) are held constant with latitude in the following analysis to show how the energy flux as a function of arrival time varies with wave frequency, plasma density and path. The effect of allowing these terms to vary along the field line is treated in a later section.

E. Time Dependent Normalized Energy Flux

The precipitating electron flux from a segment of the interaction region begins to flow when the scattering wave enters the segment and continues until the wave leaves it. If we assume a constant reservoir of electrons available for scattering into the loss cone (reasonable for a single pass of a short wave train), then constant precipitation from a segment will continue for an interval equal to the propagation time across the segment plus the duration of the pulse. The precipitation is seen at the ionosphere for the same interval but delayed by the time required for the electrons to traverse the distance from the interaction

point to the ionosphere. To obtain the total normalized precipitation energy flux at the ionosphere as a function of time, we simply sum the individual fluxes from all segments which contribute in each increment of arrival time.

Assuming a constant reservoir, a long enduring wave train will allow all segments to contribute a constant portion to a resulting steady state precipitation. To study the effect of the concurrent arrival of electrons of various energies, we instead reduce the wave train to an impulse. The relative energy flux as a function of arrival time is shown in figure 2.6 for the same case considered in figure 2.5. A comparison of figure 2.6 with figure 2.5 indicates that the greatest total flux in this case is due to scattering close to the equator on the upstream side. The resulting peak can be many times greater than the energy flux due only to scattering in the equatorial (i.e. maximum contributing) segment, thus showing the importance of the arrival time convergence effect in determining the shape and intensity of the flux curve. For the curves shown, the peak is of larger relative magnitude for direct precipitation than it is for mirrored precipitation because the longer flight path in the latter case allows electrons of various energies to spread more in arrival times. The total energy deposition, given by the area under the curves, is the same in each case.

The time sequence for the precipitation events of figure 2.6 begins with the injection of a 3.5 kHz wave at t=0. Loss cone electrons arrive first at the injection site due to direct precipitation (figure 2.6a). A fraction of the electrons are backscattered from the ionosphere above the injection site and begin traveling back towards the

conjugate point. Meanwhile the wave is reflected from the conjugate ionosphere and makes a second pass through the equatorial interaction region. The electrons scattered during the second pass precipitate directly to the ionosphere above the wave echo site (figure 2.6b). A fraction of these are also backscattered and begin traveling towards the wave injection site. The electrons previously backscattered at the wave injection site next arrive at the wave echo site (figure 2.6d). Finally the electrons backscattered at the wave echo site arrive at the wave injection site (figure 2.6c).

The relative energy fluxes for the direct or mirrored precipitation in figure 2.6 are calculated as if 100 percent of the loss cone electrons are deposited at one end of the field line. If mirroring occurs then the loss cone electrons due to a single pass of the VLF wave through the equatorial region will be shared between the precipitation fluxes at both ends of the field line and the relative magnitudes of figure 2.6 should be scaled accordingly. A return of 100 percent of the scattered electrons to the conjugate hemisphere could only occur if an asymmetry in mirror heights caused the equatorial pitch angle for the loss cone at the mirror point to lie inside of the equatorial pitch angle for the loss cone at the precipitation point. If we neglect the mirror height asymmetry the returned energy flux due only to backscattering will be about 10 percent (Davidson and Walt, 1977) of the relative magnitudes shown in figure 2.6 (c) and (d). This reduction makes the mirrored precipitation events more difficult to detect than the direct events.

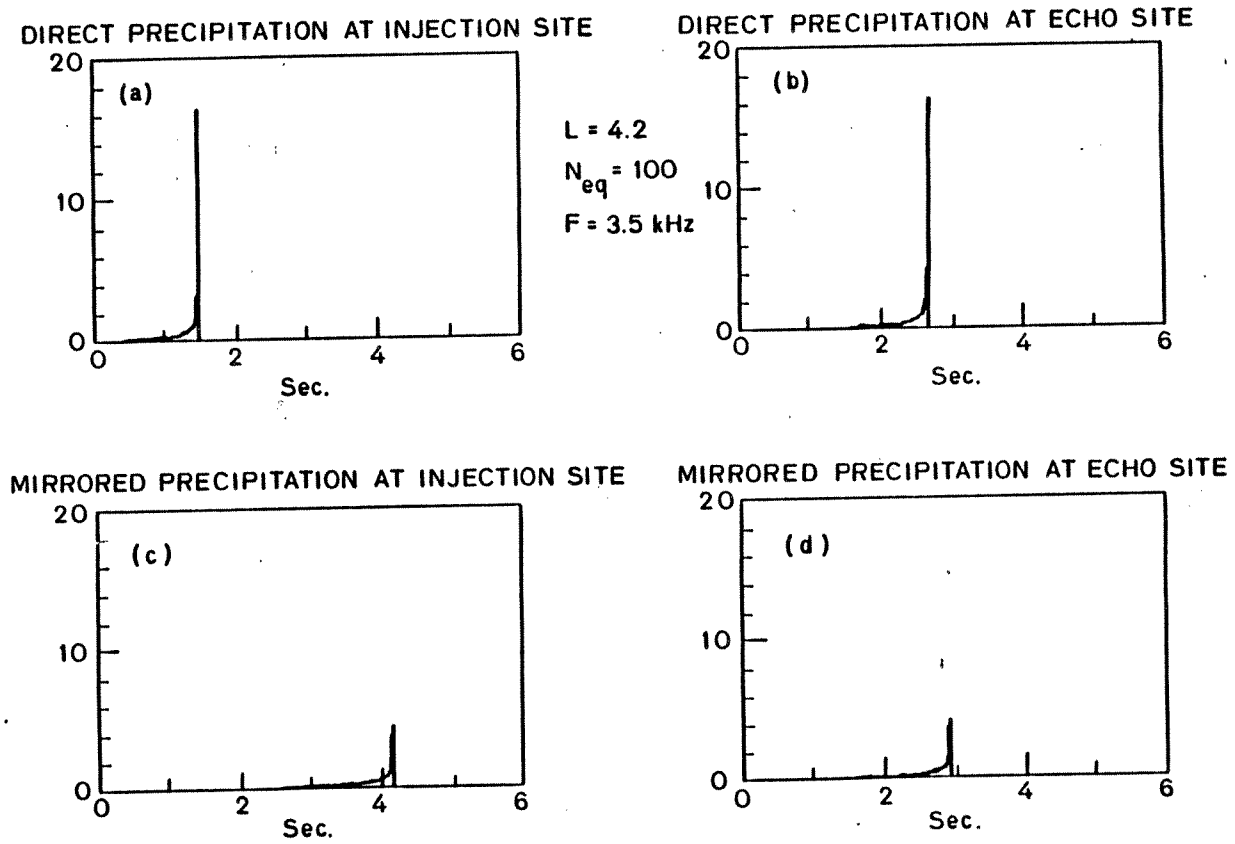

Figure 2.6 Normalized energy flux as a function of arrival time for direct and mirrored precipitation at conjugate points

F. Variation of Arrival Time Convergence with Wave Frequency

The general circumstance which leads to an arrival time convergence in electron precipitation is based on the integrals of the wave and electron velocities and on the length of the respective paths. These in turn are dependent on our choice of L, N_{eq} and f. To show the effect of varying these parameters we first let L=4.2 and N_{eq}=100 cm^{-3} as before and vary the wave frequency. In order to compare the arrival time curves for different cases, it is useful to calculate a weighted mean arrival time where the relative energy flux from each segment is used as a weighting factor.

$$t_{ave} = \frac{\sum_i \left(\frac{\mathcal{F}_i}{\mathcal{F}_{eq}}\right) t_i}{\sum_i \left(\frac{\mathcal{F}_i}{\mathcal{F}_{eq}}\right)}$$

The mean arrival time as a function of wave frequency is plotted in figure 2.7 for the cases of direct and mirrored precipitation at the wave injection site. The general effect of whistler mode dispersion is apparent, as is the effect of lower frequency waves resonating with faster electrons.

In figure 2.8 we have plotted the peak magnitude of the total normalized energy flux as a function of wave frequency for the L=4.2, N_{eq}=100 cm^{-3} case. The normalizing flux is frequency dependent because different frequencies resonate with different energy electrons at the equator. Consequently the values plotted are first scaled to arbitrary common units to allow direct comparison. The peak energy flux

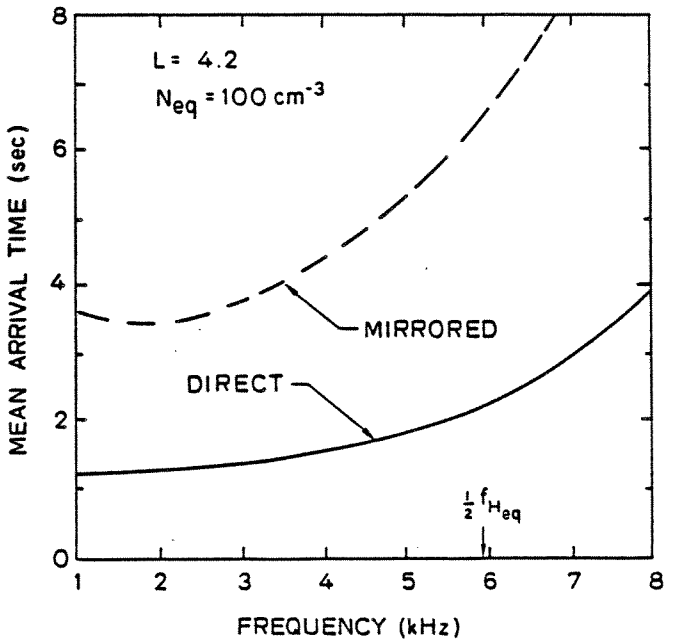

Figure 2.7 Mean arrival time of precipitating electrons as a function of wave frequency for L = 4.2, N_{eq} = 100 cm^{-3}.

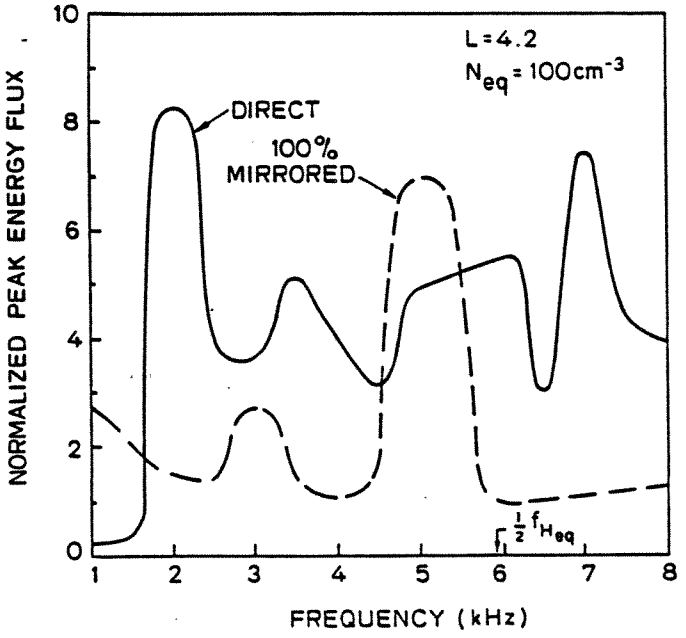

Figure 2.8 Peak magnitudes of normalized energy flux as a function of wave frequency for L = 4.2, N_{eq} = 100 cm^{-3}.

enhancement for direct precipitation is seen to generally exceed that for mirrored (100 percent backscattered) precipitation. However, a proper selection of the wave frequency can in some cases (e.g. f=5 kHz) cause the mirrored precipitation to exceed the peak magnitude of the direct precipitation assuming that a mirror height asymmetry allows 100 percent of the precipitating electrons to return from the conjugate point.

Another parameter which can be used to characterize the convergence effect is the standard deviation of arrival times.

$$s = \left[\frac{\sum_i \mathcal{F}_i \, (t_i - t_{ave})^2}{\sum_i \mathcal{F}_i} \right]^{\frac{1}{2}}$$

The standard deviation gives a measure of the spread in arrival time of electrons from all of the segments of the interaction region. A plot of the standard deviations as a function of interacting wave frequencies for the L=4.2, N_{eq}=100 cm^{-3} case is shown in figure 2.9. As intuition might suggest, the events which have the greatest peak magnitude are also the ones with the least spread in arrival times.

G. Variation of the Arrival Time Convergence with L and N_{eq}

A comparison of the arrival time convergence effect on different field lines or under different conditions of cold plasma density, is simplified if we choose the same energy distribution of loss cone electrons in each case. This can be done by requiring that the wave frequency for the comparative models be chosen such that the parallel

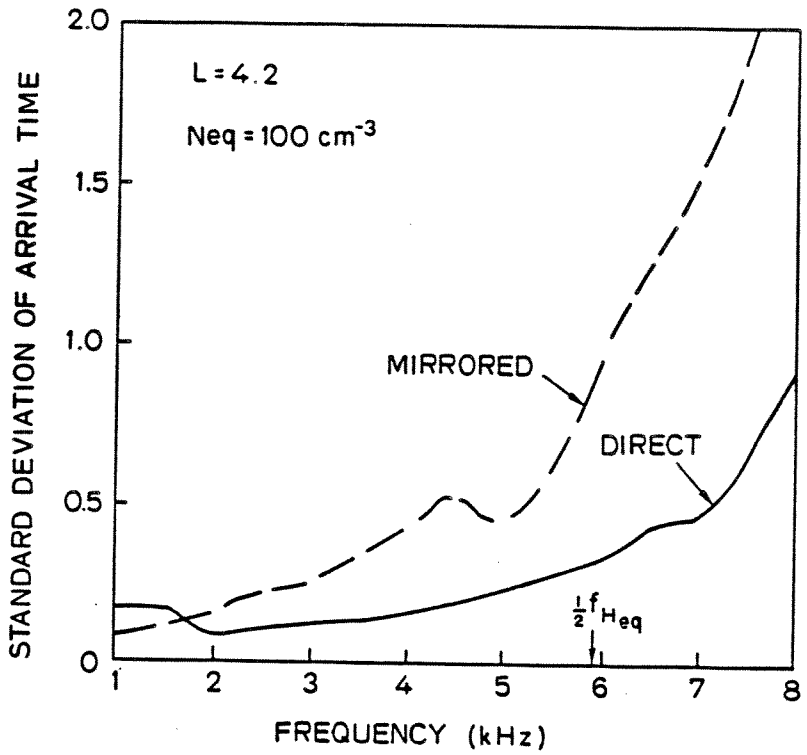

Figure 2.9 Standard deviation of arrival times as a function of wave frequency for L = 4.2, N_{eq} = 100 cm^{-3}

energy of electrons resonant at the equator (i.e. the lower energy limit) be the same in each case. As the wave propagates to higher latitudes along any field line it interacts with higher energy electrons until an arbitrary upper energy limit (e.g. 100 keV) is reached, beyond which the contributions to the total energy flux are assumed to be negligible. If we let the equatorial parallel resonant energy be 1.0 keV, then the corresponding resonant frequency can be plotted in L, N_{eq}, f space as shown in figure 2.10. We shall examine the variation of the arrival time convergence effect by first holding N_{eq} constant at 100 cm^{-3} while varying L, and then holding L constant at 4.2 while varying N_{eq}.

The mean arrival times are plotted for a range of mid-latitude L values in figure 2.11 for direct precipitation at the wave injection site. A general trend for longer delays at higher L shells results from

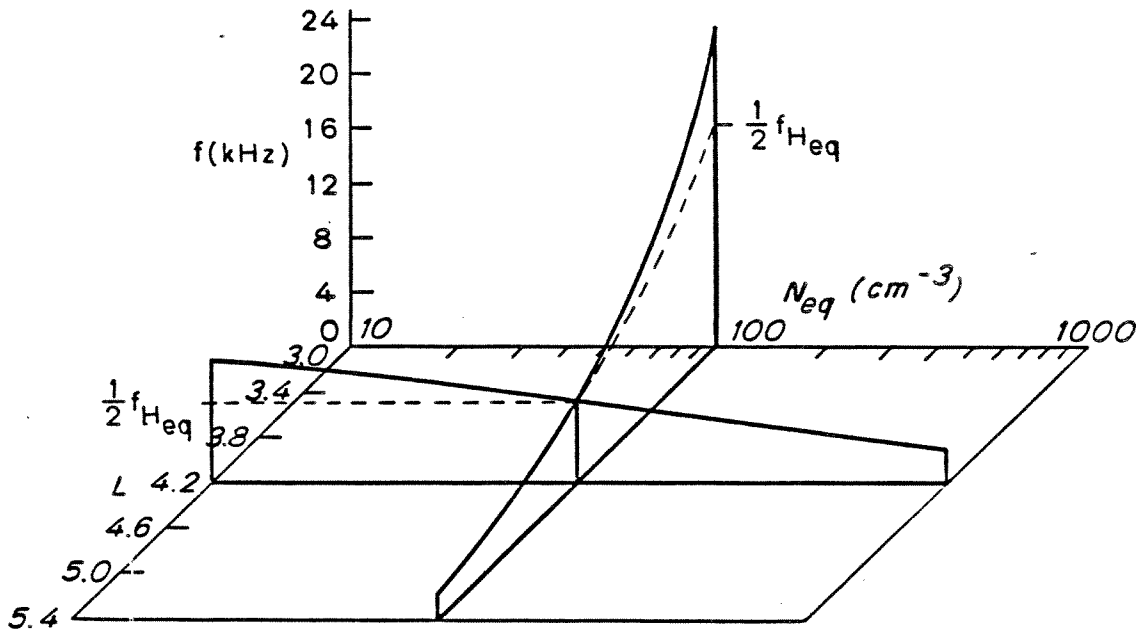

Figure 2.10 Frequency of waves resonant at the equator with 1.0 keV electrons as a function of L and N_{eq}

the longer distances which both waves and scattered electrons must traverse. Holding L constant at 4.2, figure 2.12 shows that greater cold plasma densities, also cause longer mean arrival times, primarily because of a decrease in the group velocity of the wave.

In order to quantitatively investigate the sharpness of the precipitation energy flux pulses under various conditions, we calculate the coefficient of kurtosis (or "peakedness") using the standard form (Spiegel, 1961)

$$\kappa = \frac{\sum_i \mathcal{F}_i \, (t_i - t_{ave})^4}{\sum_i \mathcal{F}_i} - 3$$

A coefficient of zero corresponds to arrival times which follow a normal curve, while coefficients greater than zero indicate an increasing

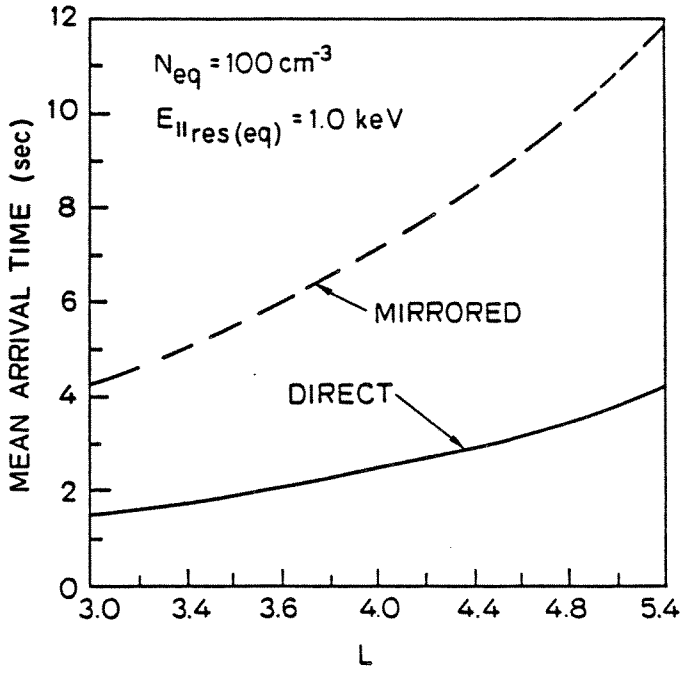

Figure 2.11 Mean arrival time as a function of L for precipitation due to scattering along path by waves which resonate with 1.0 keV electrons at the equator

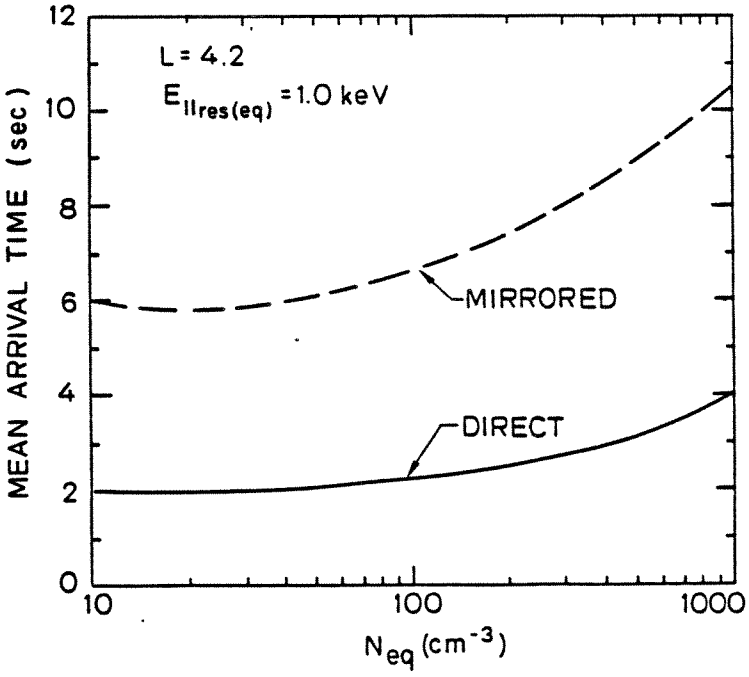

Figure 2.12 Mean arrival time as a function of N_{eq} for precipitation due to scattering along path by waves which resonate with 1.0 keV electrons at the equator

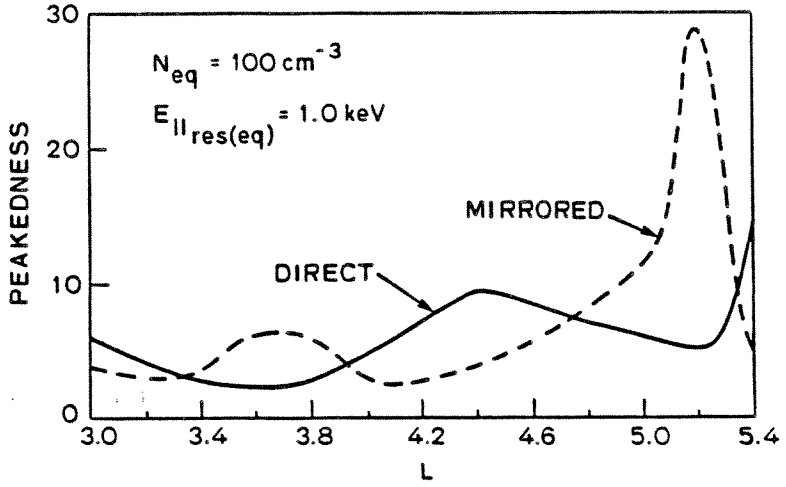

Figure 2.13 Peakedness coefficient as a function of L for precipitation due to scattering along path by waves which resonate with 1.0 keV electrons at the equator

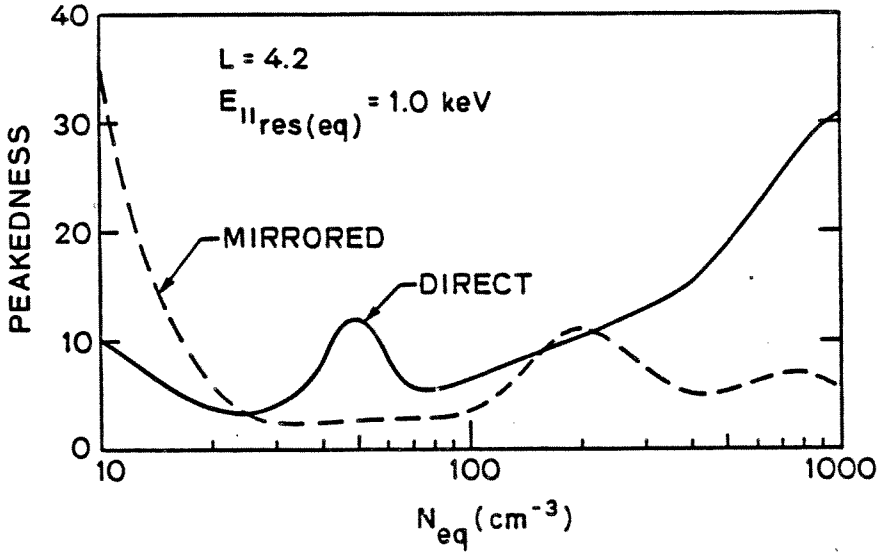

Figure 2.14 Peakedness coefficient as a function of Neq for precipitation due to scattering along path by waves which resonate with 1.0 keV electrons at the equator

degree of peakedness. In figure 2.13 the peakedness coefficient is plotted as a function of L for the cases of figure 2.11. In figure 2.14 the peakedness coefficient is plotted as a function of N_{eq} for the cases of figure 2.12. The curves show that the precipitation energy flux can be a more or less sharply defined pulse depending on the conditions. Knowing the shape of an expected precipitation burst could allow a detector to recognize characteristic pulses buried in a noisy background.

H. Pulses of Longer Duration

The precipitation energy flux due to an impulse has been used in the preceding section to study the variation of the pulse shape with changes in L or N_{eq}. However many VLF waves are of extended duration and therefore the precipitation from any segment of the interaction region will continue for the additional time that the wave is present or until the supply of electrons near the loss cone is reduced. Assuming a constant reservoir of electrons near the loss cone, then as the duration of a constant amplitude wave is increased, both the magnitude and duration of the precipitation pulse will increase. For very long wave trains the entire interaction region can contribute simultaneously to the precipitation flux. The case of L=4.2, N_{eq}=100 cm^{-3} is shown in figure 2.15 for waves of various durations. For direct precipitation the energy flux is seen to saturate for waves of duration greater than about 1.0 seconds. For mirrored precipitation, where there is greater spreading of arrival times between low and high energy electrons, saturation occurs for waves of duration greater than about 2.0 seconds.

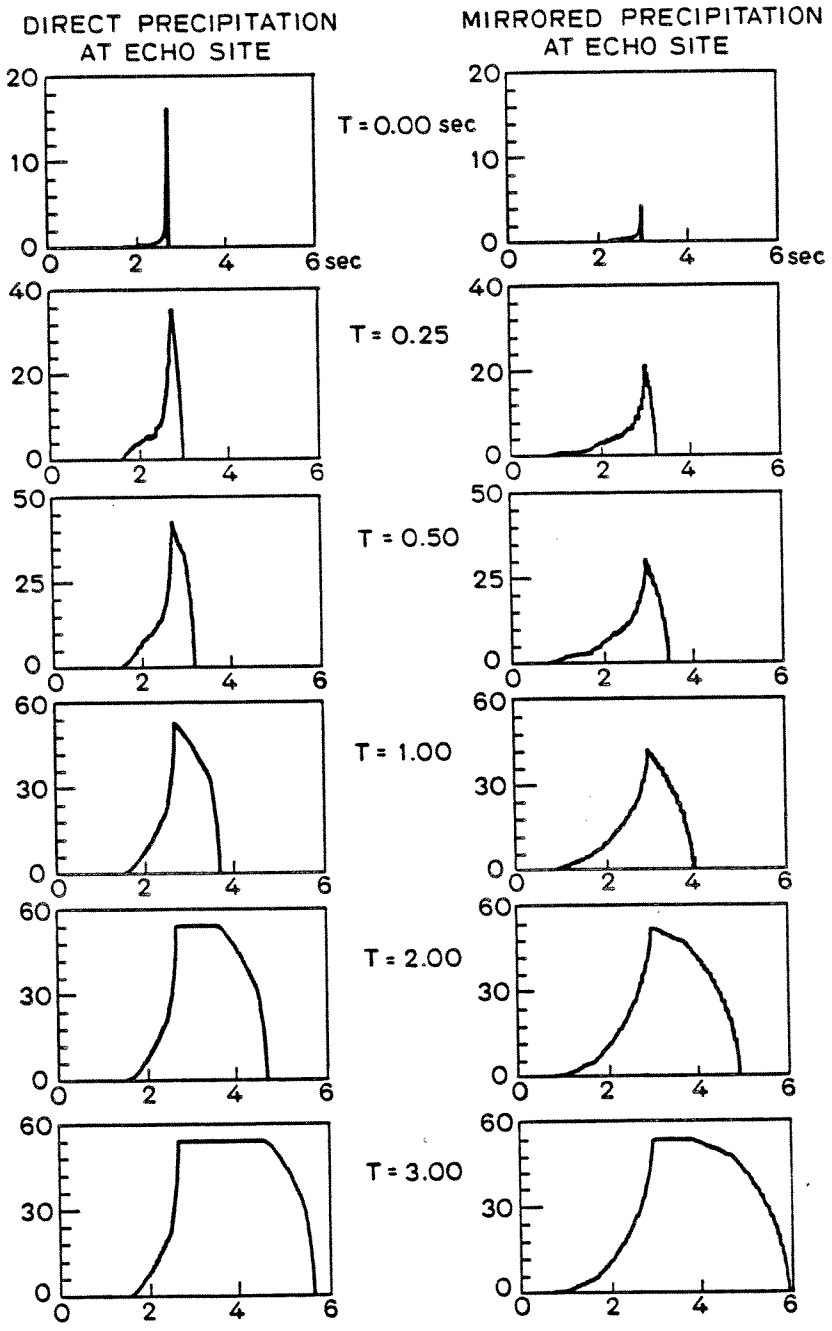

Figure 2.15 Variation in relative energy flux caused by increasing the duration of the VLF wave train

I. Scattering Efficiency

Two normalized scattering efficiency coefficients have been described previously. One coefficient (ξ) reflects the dependence of scattering on wave amplitude while the other (ζ) includes the effect of a decrease in interaction time for electrons of greater parallel velocities. The importance of including these terms can be established by comparing models in which each is allowed to vary while the other is held constant. First we shall consider the effect of varying the duration of the interaction time along the path.

Duration dependent efficiency. The amount of time that an energetic electron is subjected to the forces of a perturbing wave depends on the relative wave velocity as seen in the electron frame of reference and on the length of the wave train. In the equatorial region the wave group velocity is nearly constant while the electron parallel velocities which satisfy the resonance condition vary considerably with latitude. Therefore the normalized scattering efficiency term ζ for a wave of a given duration can be expressed as a function which decreases with an increase in the electron parallel kinetic energy. The normalizing factor here is the efficiency value associated with scattering at the equator such that $\zeta_{eq}=1.0$.

In the model results presented previously, ζ has been assumed to remain constant over the path. The normalized energy flux as a function of arrival time is shown in figure 2.16a for L=4.2, N=100 cm^{-3}, f=3.5 kHz, and a wave duration of 0.25 seconds where ζ is held constant over the path. Figure 2.16b shows a similar result except that ζ is allowed

to decrease linearly with increasing parallel kinetic energy. In this case ζ varies from 1.0 at the minimum resonant energy (i.e. E=5.45 keV at the equator) to zero at the limit of the interaction region (e.g. when E=100 keV). In the cases of figure 2.16 (c) and (d), the scattering efficiency is allowed to decrease exponentially from ζ=1.0 at the equator. The efficiency is reduced to 1/e in the case of figure 2.16c when the parallel energy is half way (about 53 keV) between the resonant energies at the equator and the limit of the interaction region. The scattering efficiency in the case of figure 2.16d falls off more rapidly, reaching 1/e when the energy is only one quarter of the way (about 29 keV) between the limits.

A comparison of the models of figure 2.16 shows that while decreasing the scattering efficiency with increasing latitude slightly reduces the magnitude of the precipitation energy flux, it does not appreciably alter the general shape of the burst. This is because the energy distribution of the trapped electrons diminishes rapidly with increasing energy and therefore fewer high energy electrons are available to be scattered regardless of how efficient the scattering forces might be. Thus we find that holding the interaction time term of the scattering efficiency constant over the entire equatorial region gives a reasonable first order pulse shape.

Amplitude dependent efficiency. The wave amplitude term of the scattering efficiency (ξ) can be examined by holding constant the interaction time term (ζ) and allowing the wave to grow as it propagates along the path. The case shown in figure 2.17a is typical of models

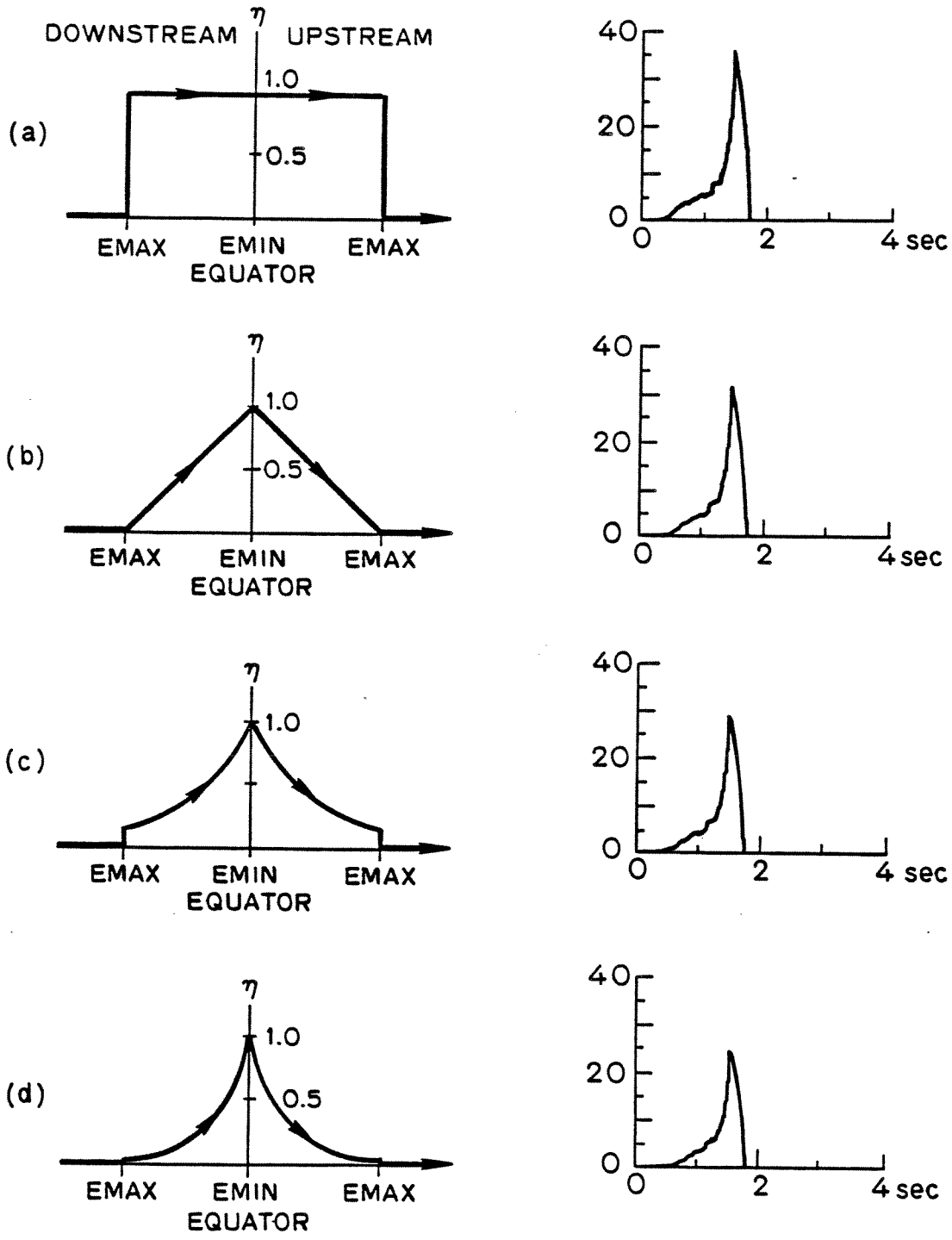

Figure 2.16 Dependence of the relative energy flux on the scattering efficiency term associated with the interaction time

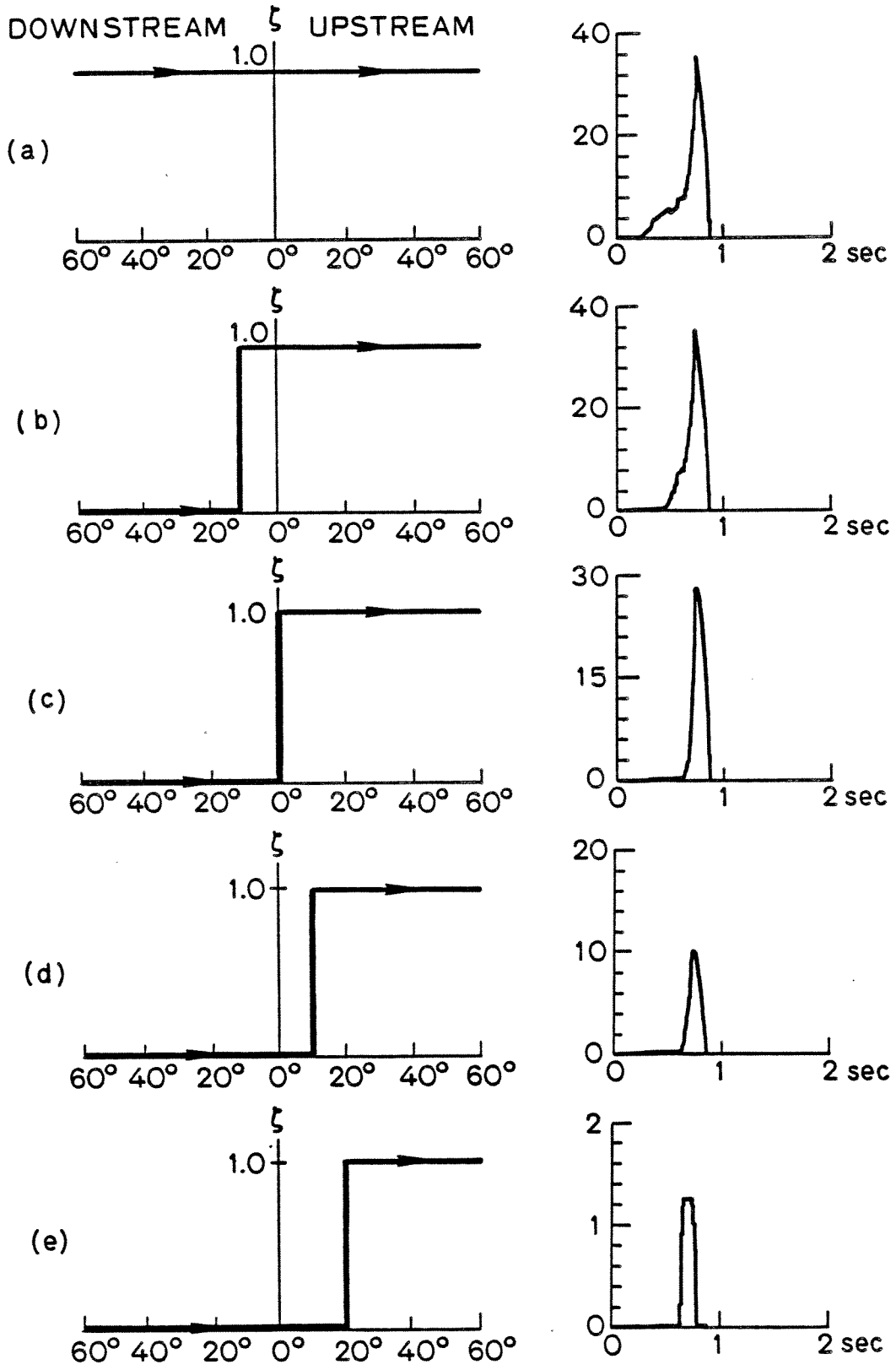

Figure 2.17 Dependence of the relative energy flux on the scattering efficiency term associated with the wave amplitude

shown previously where neither growth nor attenuation is exhibited by the wave and therefore the normalized wave amplitude term of the scattering efficiency remains constant at ξ=1.0. The model parameters for that example are L=4.2, N_{eq}=100 cm^{-3}, f=3.5 kHz and the wave duration is 0.25 seconds.

When growth is included, the wave becomes more efficient in scattering electrons into the loss cone as the amplitude increases. The growth region is believed to lie near the equatorial plane (Helliwell, 1967). In order to investigate the effect of wave growth on the precipitation energy flux pulse shape we will appoximate the amplitude dependent scattering efficiency term by a step function such that the wave "turns on" to its maximum amplitude at a particular latitude along the field line. As the wave propagates to the turn-on point, ξ has a value of zero. Beyond the turn-on point, ξ has a value of one. Step function wave growth in the equatorial region has shown good agreement with observation of optical emissions correlated with VLF noise bursts seen at L=4.2 (Helliwell et al., 1980).

In panels (b), (c), (d), and (e) of figure 2.17, the step function wave growth is seen to turn on at various points along the field line as the wave propagates from left to right. In panel (b), the turn-on point is at a latitude of 10 degrees on the downstream side of the equator. The energy flux pulse shape for this case is quite similar to that of case (a) where the wave has a constant amplitude at all points along the path. A noticable difference, however, can be seen in the leading edge where the absence of a scattering wave on the left side of the turn-on point results in an absence of higher energy downstream electrons. This

effect is more pronounced in panel (c) where the flux has no contributions from the entire downstream side of the equator. If wave growth were delayed until the wave propagated to the upstream side of the equator, then the shape of the precipitation flux would be determined by only the higher energy electrons which satisfy the resonance condition at higher latitudes. The results seen in panels (d) and (e) show that the relative magnitude of the energy flux is much less in those cases since the number of electrons available to be scattered is less because of the inverse nature of the energy distribution (here assumed to go as E^{-2}).

Unlike the scattering efficiency term (ζ), which depends on the amount of time a wave and counter streaming electron are in close proximity to each other, a variation with location along the field line of the amplitude dependent efficiency term (ξ) is seen to have a pronounced effect on the energy flux pulse shape. It should be possible to roughly bracket the region along a field line where wave growth is occurring by examining data for wave-induced electron precipitation events. The procedure might begin by determining the path and cold plasma density using the whistler scaling method (Park, 1972). The relative energy flux profiles for a range of wave turn-on locations could then be modeled for a monochromatic wave of the observed frequency and duration using the technique described in this chapter. A shape comparison between the observed and modeled precipitation bursts would then provide a means of estimating the wave turn-on location. Although growth does not actually occur as a step function, it is reasonable to model it as such in order to obtain a first order approximation of the location of the growth region.

Chapter III

COMPARISON BETWEEN ARRIVAL TIME MODEL AND CORRELATIVE OBSERVATIONS

In this chapter we examine the relative timing between observed VLF events and correlated precipitation effects. The time differences are compared to the results predicted by the model described in chapter 2. Observations which agree with the model will support the hypothesis that electron precipitation results from cyclotron resonant interactions with whistler mode waves propagation in the magnetosphere.

A. X-ray Events of January 2, 1971 at Siple Station

The first correlation between discrete VLF waves and an effect of electron precipitation (Rosenberg et al., 1971) was obtained on January 2, 1971 by measuring bremsstrahlung X-ray bursts using a balloon-borne detector launched from Siple station. From an examination of the ground based VLF recordings, it was determined that the waves led the arrival of the precipitating electrons by about 0.3 to 0.4 seconds. Direct precipitation at Siple station would result from a north-going wave scattering south-going electrons into the loss cone. Mirrored precipitation would result from a south-going wave scattering north-going electrons which then mirror above Roberval before entering the Siple loss cone. Mirrored precipitation was found to provide a better explanation of the January 2, 1971 data than direct precipitation because, while the VLF emissions at Siple station were closely correlated with the X-ray bursts, similar VLF emissions at Roberval were not.

Rosenberg et al. (1971) used a simple model similar to that discussed in chapter 2 to calculate the arrival time of electrons scattered only at the equator. The propagation path was assumed to be outside the plasmapause where the equatorial electron density was estimated to be 10 cm^{-3}(Angerami and Carpenter, 1966). The relative arrival times were calculated on the basis of mirrored precipitaion and provided electron lag times which are generally consistent with the observations. We shall reexamine the timing by calculating the relative arrival times when interactions off the equator are included. We also will ignore the absence of a correlation with the VLF emissions at Roberval and consider the arrival times associated with direct precipitation to Siple.

The equatorial electron density on the L=4.2 field line at the time of the correlation was estimated (Carpenter et al., 1975) through whistler scaling to be 25 ±12 cm^{-3}, slightly greater than the 10 cm^{-3} used in the calculations of Rosenberg et al. The VLF activity was characterized by quasi-periodic whistler triggered bursts of rising emissions with durations of 0.5 to 3.0 seconds in a frequency band of about 2 to 4 kHz. The model was run for a representative 0.5 second long wave at 3 kHz. The results for precipitation to the wave echo site (analogous to Siple station in this case) are summarized in table 3.1 where the mean electron arrival times are expressed as lags measured from the mean arrival time of the wave train. The model was run both for diffusive equilibrium (DE) and collisionless (CL) plasmas.

The lags obtained from the models show in table 3.1 that direct precipitation should arrive later than the 0.3 to 0.4 seconds observed.

Table 3.1
Mean Arrival Time Lag of Electrons relative to Waves
Observed at Siple Station 02 Jan 71

N_{eq}	Mirrored		Direct	
	DE	CL	DE	CL
13	0.38	0.28	0.46	0.56 sec
25	0.49	0.36	0.60	0.75
37	0.59	0.41	0.71	0.88

Thus the direct mode of precipitation can be discounted on the basis of the arrival time calculations in addition to the observation that no north-going wave was seen. The mirrored precipitation time lags found by including off-equator interactions show a better agreement with the observations for the case of the collisionless plasma model than for diffusive equilibrium.

These calculations support the conclusion by Rosenberg et al. (1971) that the observed X-ray bursts were due to mirrored precipitation. Some of the electrons initially directed towards the northern hemisphere mirror point may have been scattered into the Roberval loss cone. Precipitation would then have occurred by the direct mode at Roberval shortly before the mirrored electrons were detected at Siple. At the time of the January 2, 1971 events, no sensors suitable for detecting precipitation were being operated at Roberval.

B. Optical Emissions of July 24, 1971
at Siple Station

One-to-one correlations between discrete VLF waves and bursts of ionospheric optical emissions were first observed in 1977 at Siple

station (Doolittle et al., 1978) and have been discussed in detail by Helliwell et al. (1980). In most cases the VLF waves were similar to those correlated with the X-ray bursts discussed above. Propagation was generally outside the plasmapause where equatorial densities were quite low. The events were characterized by bursts of rising VLF emissions, usually in a frequency range of 2-4 kHz. In several cases triggering by whistlers was evident.

The arrival time model described in chapter 2 has evolved from an earlier version which computed the time of arrival for individual energetic electrons, but did not attempt to find the temporal shape of the precipitation pulse. The earlier model was used by Helliwell et al. (1980) to predict the time when a precipitation flux would be expected to arrive at Siple station under the conditions which existed during the correlations of July 24, 1977. The equatorial density on the L=4.2 field line was determined by whistler scaling to be about 100 cm^{-3} at that time. By modeling both the direct and mirrored modes of precipitation, it was found that the photometer results could best be explained by direct precipitation. This interpretation, therefore, is just opposite to the mirrored precipitation which explained the January 2, 1971 X-ray correlation.

The initial modeling by Helliwell et al. (1980) of the July 24, 1977 event for 2-4 kHz waves provided a means of determining the range of times in which electrons of various energies could arrive at the Siple ionosphere. Direct precipitation under the conditions modeled showed an arrival time convergence in which electrons of energies up to 30 keV resonant with 2-4 kHz waves would arrive within about 200

milliseconds of each other during an interval of 2.6 to 3.0 seconds after the triggering wave was launched by a lightning stoke. Adding the 1.2 second duration of the emission wave train to this, the upper limit is extended to 4.2 seconds. For the case of mirrored precipitation, however, it was shown that electrons of various energies less than 30 keV would have their arrivals spread out in time from about 2.0 to 4.8 seconds. The observed photometer response occurred during the interval 2.6 to 4.3 seconds, and therefore the direct mode of precipitation showed better agreement.

The July 24, 1977 event can be reexamined by using the model described in chapter 2 which determines the normalized flux as a function of arrival time. A more specific determination of the expected time of a photometric response will result since the model uses the parallel resonant energies to weight the contributions to the total precipitation flux from each segment of the interaction region. The flux will fall off rapidly with energy for a distribution proportional to E^{-2}, and therefore the greatest contributions to the total flux are made by the lower energy electrons resonant closest to the equator. Thus the interpetation of the expected arrival times described by Helliwell et al. (1980), which gave equal weight to all electrons in a range of energies up to 30 keV, may have been subjectively biased by the relatively fewer high energy electrons.

The results of the arrival time model for the conditions appropriate to the July 24, 1977 event are shown in figure 2.15 for waves of various durations at 3.5 kHz. For a 1.2 second long wave train, precipitation of electrons of energies up to 100 keV should occur

during the intervals 1.6 to 3.8 and 0.7 to 4.1 seconds, respectively, for the cases of direct and mirrored precipitation. These intervals include the peaks and the low energy flux shoulders which would be less easily detected against a noisy background. A better comparison between the direct and mirrored cases can be made by considering the range of arrival times for the peaks alone as measured at half of the maximum amplitude of the pulses. Precipitation above the half maximum level is then found to occur from 2.5 to 3.7 and 2.6 to 3.9 seconds, respectively for the direct and mirrored cases. The close coincidence of the two pulses suggests that it would have been difficult to distinguish them in the data. One distinguishing feature, however, is the faster rise time associated with the direct mode.

The peaks of the model precipitation pulses occur at about 2.6 and 3.0 seconds for the direct and mirrored modes. An uncertainty in N_{eq} of ± 25 cm^{-3} will result in an uncertainty in the times of the precipitation peaks of about ± 0.1 second. Measurements of the observed photometer pulses indicated that the precipitation began at about 2.6 seconds after the spheric and peaked at about 3.4 seconds. The data suggests that both the direct and mirrored modes could have contributed to the total flux. The leading edge of the optical bursts is best modeled by direct precipitation while the peak is more closely modeled by mirrored precipitation.

The conjugate VLF records during the July 24, 1977 events showed that the two-hop wave received at Roberval was only about 2 dB weaker than the 0.5 pT waves seen at Siple. This was stressed by Helliwell et al. (1980) to point out that scattering by the north-going echo

should be comparable in magnitude to scattering by the south-going wave. They concluded that direct precipitation to Siple station is the more plausible model because no backscattering or asymmetric mirroring is required. Yet the January 2, 1971 X-ray event has given credibility to the mirrored mode for precipitation to Siple station.

C. Optical Emissions of August 30, 1977 at Roberval

The coincidence in arrival times at the wave echo site for electrons precipitated by the direct and mirrored modes can make it difficult to distinguish one mode as being a preferred source of precipitation. Even for cases of low equatorial electron density, such as the January 2,1971 event when short whistler travel times compared to the electron travel times cause the direct and mirrored precipitation pulse separations to be maximized, the two modes will peak within a few hundred milliseconds of each other. At the wave injection site, however, the arrival times for the direct and mirrored modes will be widely separated as can be seen in figure 2.6 (a) and (c). A detector at the wave injection site should be able to unambiguously determine which mode is responsible for an observed precipitation pulse. Most of the noise bursts correlated with the precipitation events seen at Siple station were triggered by waves injected into the magnetosphere by lightning strokes in the vicinity of Roberval, Quebec. In an attempt to correlate over head optical emissions with bursts of VLF noise at the wave injection site, a photometer was operated intermittently at Roberval from 1978 to 1981.

The Roberval photometer monitored ionospheric optical emissions of

N_2^+ at a wavelength of 4278 Angstroms using a narrow bandwidth interference filter. It had a 10 degree field of view centered on the zenith. The system turned on automatically after sunset and recorded the sky brightness on a chart recorder running at a slow speed. During synoptic intervals of 1 minute in every 15 the chart speed was increased by a factor of 10 to give better time resolution. VLF audio recordings were also made during the synoptic intervals, both at Roberval and at Siple station. The analog output of a photometer will reflect large amplitude slow variations in the night sky brightness due to such factors as airglow, moon elevation, integrated starlight in the field of view and encroachment of twilight. By using a high-pass filter with a 2 minute time constant, the slowly changing background was removed and the signal was further amplified by 13 dB so that very small bursts of ionospheric optical emissions would be detectable.

One-to-one correlations between optical emissions and whistler-triggered noise events were recorded at Roberval on 30 August, 1979, between 0735 and 0851 universal time (UT) (Doolittle, 1980). The photometer chart record during the 0750 synoptic interval is shown in figure 3.1a where bursts of optical emissions of about 1.5 seconds duration are labeled using letter designations. The integrated 2-3 kHz VLF amplitudes obtained from audio recordings made at Siple Station and Roberval are shown in figure 3.1 (b) and (c). Conjugate VLF spectrograms for the interval appear in figure 3.2 where the subscripts on the event labels indicate the lightning source (e.g., A_0), the one-hop whistler (A_1), and the two-hop whistler (A_2). In some cases up to seven hops were apparent. Rising emissions are associated with the

whistlers at each end of the field line. A comparison of the slope of the risers shows that retriggering occurs on each pass of the whistler through the magnetosphere.

The sequence of a typical event (e.g., F) begins with a lightning source in the northern hemisphere (F_0) which launches a VLF wave into the magnetosphere. The whistler mode wave is ducted along the Siple-Roberval field line and resonates with counter streaming electrons. Wave growth results from the interactions and therefore the wave becomes more efficient in scattering electrons as it travels past the equator. North-going electrons which are scattered into the loss cone continue spiraling along the field line toward Roberval while the wave travels south and is seen at Siple station (F_1) as a one-hop whistler. The precipitating electrons then cause the ionospheric optical burst (F) seen at Roberval and finally the two-hop whistler (F_2) arrives after the expected delay.

The times of occurrence for eight photometric peaks during the 0750 UT synoptic interval were scaled from the chart. These were then compared to the corresponding times of peak integrated VLF amplitude in a frequency band of 100 Hz. centered on 2 kHz. It was found that the photometric peaks led the peaks of the two-hop waves by an average of 0.7 seconds, with an rms deviation of 0.11 seconds. The average VLF noise burst had a duration of about 0.6 seconds.

In addition to the whistler-triggered noise bursts correlated with the optical emissions, the broadband VLF data during the 0735 to 0851 UT interval showed repeatable single trace whistlers propagating on two paths. One path was well inside the plasmapause and the other well

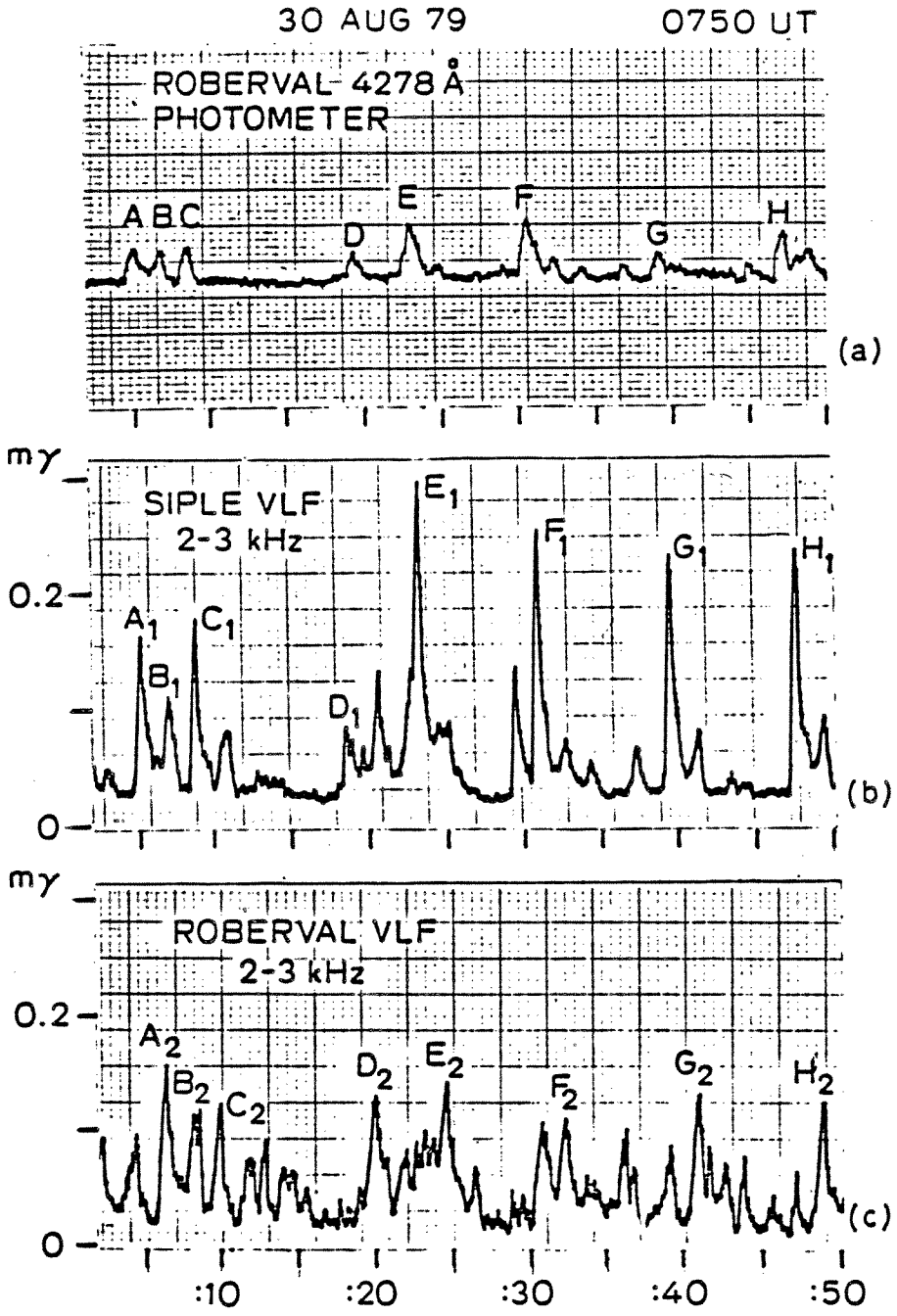

Figure 3.1 One-to-one correlation between a) Roberval photometer and VLF events seen at b) Siple station and c) Roberval

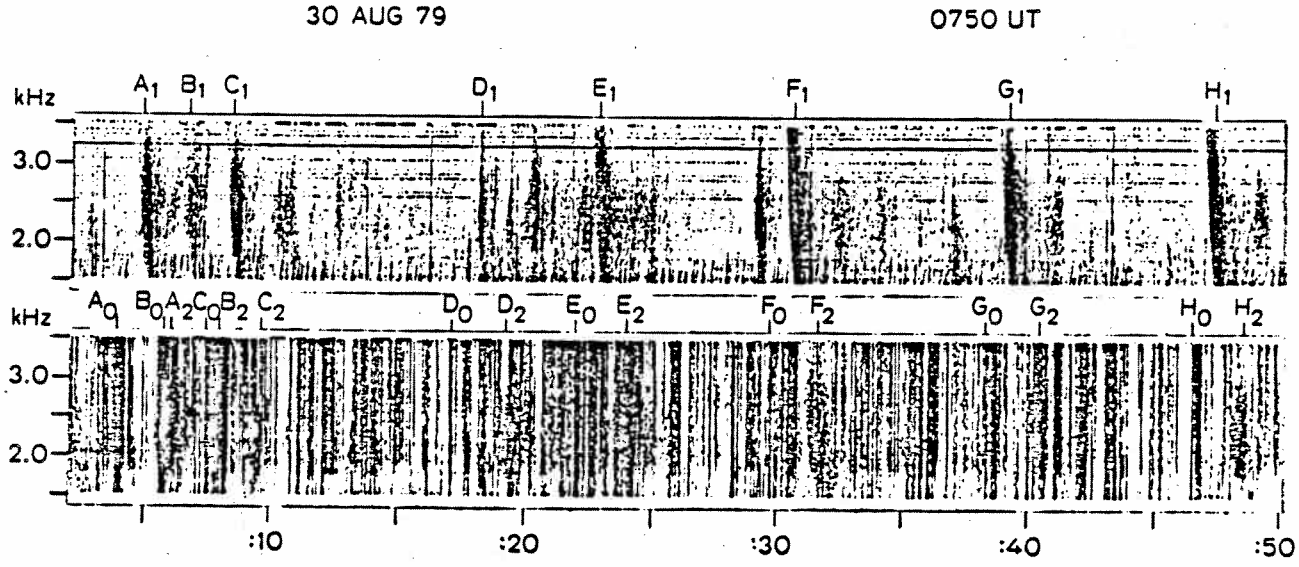

Figure 3.2 Conjugate spectrograms from (top) Siple Station and (bottom) Roberval showing whistler triggered rising emissions correlated with photometer.

outside. The two paths serve to bracket the plasmapause location. Six plasmaspheric whistlers were scaled to determine the corresponding paths and equatorial electron densities and are plotted in figure 3.3. By applying a subjective weighting factor (1 to 3), a weighted average location of the path L=2.48 was obtained with a corresponding equatorial electron density of 1750 cm^{-3}.

Fewer whistlers were measurable on the path outside of the plasmapause. Two of the best were scaled for both the condition of a collisionless plasma and for the condition of a diffusive equalibrium plasma. These serve to bracket the higher latitude path to L between 4.0 and 5.7 and the equatorial density on the path to N_{eq} between 3.6 and 26 cm^{-3}.

From figure 3.3 it can be seen that the plasmapause falls between

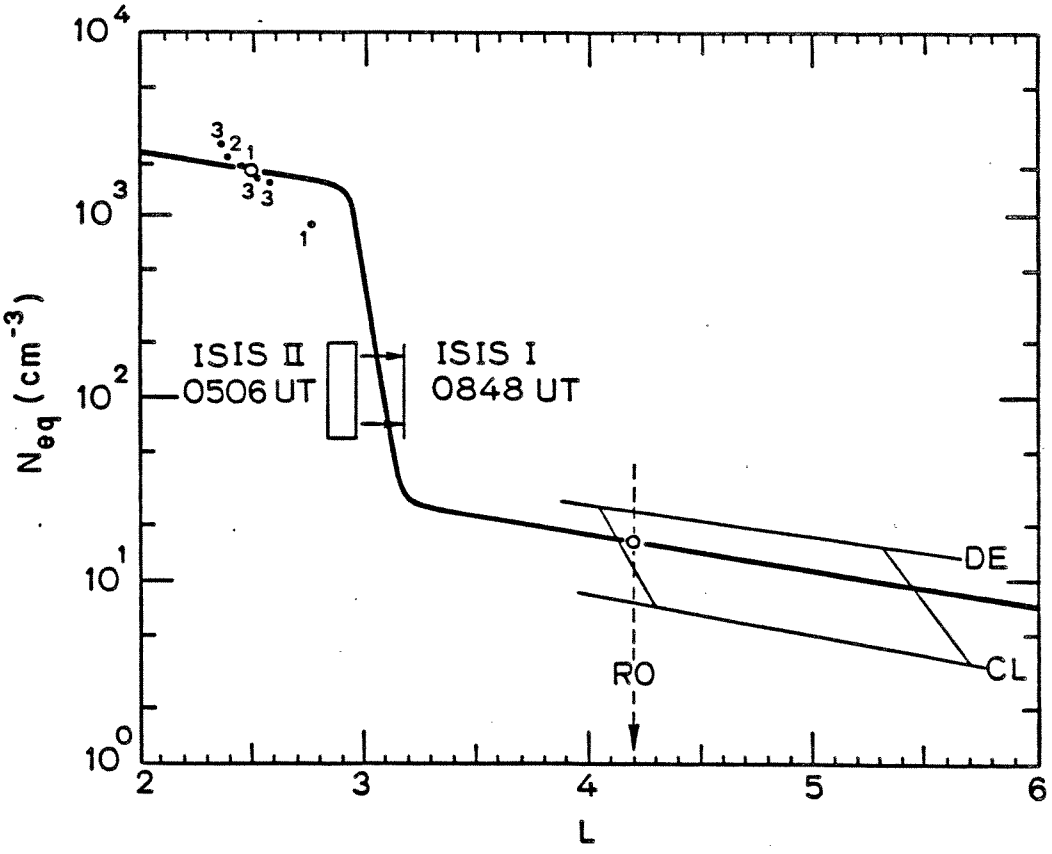

Figure 3.3 Equatorial electron density as a function of L showing plasmapause location at time of photometric correlation with VLF waves, August 30, 1977.

L=2.5 and 4.0 which is typical of the recovery stage after a magnetic disturbance. For Roberval at L=4.2 the equatorial density can be estimated as $N_{eq}=17 \pm 9$ cm^{-3}. Thus the path of propagation for the VLF signals responsible for overhead optical emissions at Roberval is well outside of the plasmapause.

Greater time resolution spectrograms of the VLF events shown in figure 3.2 suggest that rising emissions were triggered by the whistlers at a frequency of about 2 kHz. In order to determine whether the direct or mirrored precipitation mode better explained the data, the arrival

time model was run for a 0.6 second long 2 kHz wave propagating on the L=4.2 field line. An equatorial density of 17 cm^{-3} was assumed for both diffusive equilibrium and collisionless plasma models. The mean arrival time for direct precipitation results in the electrons leading the two-hop whistler signals by 0.50 seconds for the DE model and 0.90 seconds for the CL model. For mirrored precipitation the electrons lag the two-hop whistlers by 0.51 and 0.38 seconds, respectively for the two models. A comparison to the 0.7 second average lead time measured for the photometer peaks relative to the two-hop waves at Roberval leaves no doubt that this event is described by the direct mode of precipitation.

The correlations occurred during an interval of magnetic quieting following a fairly intense magnetic substorm. The K_p index for the last five days of August shows in figure 3.4 that the disturbance reached a peak of K_p=8- about 13 hours before the correlations were observed. During the correlations the index had relaxed to about K_p=4-.

The circumstance of the August 30, 1979 VLF/Photometer correlation at Roberval is generally in agreement with previous correlations made at Siple station. In all cases the correlations have occurred in the recovery period following magnetic disturbances. Wave propagation in each case has been outside the plasmapause where the equatorial cold plasma density is typically less than 50 cm^{-3} (one case, SI July 24, 1977 showed $N_{eq} \simeq 100\ cm^{-3}$). The injection of large quantities of energetic electrons into the magnetosphere due to a substorm may also be a necessary condition for the occurrence of measurable VLF wave-induced electron precipitation.

A better definition of the plasmapause location on August 30, 1979

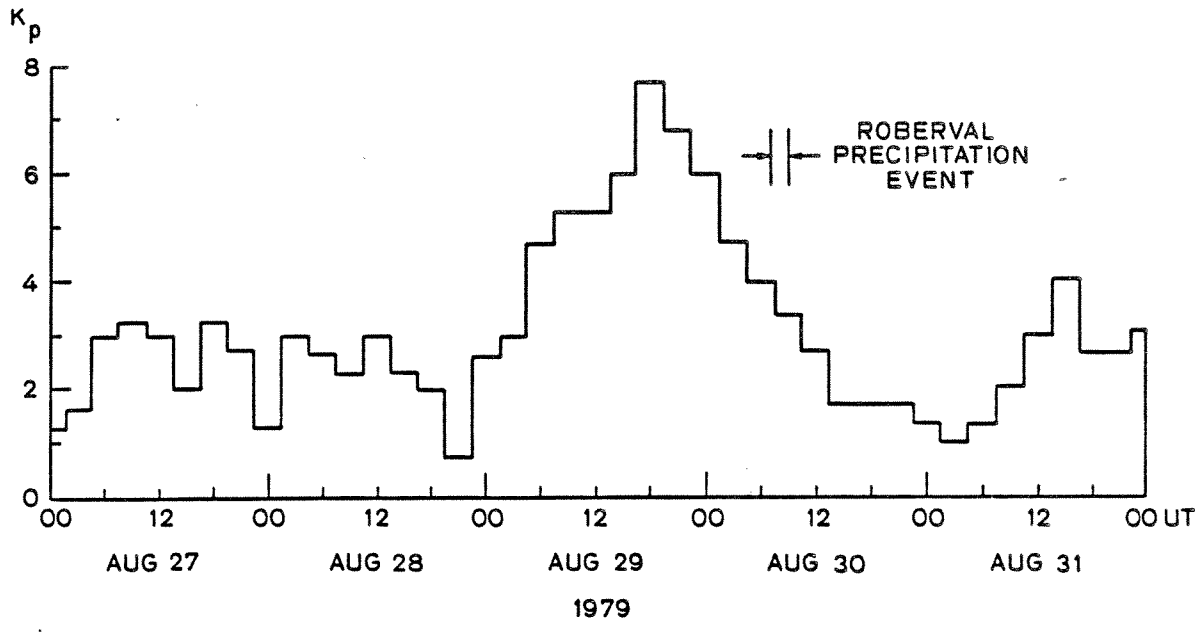

Figure 3.4 K_p index of magnetic activity showing that the Roberval precipitation event occurred during the recovery period following a magnetic storm.

can made by examining the VLF data from ISIS-I and II for an abrupt spatial cutoff of whistlers using the method of Carpenter et al.(1968). The VLF receivers were turned on during three passes of the satellite between 0454 and 2111 UT. At 0847:30 UT, at the end of an ISIS-I pass, the satellite had not yet entered the plasmasphere at L=3.18 when the receivers turned off. Several hours earlier ISIS-II encountered the plasmapause at 0502:55 UT ± 10 seconds, corresponding to L=2.89 ± 0.06. Much later, as the plasmasphere relaxed slightly, the next pass of ISIS-I at 2107:00 located the plasmapause at L=2.99 +0.28,-0.05. The satellite results are plotted on figure 3.3, showing that the plasmapause location during the VLF/Photometer correlations was about

$L=3.0 \pm 0.2$.

During the interval of the VLF/Photometer correlations at Roberval, a SAR arc was observed at about L=2.7 to 2.8 by a photometer chain run by Battelle Pacific Northwest Laboratories (D. W. Slater, private communications). The location of the plasmapause as determined by ground and satellite VLF data seems to be consistent with previous reports that place the SAR arcs in very close proximity to it (e.g. Carpenter, 1971; Chappell et al., 1971; Nagy et al., 1972).

Chapter IV

SIMULATION OF IONIZATION ENHANCEMENTS ASSOCIATED WITH WAVE-INDUCED ELECTRON PRECIPITATION

A. Introduction

Energetic electrons scattered into the loss cone by interaction with VLF waves in the equatorial region will precipitate into the ionosphere causing additional ionization, heating, optical emissions and bremsstrahlung x-rays. In this chapter we examine the temporal change in the ionospheric electron density profile as a function of height due to typical precipitation fluxes associated with equatorial scattering by VLF waves.

A computer program developed by several other authors (e.g. da Rosa, 1966; Waldman, 1971; Bernhardt, Park and Banks, 1975) is used to simulate the unperturbed ionosphere. The effect of precipitation is then introduced by including additional terms in the ionization production rate.

The model separates the ionosphere into three regions, as shown in the block diagram in figure 4.1. The upper region (above 3000 km) is assumed to act as a finite volume thermal plasma reservoir following a procedure used by Park and Banks (1974, 1975). The temperature of the upper region is assumed to remain constant while the plasma density is allowed to vary as protons and electrons flow across the lower boundary.

In the middle region (500 to 3000 km) the neutral atmosphere consists of atomic hydrogen, helium and oxygen. The dominant ion

species are O^+ and H^+, therefore the continuity equations for each must be solved. The electron and ion temperature profiles are determined by assuming that the heat flux is constant with altitude in this region.

The neutral constituents of the lower region (100 to 500 km) are atomic and molecular oxygen and molecular nitrogen. The major ion is O^+ while ions with lesser concentrations (N_2^+, O_2^+ and NO^+) are referred to as minor ions. The ion density profiles are found by solving the continuity and momentum transfer equations using the upper boundary values for temperature and O^+ concentration provided by the middle ionosphere solution and the lower boundary values for temperature and ion concentration found by assuming thermal and chemical equilibrium at the 100 km level.

B. The Continuity Equation

The ionospheric plasma is influenced by many processes acting simultaneously. Some of the more important are described by the continuity equation, the momentum transport equation for ions and the heat equation.

The time rate of change in concentration (n) of any constituent ion in a parcel of unit volume at a given height is described by the continuity equation,

$$\frac{\partial n}{\partial t} = Q - L - \nabla\cdot(n\vec{V}) \qquad (4.1)$$

where Q and L are the total production and loss rates for the species due to all processes. The divergence term expresses the net change in

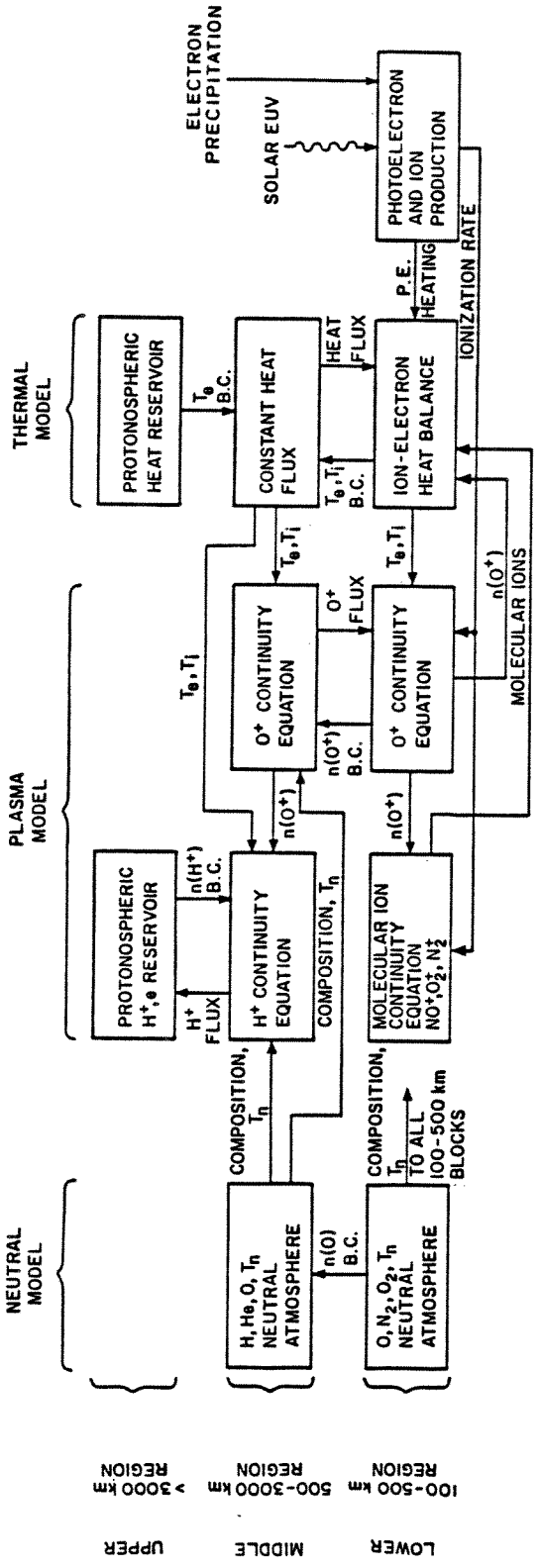

Figure 4.1 Block diagram of the model ionosphere simulation

concentration of the species due to mechanical transport at an average velocity $\vec{V}$.

The primary source of ion-electron pair production in the daytime ionosphere is photoionization due to solar radiation. An additional production source results from corpuscular ionization due to an influx of energetic electrons, protons and cosmic rays. While corpuscular ionization is negligible in comparison to solar photoionization, it can become the dominant source in the absence of sunlight at night.

The loss of electrons in the ionosphere can result from chemical or mechanical processes. In the E and lower F regions where densities of the ionospheric constituents are greater, chemical processes are most important while in the less dense regions at higher altitudes diffusion dominates. Three general types of chemical reactions are responsible for the recombination of free electrons. Radiative recombination occurs when an electron combines with an atomic positive ion to yield a neutral atom and a photon of radiant energy.

$$e^- + X^+ \longrightarrow X + h\nu$$

When an electron combines with a molecular positive ion to yield separate neutral atoms, the process is called dissociative recombination.

$$e^- + XY^+ \longrightarrow X + Y$$

Free electrons can also combine with neutral atoms to yield atomic

negative ions through a process called attachment.

$$e^- + X \longrightarrow X^-$$

The products of each reaction become immediately available to enter into further chemical reactions. The negative ion products of attachment enter into collisional or associative detachment reactions which quickly release the captured electron. In the D region the rate of detachment is of the order of the rate of attachment and the processes can contribute significantly to the electron concentration. At heights above the D region the rate of detachment is much greater than the rate of attachment and therefore the latter is not an important loss mechanism. Which reactions will be most important in influencing the total loss rate at any height depends on the relative abundance of the interacting constituents. In the computer simulation the concentrations of all species are found at each step in time.

C. The Momentum Transfer Equation

Mechanical transport also can have an effect on the concentration of a species. The rate of change of the momemtum of a unit volume of an ionospheric species is described by the momentum transfer equation. A rigorous derivation can be obtained from Boltzmann's equation (Spitzer, 1962). The time derivative of the momentum for a unit volume must equal the total of all forces acting on the parcel. These forces can be due to gradients in pressure within the species considered or friction resulting from collisions with particles of any species. External

forces resulting from the gravitational, electric and magnetic fields will also influence the momentum transfer equation. The production or loss of particles within the parcel will involve further net changes in the momentum. The momentum transfer equation including all of these terms can be expressed as (e.g. Waldman, 1971)

$$\frac{d}{dt}(nm\vec{V}) = n\vec{F} - \vec{\nabla}p + \sum_j (\vec{V}_j - \vec{V})mn\nu_j - Lm\vec{V} + Qm\vec{V}_Q \qquad (4.2)$$

where: $\vec{F}$= sum of external forces acting on a particle of the species

p= isotropic partial pressure of the species

$\sum_j$= summation over all species other than the one considered

ν_j = frequency of collisions with species "j" = $n_j\sigma_j V$

$\vec{V}_Q$= average velocity of particles of the species produced within the parcel

$\vec{V}$= bulk (average) velocity of the species

$\vec{V}_j$= average velocity of the colliding species "j"

m= mass of a particle of the species

n_j= concentration of colliding species "j"

σ_j= impirically obtained cross-section for collisions with species "j"

By applying the perfect gas law, continuity equation and charge neutrality, and by assuming that spatial gradients exist only in the vertical direction, Waldman (1971) has shown that the vertical component of the plasma velocity (v) for the species considered can be written as

$$v = u + \frac{g}{\nu}\sin^2 I - D\left\{\frac{1}{n}\frac{\partial n}{\partial h} + \frac{1}{T}\frac{\partial T}{\partial h}\right\} \qquad (4.3)$$

where: I= magnetic dip angle

D= ambipolar diffusion coefficient = $2kT/m\nu$

ν= total collision frequency = $\sum_j \nu_j$

T= average temperature = $(T_e + T_i)/2$

u= vertical plasma drift velocity due to horizontal electric fields and neutral winds

$u = U_z \sin I - (E_x/B) \cos I$

U= bulk velocity of an equivalent single background species = $\Sigma V_j \nu_j$

U_z= field aligned component of u

V_j= average velocity of species "j"

Equation (4.3) is essentially that derived by Ratcliffe and Weekes (1960) with an additional term to include plasma drift.

D. The Concentration Equation

Equation (4.3) relates the major ion density, temperature and plasma velocity. The vertical plasma velocity equation (4.3) can now be used to eliminate the velocity from the continuity equation (4.1) giving a second order partial differential equation for the major ion density,

$$\frac{\partial n}{\partial t} = Q - L - u\frac{\partial n}{\partial h} - \frac{\partial}{\partial h}\left\{D\left[\frac{nmg}{2kT} - \frac{\partial n}{\partial h} - \frac{n}{T}\frac{\partial T}{\partial h}\right]\right\} \qquad (4.4)$$

assuming a constant drift velocity (i.e. $\partial u/\partial t=0$). Expanding the last derivative, the equation can be rewritten in the form

$$\frac{\partial n}{\partial t} = Q - L - u\frac{\partial n}{\partial h} + D\left\{\frac{\partial^2 n}{\partial h^2} + A\frac{\partial n}{\partial h} + Bn\right\} \qquad (4.5)$$

where:

$$A = \frac{\nu}{T}\frac{\partial}{\partial h}\left(\frac{T}{\nu}\right) - \frac{mg}{2kT} + \frac{1}{T}\frac{\partial T}{\partial h}$$

$$B = \frac{\nu}{T}\frac{\partial}{\partial h}\left(\frac{T}{\nu}\right)\left\{-\frac{mg}{2kT} + \frac{1}{T}\frac{\partial T}{\partial h}\right\} - \frac{m}{2kT}\frac{\partial g}{\partial h} + \frac{mg}{2kT^2}\frac{\partial T}{\partial h} - \frac{1}{T^2}\left(\frac{\partial T}{\partial h}\right)^2 + \frac{1}{T}\frac{\partial^2 T}{\partial h^2}$$

Equation (4.5) is referred to as the "concentration equation" since it describes the density of an ion species as a function of height at any time provided that the temperature profile and local production and loss rates are known. It is valid for the major ion of the mixture, but can also be used to find the minor ion concentrations by including a modified description for the temperature and gravitational field. For minor ions the diffusion coefficient depends simply on the ion temperature T_i and not on the electron temperature T_e since the minor ions need not follow the same distribution as the electrons. Thus unlike the major ions for which $T=(T_i+T_e)/2$, the temperature to be used in equation (4.5) for each species of minor ions is $T=T_i/2$.

Equation (4.5) for major ions assumes charge neutrality. The vertical electric field which causes the electron and major ion height distributions to be the same has been derived by Waldman (1971) as

$$E_z = -\frac{\bar{m}_i}{\left(1+\frac{T_i}{T_e}\right)}\frac{g}{e}\sin I \qquad (4.6)$$

where: $\bar{m}_i$ = mass of the major ion

The force of the electric field on an ion of a minority species can be

combined with that of the gravitational field such that

$$m_i g \sin^2 I + eE_z \sin I = m_i \left\{ 1 - \frac{\frac{\bar{m}_i}{m_i}}{\left(1 + \frac{T_i}{T_e}\right)} \right\} g \sin^2 I \qquad (4.7)$$

We may now define an effective field term g' for minor ions such that

$$g' = g \left\{ 1 - \frac{\frac{\bar{m}_i}{m_i}}{\left(1 + \frac{T_i}{T_e}\right)} \right\} \qquad (4.8)$$

When g' is substituted for g and the temperature is given by $T=T_i/2$, then the concentration equation (4.5) is also valid for minor ions.

The solution of the concentration equation (4.5) requires a knowledge of all of the coefficients. The production rates, loss rates and vertical drift velocities as a function of height for each species are found from models as described below.

The coefficients A and B depend on the ion and electron temperatures which are obtained through solutions of the heat equations. The heat equations, in turn, depend on the electron concentration and therefore the coupled system of partial differential equations must be solved simultaneously in order to simulate the ionosphere.

E. The Heat Equation

The heat equation for a species, applicable both for electrons and ions, expresses the time variations of the thermal energy contained in a unit volume of space. It is derived from Boltzmann's equation and, following Waldman (1971), can be expressed as

$$\frac{\partial}{\partial T}\left(\frac{3}{2}nkT\right) = \frac{\partial}{\partial T}\left(\frac{3}{2}nkT\right)_{ext} - \nabla\cdot\left(\frac{3}{2}nk\vec{v}\right) + \nabla\cdot\left(B_c T^{5/2}\nabla T\right) - nkT(\nabla\cdot\vec{v}) \qquad (4.9)$$

where k is the Boltzmann constant and B_c is a thermal conductivity constant.

The first term on the right accounts for thermal variations due to external sources or sinks. These include the production and loss of particles, absorption and emission of radiation, and thermal exchange with other species. The term can be expressed as

$$\frac{\partial}{\partial T}\left(\frac{3}{2}nkT\right)_{ext} = (Q - L)\frac{3}{2}kT + Q_H - L_H$$

where Q and L are the production and loss rates for the particular species and Q_H and L_H represent the net rates of thermal energy input and loss.

The second term on the right of equation (4.9) expresses the net heat flux divergence which results from particles flowing in or out of the unit volume. The third term accounts for the divergence of the heat flux because of a gradient in temperature where the thermal conductivity of an ionized gas is given by $K=B_c T^{5/2}$ (Spitzer, 1962). The last term expresses the heat lost by a gas as it expands.

After expanding some of the derivatives, applying the continuity equation (4.1), and assuming that gradients exist only in the vertical direction, the heat equation (4.9) can now be written as

$$\frac{\partial T}{\partial t} = \frac{Q_H - Q_L}{C} + \frac{\sin^2 I}{C}\frac{\partial}{\partial h}\left\{K\frac{\partial T}{\partial h}\right\} - V_z\frac{\partial T}{\partial h} - \frac{3}{2}T\frac{\partial V_z}{\partial h} \qquad (4.10)$$

where: C is the heat capacity of the gas at constant volume, 3kn/2

V_z is the vertical component of the bulk velocity of the species

K is the thermal conductivity of the gas = $B_c T^{5/2}$

B_c is a thermal conductivity constant

Herman and Chandra (1969) have shown that the last two terms are small compared to the others in equation (4.10) and therefore can be neglected. The resulting heat equation for electrons is

$$\frac{\partial T_e}{\partial t} = \frac{1}{C_e}\left\{Q_H - L_H^{ei} - L_H^{en} + \sin^2 I \frac{\partial}{\partial h}\left(K_e \frac{\partial T_e}{\partial h}\right)\right\} \qquad (4.11)$$

where K_e is the thermal conductivity for electrons and the heat loss rates L_H^{ei} and L_H^{en} are determined using published expressions for electron-ion (Mantas, 1973) and electron-neutral (Banks and Kockarts, 1973) thermal transfer processes.

The heat equation for ions is similar to that for electrons, but simplified because the ion thermal conductivity is very small. By simplifying the conduction term, the ion heat equation can be reduced to a non-linear, yet first order partial differential equation (Antoniadis, 1976)

$$\frac{\partial T_i}{\partial t} = \frac{1}{C_i}\left\{L_H^{ei} - L_H^{in} + \frac{5}{2}K_i^* T_i^{3/2} \sin^2 I \left(\frac{\partial T_i}{\partial h}\right)^2\right\} \qquad (4.12)$$

which is easier to solve than the electron heat equation. The term L_H^{ei} appears as heat production in equation (4.12) since electrons give up energy to the ions which are at a lower temperature. The ion-neutral heat transfer process contributes a net loss of heat (L_H^{in}) from the ion population. In the derivation of the ion heat equation (4.12) the ionic gas is assumed to be dominated by O^+ such that the ion thermal conductivity can be given by (Banks, 1967)

$$K_i = K_i^* T^{5/2}$$

where $K_i^* = 1.2 \times 10^{-4}$ eV cm^{-1} s^{-1} ^{0}K$^{-7/2}$

The heat equations for both electrons (4.11) and ions (4.12) can be expressed as implicit difference equations and solved using the method of Laasonen (1949). The technique used in the simulation program is based on a procedure formulated by da Rosa (1966).

F. O^+ Concentration

In addition to ion production, diffusion and vertical transport by neutral winds and electric fields, the concentration of O^+ is also controlled by losses through chemical reactions. The principal reactions and their corresponding reaction rates (γ_{O_2} and γ_{N_2}) are given in table 4.1. The loss rate for O^+ can be expressed as

$$L = \gamma_{O_2} [O_2][O^+] + \gamma_{N_2}[N_2][O^+]$$

where the square bracket notation indicates the "concentration of" a reacting species. While this loss process is not strictly exponential, it is common practice to express it in terms of a linear differential equation of the form

$$L = \frac{dn}{dt} = - \beta n$$

where

$$n = n_o e^{-\beta t}$$

and β represents the linear loss rate.

Table 4.1

IONOSPHERIC REACTIONS

Reaction	Reaction Rate	Reference
$O^+ + O_2 \longrightarrow O_2^+ + O$	$\gamma_{O_2} = 1.6\times10^{-11}$	Stubbe (1969)
$O^+ + N_2 \longrightarrow NO^+ + N$	$\gamma_{N_2} = 5.0\times10^{-13}$	Stubbe (1969)
$O_2^+ + e \longrightarrow O + O$	$\alpha_{O_2} = 7.0\times10^{-8} (\frac{1000}{T_e})$	Whitten et al. (1964)
$N_2^+ + e \longrightarrow N + N$	$\alpha_{N_2} = 2.8\times10^{-7} (\frac{1000}{T_e})^{3/4}$	Whitten et al. (1964)
$NO^+ + e \longrightarrow N + O$	$\alpha_{NO} = 4.7\times10^{-8} (\frac{1000}{T_e})^{3/2}$	Whitten et al. (1964)
$O_2 + N_2^+ \longrightarrow N_2 + O_2^+$	$\delta_{O_2} = 1.0\times10^{-10}$	Fehsenfeld et al. (1965)
$O + N_2^+ \longrightarrow NO^+ + N$	$\delta_O = 2.5\times10^{-10}$	Fehsenfeld et al. (1965)
$O_2^+ + NO \longrightarrow NO^+ + O_2$	$\varepsilon = 8.0\times10^{-10}$	Mitra (1968)

G. Finite Difference Form of the Concentration Equation

The differential equation (4.5) describing the temporal variation in ion concentration at a given altitude is found to be non-linear in terms of the dependent variables u and n. However by expanding the non-linear expressions in a Taylor series and neglecting all but the first order terms, the non-linearities can be removed without affecting the validity of the equation (Antoniadis, 1976). The partial differential equation can then be expressed as a finite difference equation. Using the implicit method of Crank and Nicolson (1947), each spatial derivative is written as a weighted sum of expressions which describe the finite vertical differences in concentration at consecutive steps in time. The implicit scheme is unconditionally stable as it is applied here. The resulting finite difference form of the concentration equation for each species is (Waldman, 1971):

$$\frac{x_i - n_i}{\Delta t} = Q_i - \frac{1}{2}\beta_i (x_i + n_i) - \frac{u}{4\Delta h}(x_{i+1} + n_{i+1} - x_{i-1} - n_{i-1}) +$$

$$+ D_i \frac{1}{2(\Delta h)^2}(x_{i+1} + n_{i+1} - 2x_i - 2n_i + x_{i-1} + n_{i-1}) +$$

$$+ \frac{A_i}{4\Delta h}(x_{i+1} + n_{i+1} - x_{i-1} - n_{i-1}) + \frac{B_i}{2}(x_i + n_i) \qquad (4.13)$$

where

$$x_i = n_{i,j+1}$$

$$n_i = n_{i,j}$$

$$Q_i = Q_{i,j+1/2}$$

$$\beta_i = \beta_{i,j+1/2}$$

$$u = u_{j+1/2}$$

$$D_i = D_{i,\, j+1/2}$$

$$A_j = A_{i,\, j+1/2}$$

$$B_i = B_{i,\, j+1/2}$$

and the subscripts i and j refer to indexes of height and time, respectively.

When applied to the entire range of heights, equation (4.13) expands into a linear system of equations for each step in time. The method of solution for a system of banded matrices used in the ionospheric simulation program is Gauss elimination (Richtmeyer, 1957) which requires the specification of two boundary conditions.

The lower boundary is chosen to be 100 km where a large recombination rate will assure that the ion concentrations will be in equilibrium. Assuming that losses are exponential (i.e. $L=\beta x$), then for equilibrium (i.e. $L=Q$) the lower boundary condition is specified by

$$x_i = Q/\beta$$

When the top boundary concentration is also specified for the lower region, then the entire lower region profile can be obtained at successive steps in time, through a recurrent application of equation (4.13). The top boundary O^+ concentration is obtained by solving for the density profile in the middle region (500 to 3000 km) as described below.

H. Minor Ions

The complexity of equation (4.13) results from the inclusion of the non-linear term which describes plasma diffusion. Because the density of the neutral atmosphere decreases with height, diffusion is an important process affecting ion concentrations above 250 km. The major ion species O^+ is found in abundance above this height and therefore the diffusion term must be included in the concentration equation. However the minor ions (O_2^+ , N_2^+ and NO^+) are produced mainly below 200 km where greater neutral densities inhibit diffusion through collisions. While the densities of the minor ions could be determined from the full concentration equation as discussed previously, a linear form of the continuity equation can be substituted since the diffusion terms become negligible.

Minor ion production results from both solar EUV radiation and corpuscular ionization. Losses are controlled by chemical reactions with other species. Eight important reactions involving minor ions which are considered in the simulation are given in table 4.1 along with their reaction rates. While other reactions are also taking place, simulation results using only these eight have shown agreement with experimental results (e.g. Johnson, 1969). The concentration equations for the minor ions are:

$$\frac{d[N_2^+]}{dt} = Q_{N_2} - \alpha_{N_2} n_e [N_2^+] - \delta_{O_2} [O_2] [N_2^+] - \delta_O [O][N_2^+] \qquad (4.14a)$$

$$\frac{d[O_2^+]}{dt} = Q_{O_2} + \gamma_{O_2} [O_2][O^+] + \delta_{O_2} [O_2] [N_2^+] - \alpha_{O_2} [O_2^+] n_e - \varepsilon [NO][O_2^+] \quad (b)$$

$$\frac{d[NO^+]}{dt} = \delta_O[O][N_2^+] + \gamma_{N_2}[N_2][O^+] + \varepsilon[NO][O_2^+] - \alpha_{NO}[NO^+]n_e \qquad (c)$$

Thus the ion loss rates depend on the sum of the rates of the contributing reactions, each of which depends on the product of the concentrations of the necessary reactants. The electron concentration at any location is found through charge neutrality by adding up the concentration of all of the ions.

$$n_e = [O^+] + [N_2^+] + [NO^+] + [O_2^+]$$

I. The Upper Plasmasphere

In order to obtain an accurate description of the lower ionosphere (100 to 500 km) it is necessary to include the flow of plasma and heat across the upper boundary. This can be done by considering the upper region (above 3000 km) to be a finite volume thermal plasma reservoir following the method of Park and Banks (1974, 1975). The reservoir maintains a constant temperature and acts as a source or sink for electrons and protons flowing across the upper boundary of the middle region (500 to 3000 km). Using these boundary conditions, the temperature and density profiles for the middle region are found by simultaneously solving the continuity, momentum transfer and heat equations. The lower boundary values for the middle region then provide the upper boundary values for the lower region.

The neutral constituents of the middle region are atomic hydrogen, helium and oxygen. The ionic species O^+ and H^+ are produced and lost

through the charge exchange reaction

$$O + H^+ \rightleftharpoons O^+ + H$$

The detailed solution of the middle region of the ionosphere used in the simulation is described by Park and Banks (1974, 1975).

J. Simulation of the Ionosphere

A simultaneous analytical solution of the concentration (4.5) and heat equations (4.10) for all species can only be obtained by applying unrealistic simplifying assumptions which are inconsistent with our knowledge of the ionosphere. However realistic solutions can be obtained through self-consistent numerical simulations. The program used in the present work solves the concentration and heat equations to find the density profiles of O^+, O_2^+, NO^+, N_2^+ and H^+ ions, and the electron and major ion temperature profiles. A slight compromise to self-consistency is imposed by the vertical plasma drift (equation 4.3) since the neutral wind and horizontal electric fields are entered into the program as inputs rather than being solved for.

The simulation begins by determining the initial ion density profiles and electron and ion temperature profiles by using a steady-state analysis. In the steady-state, the change in concentrations of all constituents is zero. The finite difference equation (4.13) is therefore simplified because $n_i = x_i$ for all height steps i. A solution for the ion concentrations at each height requires that the temperature profiles for ions and electrons be specified in

order to calculate the coefficients (A, B and D). Since the temperatures depend on the concentrations, it is necessary to iterate the concentration equation with the heat equation (4.10) until the density and temperature profiles are consistent.

The initial ion and electron temperature profiles used in the first pass through the steady-state iteration process are derived from a model of the exospheric temperature variations (Roble, 1975) at the required latitude. The model includes seasonal as well as diurnal variations in the exospheric temperature distribution.

Once the initial concentration is determined from the steady-state analysis, then the dynamic simulation can proceed through successive time steps by solving the concentration equation (4.13) and the heat equation (4.10) simultaneously. The procedure taken at each step for the time varying solution is shown in figure 4.2 and is summarized as follows (after Waldman, 1971):

1) Find the neutral temperature profile. The neutral temperature T_n increases exponentially from the turbopause (top of the mixing layer) to the exosphere. The turbopause is chosen to be located at an altitude (h_t) of 120 km. A neutral temperature ($T_n(h_t)$) of 347 degrees is assumed in the mixing layer. The exospheric temperature ($T\infty$) is specified from a time varying model. The neutral temperature profile is described by an empirical relation used by Stein and Walker (1965) and Walker (1965).

$$T_n(h) = (T\infty - T(h_t))\, e^{-\alpha\Psi}$$

where $\alpha = 0.02\ km^{-1}$ and Ψ is the geopotential height measured with respect to h_t and expressed in term of the earth's radius (r_o) and

height (h).

$$\Psi = \frac{r_o + h_t}{r_o + h}(h - h_t)$$

2) Find the concentration profile for the neutral constituents. A diffusive equilibrium distribution is applied.

3) Calculate the height profiles of the ion production rates (q_O, q_{O_2}, q_{N_2}) due to solar radiation (negligible at night) and corpuscular ionization. The production rate profile which results from ionization by a monoenergetic beam of electrons is discussed in the next section.

4) Calculate the concentrations of the minor ions by integrating equations (4.14) over the interval since the previous step. The values of T_e (used to find the reaction rates) and $[O^+]$ are those obtained in the previous time step.

5) Calculate the concentration of the major ion $[O^+]$ by integrating equation (4.13) over the interval since the previous step. The values of T_e and T_i and $[O^+]_{500}$ are those obtained in the previous time step.

6) Find the electron density profile assuming charge neutrality by summing the concentrations of all ions at each height.

7) Calculate the local electron heat production rate at each height. Heat is transferred to the electron gas by energetic photoelectrons created during the ionization processes. The amount of energy transferred since the previous time step is found by integrating the heat production rate over the interval. The total heat production rate is given by the product of the average energy per photoelectron

times the ionization rate for each species, summed over all species.

8) Obtain the electron and ion temperature profiles by solving the heat equations (4.11 and 4.12) using concentrations defined in the previous time step.

9) Solve the middle region concentration and heat equations using the method of Park and Banks. This defines the upper boundary conditions for the solution of the lower region at the next time step.

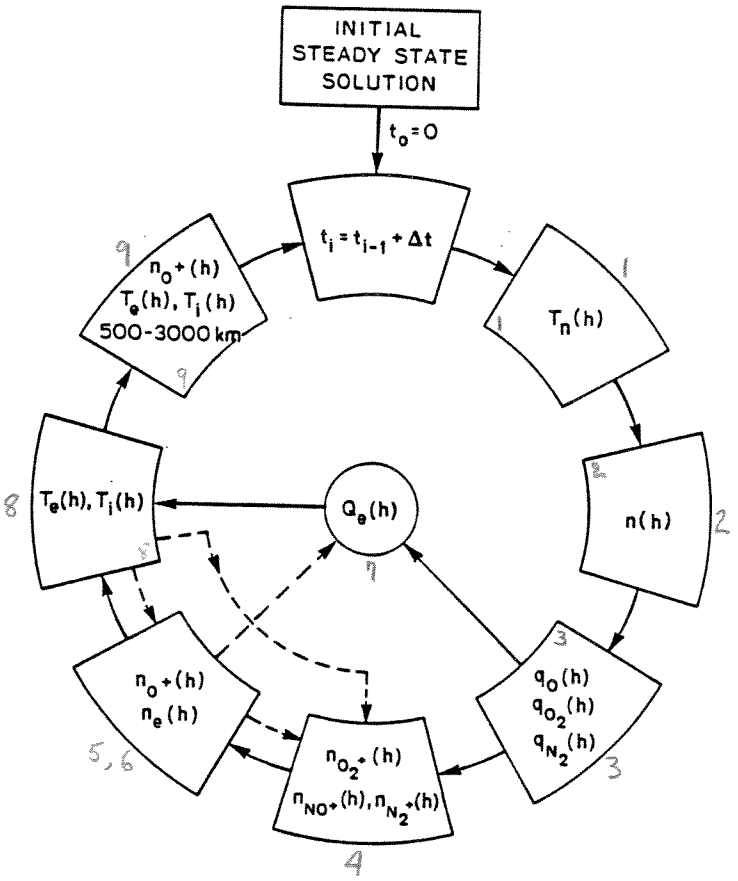

Figure 4.2 Computational sequence of ionosphere simulation

K. Ionization due to Electron Precipitation

In chapter 3 it was shown that VLF waves can scatter energetic electrons into the loss cone through cyclotron resonant interactions occurring in the equatorial region of the magnetosphere. As the loss cone electrons precipitate into denser regions in the atmosphere, they give up their kinetic energy through repeated collisions with the ionospheric constituents until they finally reach thermal equibrium with the cold electron plasma. The energy given up by the electrons goes into heating and further ionization of the ionosphere. In this section we examine the ionization rate associated with a monoenergetic electron beam in order to model the ionospheric response to electron precipitation.

Models which describe the penetration of electrons into the atmosphere have grown in sophistication in recent years. The earliest models formulated by Lewis (1950) and Spencer (1955) solved the transport equation for monodirectional, monoenergetic primary electrons. An application of the theory to auroral electrons by Chamberlain (1961) provided curves for the energy deposition as a function of altitude. Using an empirical expression obtained from laboratory data (Grün, 1957) for the energy deposition rate as a function of range for a beam of electrons in air, Rees (1963) computed the ionization rate as a function of altitude for incident beams of arbitrary energies and pitch angles. Secondary electron ionization was also included where the secondary energy distribution was obtained from theoretical or empirical data, and the fluxes of secondaries were derived from hypothetical models of the loss processes.

While the Rees method has been used to calculate ionization and optical emission rates, the model does not describe the change in energy distribution of the primary electrons as they penetrate into the atmosphere. The continuous degradation in primary energy has been computed by Maeda (1965), and Stadsnes and Maehlum (1965) who applied Monte Carlo techniques to the problem. The analysis follows many primary electrons through successive scattering collisions until they are reduced to thermal velocities. The results provide average energy deposition and ionization rate profiles.

A different method formulated by Walt et al. (1969) uses a Fokker-Planck diffusion equation to determine the distribution in energy along the path into the atmosphere. The model also includes the effect of the magnetic field convergence on the electron pitch angle. The phase space calculations consider the effect on the distribution function for collisions of primary electrons with initial energies above 10 keV. By improving angular and energy cross sections, Donat et al. (1971) extended the method down to 1 keV and Banks et al. (1974) down to 500 eV.

An improved model developed by Banks et al. (1974) follows the degradation in energy of primary and secondary electron fluxes below 500 eV. While the continuous energy loss described by the Fokker-Planck method applies for energies above 500 eV, for lesser energies angular scattering and energy losses are better represented by discrete changes (Banks and Nagy, 1970). In the energy deposition computations, the transport of low energy electrons along the magnetic field line is described by solving a two stream flux continuity equation (e.g. Nagy

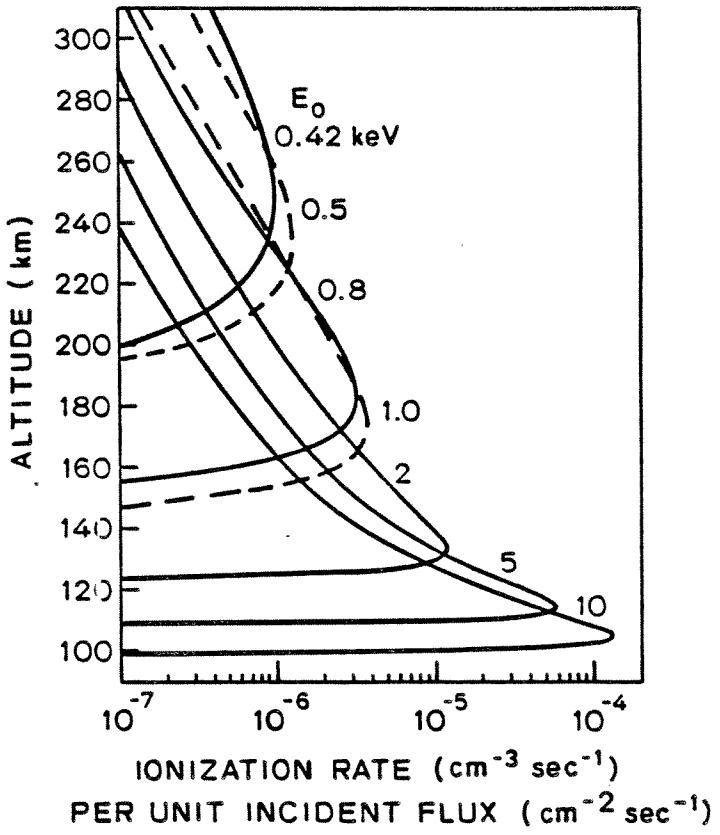

Figure 4.3 Corpuscular total ionization rate height profiles (Banks, Chappell and Nagy, 1974)

and Banks, 1970; Stolarski, 1972). A divergence of the upward and downward fluxes can be interpreted as energy losses or gains due to elastic or inelastic scattering.

Banks et al. (1974) have used the extended Fokker-Planck method to calculate the ionization rates per unit incident flux as a function of altitude as shown in figure 4.3. They assume that a beam of incident electrons is isotropic in pitch angle over the lower hemisphere and the energy distribution of the flux is nearly monoenergetic as given by a

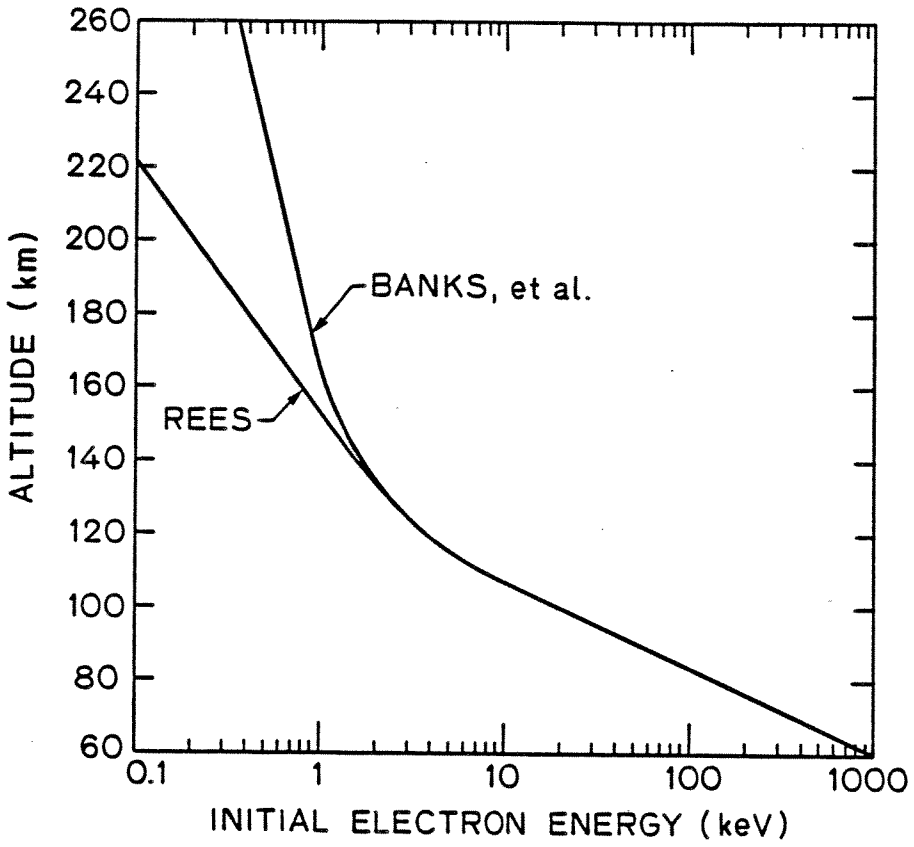

Figure 4.4 Altitude of maximum ionization rate for precipitated electrons

narrow gaussian such that

$$\Phi(E_o) = A\, e^{-50\left(\frac{E}{E_o} - 1\right)^2}$$

for characteristic initial energies $0.42 < E_o < 10$ keV and where A is a normalization factor adopted by Rees (1963, 1969). The profiles for initial energies of 2, 5 and 10 keV in figure 4.3 are in good agreement with the results obtained by Rees. For lower initial energies the

profiles peak at higher altitudes than found by Rees, thus indicating the importance of including the effect of discrete losses for soft precipitation.

A useful parameter which characterizes the effect of precipitation is the "penetration height" or altitude of maximum ionization rate. Figure 4.4 shows the penetration height as a function of the initial energy for monoenergetic beams of electrons found by using both the method of Rees and that of Banks et al.

The ionization rate per unit incident flux for monoenergetic electron beams of initial energies other than those shown in figure 4.3 can be obtained by interpolation as described in appendix 1. A FORTRAN subroutine is also given in appendix 1 which accepts an initial energy and altitude, applies the interpolation scheme and returns the required ionization rate per unit incident flux.

L. Corpuscular Ionization in the Simulated Ionosphere

The additional production of ionization caused by monoenergetic electron precipitation can now be included in the ionospheric simulation algorithm previously discussed. For a given flux and initial primary electron energy, the total ionization rate profile due to precipitation can be found from figure 4.3 through interpolation. The ionization rates of the individual atmospheric constituents can be found from the total ionization rate by applying the appropriate total ionization cross section. The rates for each species then simply add to the rates due to solar EUV radiation and the simulation of the ionosphere proceeds as usual.

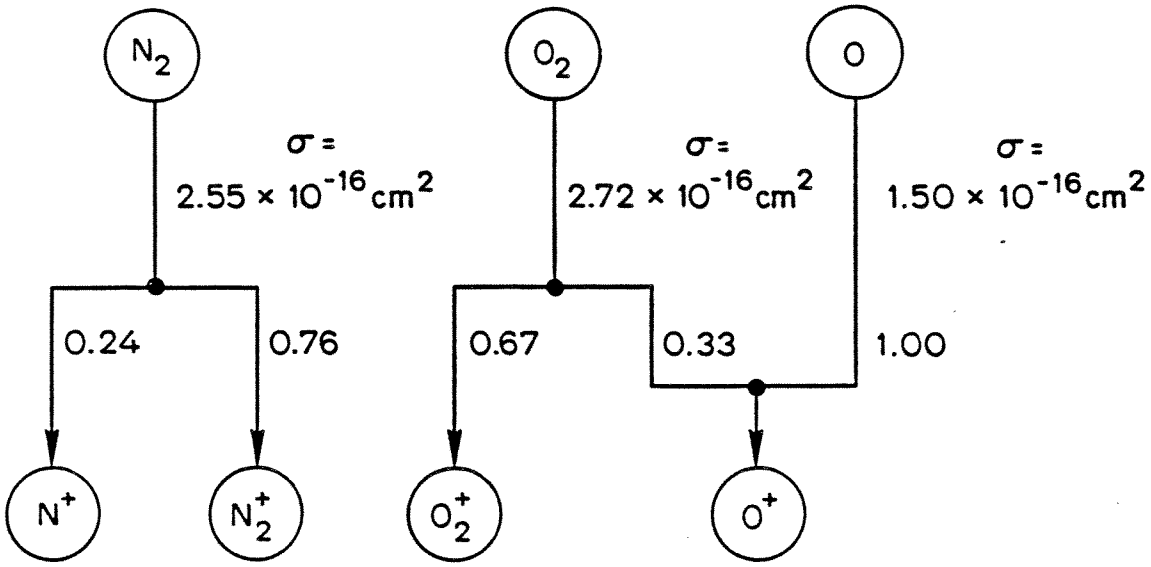

Figure 4.5 Branching schematic for corpuscular ionization

The important processes of atmospheric ion production due to electron bombardment are shown schematically in figure 4.5 where the rates at which the neutral species are ionized depends on the peak values of the total ionization cross sections $\sigma(M)$. The resulting ions, shown at the bottom of figure 4.5, will be produced in numbers which depend on the branching ratios. These are simply fractions of the total ionization of the parent neutral species that end up as a particular ion species. The branching ratios are given in figure 4.5 for each path of ionization between a parent neutral and ion species. Ionization of a neutral species is assumed to proceed at a rate proportional to the product of the peak cross section and the concentration of target particles (Jones, 1974). Thus the rate of ionization of a neutral species can be obtained by multiplying the total rate of ionization for

all species (η_{total} from figure 4.3) by the fraction of the total rate attributable to the particular species considered. In algebraic form the ionization rates of the important neutral species can be expressed as

$$\eta_{O_2} = \eta_{total}\, \gamma_{O_2}$$

$$\eta_{N_2} = \eta_{total}\, \gamma_{N_2}$$

$$\eta_{O} = \eta_{total}\, \gamma_{O}$$

where

$$\gamma_M = \frac{[M]\sigma(M)}{[O_2]\sigma(O_2) + [N_2]\sigma(N_2) + [O]\sigma(O)}$$

The ion production rates for individual ionic species (q') are found by multiplying the ionization rates for the parent neutral particles by the appropriate branching ratios. Thus we can write

$$q'_{N_2^+} = 0.76\eta_{N_2}$$

$$q'_{N^+} = 0.24\eta_{N_2}$$

$$q'_{O_2^+} = 0.67\eta_{O_2}$$

$$q'_{O^+} = 1.00\eta_{O} + 0.33\eta_{O_2}$$

M. Simulation Results

In a study of nonlinear pitch angle scattering of energetic electrons by coherent VLF waves in the magnetosphere, Inan et al. (1978) found that at L≈4 a 10 pT, 5 kHz CW wave can produce as much as 0.1 erg cm^{-2} s^{-1} precipitated energy flux of 1 keV electrons. In this section we examine the temporal change in the ionospheric electron density profile caused by a 0.01 erg cm^{-2} s^{-1} continuous precipitation flux of monoenergetic (i.e. narrow gaussian distribution) 1 keV electrons. The simulation results, therefore, correspond to an energy flux which is an order of magnitude less than the upper value predicted by Inan et al. for the given wave.

The model was run for an equinoctial nighttime ionosphere starting at 2230 local time. The geographic location was chosen to be Roberval, Quebec with a latitude of 48°N and longitude of 72°W. The magnetic invariant latitude at Roberval is about 60°N and the dip angle is about 74 degrees. A quiet time eastward electric field model is assumed.

The total ionization rate profile for 1 keV electron precipitation is shown in figure 4.3 as a dashed line obtained by interpolation as described previously. Since we are considering a nighttime effect in this example, solar EUV ionization is absent. The corpuscular ionization will therefore be the only source of production.

The electron density profiles obtained by the model for various times are shown in figure 4.6a. The curve marked t=o corresponds to the normal profile at 2230 local time in the absence of electron precipitation. Precipitation of 1 keV electrons with an energy flux of 0.01 erg cm^{-2} s^{-1} is then turned on. The equivalent number flux is

given by

$$6.24 \times 10^{6}\ \text{cm}^{-2}\ \text{s}^{-1} = (0.01\ \text{erg cm}^{-2}\ \text{s}^{-1})\ \frac{(6.24 \times 10^{8}\ \text{keV/erg})}{(1.0\ \text{keV per e}^{-})}$$

After the first minute of precipitation the profile marked t=1 shows that a noticeable density enhancement has begun. Successive curves at 2, 5, 10, 20 and 60 minutes show that as the long enduring precipitation event continues, the perturbation to the F_1 region eventually saturates. At that time a steady state is achieved between production by precipitating energetic electrons and the usual loss processes of recombination, diffusion and transport.

The ionization enhancement caused by a flux of 1 keV electrons shows the greatest change at a height of about 170 km. The effect diminishes above and below the peak in a range of heights from about 150 to 200 km. The peak and spread in the density enhancement are consistent with the shape of the ionization rate profile of figure 4.3.

During the hour sequence shown in figure 4.6a the F_2 region remains generally unaffected by the precipitation. This is because 1 keV electrons penetrating through the F_2 region cause ionization there at a rate which is an order of magnitude less than at the height of maximum ionization. The effect is further diminished because the density profile peaks in the F_2 region and therefore a larger absolute change in density is needed to noticeably alter the profile. However, the F_2 region does show a density change over the hour due to the normal diurnal relaxation after the sun sets at about 1800 local time. The normal density profile at 2330 local time is shown as a dashed curve in

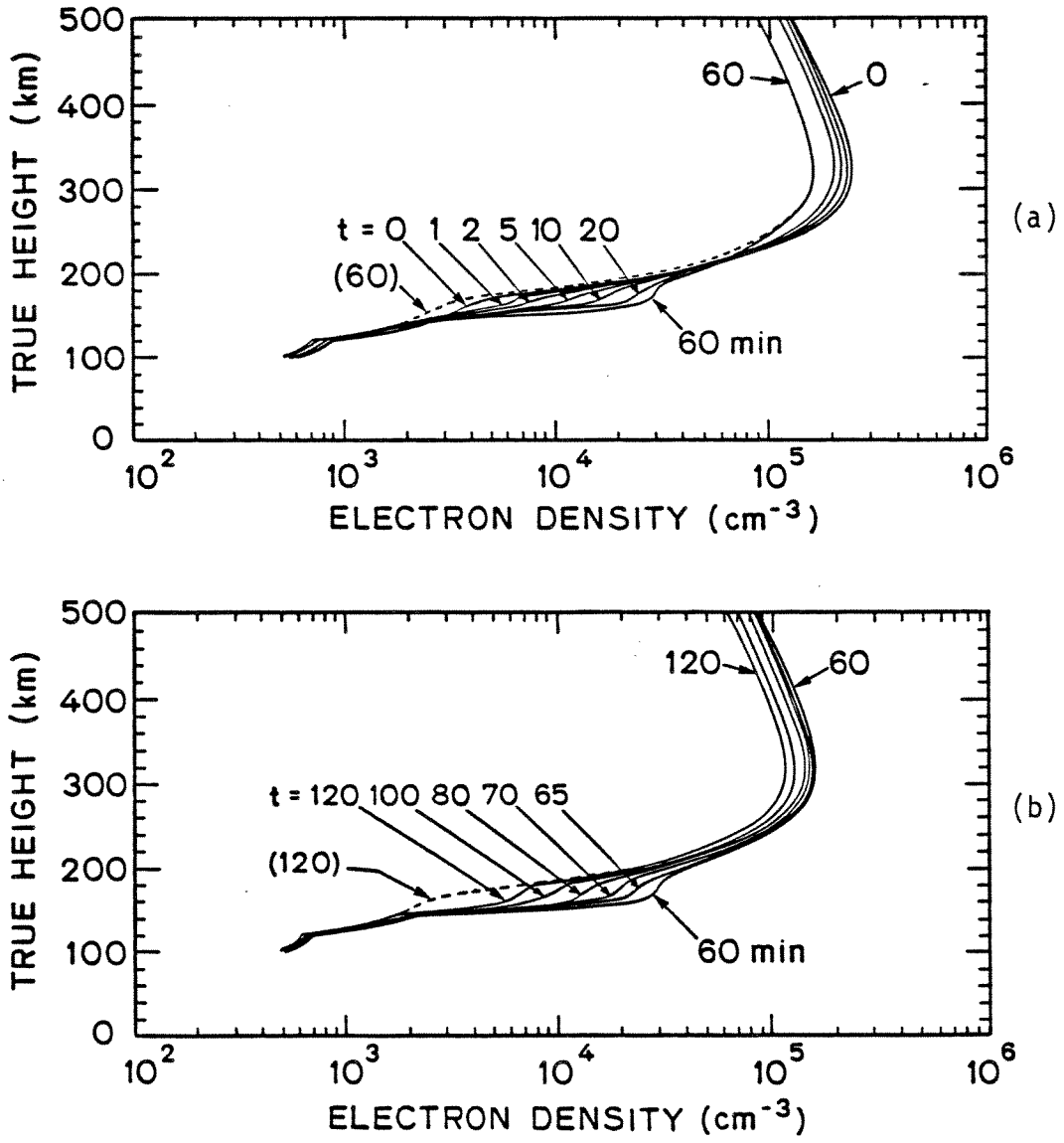

Figure 4.6 Height profile of electron density a) during precipitation event and b) during recovery

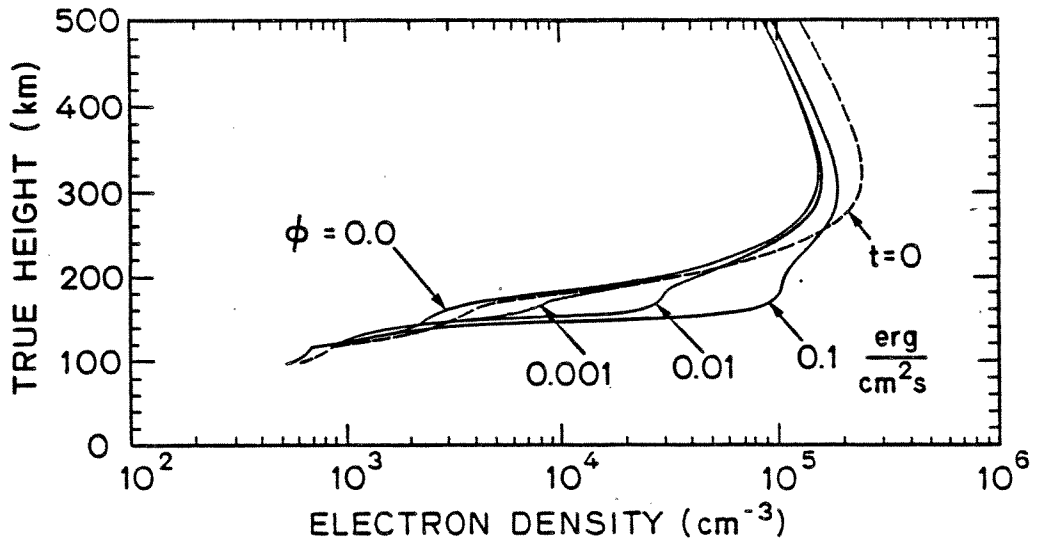

Figure 4.7 Height profiles of electron density after 1 hour of precipitation of various energy fluxes

figure 4.6a (marked "(60)"). The density profile after the precipitation has reached a steady state (marked "60 min") is therefore referenced to the unperturbed (dashed) profile for the same time. After one hour of constant precipitation, the flux is abruptly turned off at 2330 local time. The F_1 layer formed by corpuscular ionization is seen to decay as a result of recombination, diffusion and transport in the sequence of figure 4.6b.

The rate of ionization buildup due to precipitation of electrons of a given energy depends on the amount of precipitation flux. Decreasing the flux slows the buildup while increasing the flux causes the density profile to show an enhancement more quickly. The density at which saturation occurs also depends on the flux. Figure 4.7 shows an initial electron density profile (dashed curve) at 2230 local time and the

profiles one hour later for cases where there is either no precipitation (Φ=0.0) or there is a precipitation flux of 0.001, 0.01 or 0.1 erg cm^{-2} s^{-1}. The times required for saturation to occur for the three fluxes are about 100, 70 and 30 minutes, respectively.

The ionospheric time constants for the buildup of ionization due to 1 keV electron precipitation can be expressed as a function of energy flux. The electron density at a height of 170 km is plotted as a function of time for the three fluxes in figure 4.8. The normal nighttime decay of the ionosphere at that height is shown for comparison. Although a steady state is not obtained within the first 60 minutes of precipitation for the smaller fluxes, saturation densities (N_{sat}) can be estimated in those cases by projecting the curves. The buildup curves are well approximated by exponential functions such that the density at any time during the precipitation of a continuous flux of 1 keV electrons is given by,

$$N(t) = N(t_{on}) + (N_{sat} - N(t_{on})) \left\{1 - \exp\left[\frac{t_{on} - t}{\tau_b}\right]\right\} \qquad (4.15)$$

where $N(t_{on})$ is the electron density at the time when the precipitation begins. This expression can be solved for the time constant (τ_b) for the buildup, such that

$$\tau_b = \frac{-t}{\ln\left\{1 - \frac{N(t) - N(t_{on})}{N_{sat} - N(t_{on})}\right\}}$$

The time constant is then found by using the model results which define

the density (N) at any time for the energy fluxes shown in figure 4.8. The time constants for ionization buildup at the 170 km height are plotted as a function of the precipitation energy flux in figure 4.9. An empirical expression obtained by fitting a curve to the model time constants gives the time constant in minutes as

$$\tau_b \simeq - 11 \ (\log \Phi + 0.4) - 2$$

It shows that the ionospheric response time decreases linearly with a logarithmic increase in energy flux for 1 keV electron precipitation.

An increase in energy flux also results in an increase of the saturation electron density which is reached in the steady state. The value of N_{sat} corresponding to a given energy flux can be estimated from figure 4.10 where the model results are fitted by a straight line on a log-log plot. An empirically derived formula which describes the functional relationship is

$$\log N_{sat} = 0.51 \log \Phi + 5.48$$

where the units of saturation density are cm^{-3}.

The relaxation of the ionosphere at a height of 170 km in the absence of any sources of ion production is dominated by processes of recombination while second order contributions to the total decay can be attributed to diffusion and transport. The loss rate for recombination depends on the product of the concentrations of electrons and positive ions. Assuming charge neutrality, the decay can be described

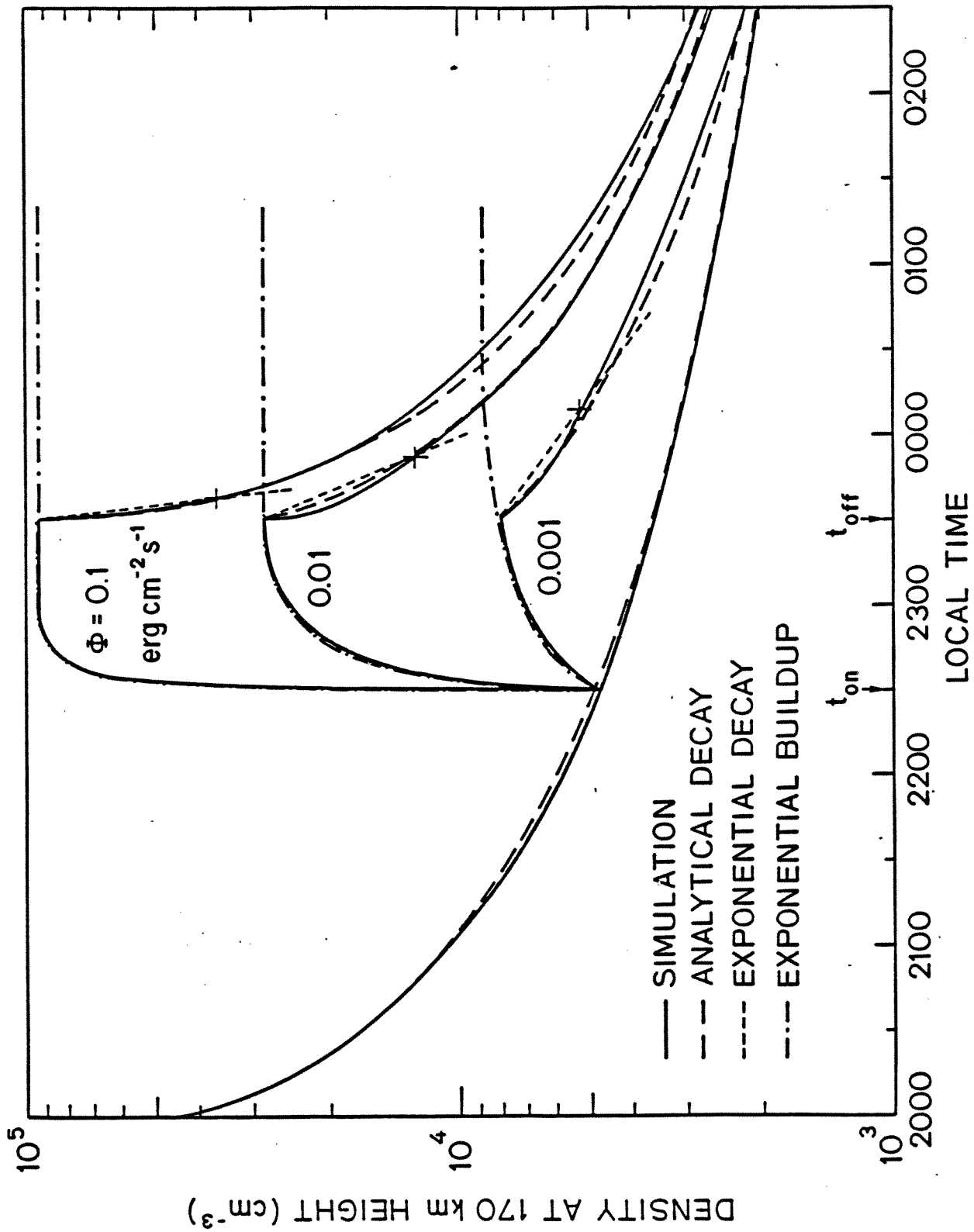

Figure 4.8 Temporal change in density at 170 km height due to various energy fluxes of 1 keV precipitation.

(Ratcliffe, 1972) by

$$\frac{dN}{dt} = -\alpha N^2$$

where α is a decay coefficient. Solving the differential equation, the density as a function of time becomes

$$N(t) = \left[\alpha(t - t_o) + \frac{1}{N_o}\right]^{-1} \qquad (4.16)$$

where N_o is the initial (t_o) density. Thus the decay coefficient can be determined from a knowledge of the temporal variation of the density, such that

$$\alpha = \frac{\frac{1}{N(t_2)} - \frac{1}{N(t_1)}}{(t_2 - t_1)}$$

The decay coefficient for the normal diurnal decay after sunset is found from the model results of figure 4.8 to be $\alpha \approx 1.2 \times 10^{-6}$ cm^3/min. The dashed curve in the figure shows the density variation found by using that value of the decay constant. It shows close agreement with the model over a six hour period. The relaxation of ionization due to precipitation is described by a different decay coefficient from that which fits the normal diurnal curve. For the three energy fluxes of 1 keV electron precipitation considered in figure 4.8, a common value of 1.9×10^{-6} cm^3/min satisfactorily describes (dashed curve) the simulation results (solid curve).

The difference between the decay coefficients in the solar EUV and

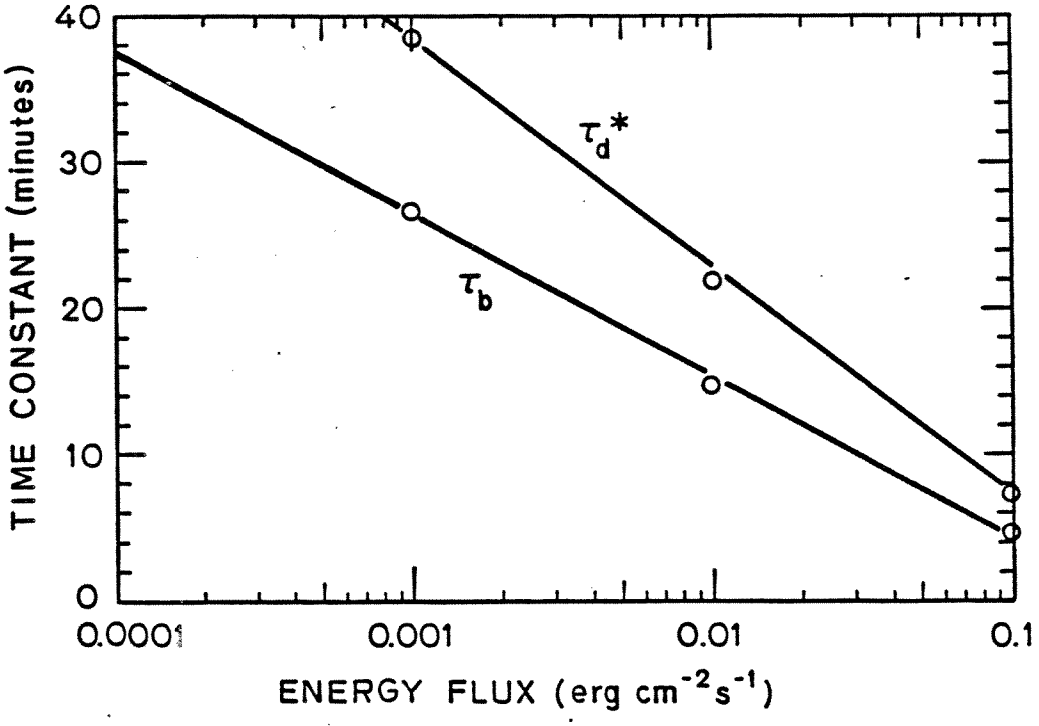

Figure 4.9 Time constant of ionization buildup at 170 km height as a function of energy flux for 1 keV precipitation.

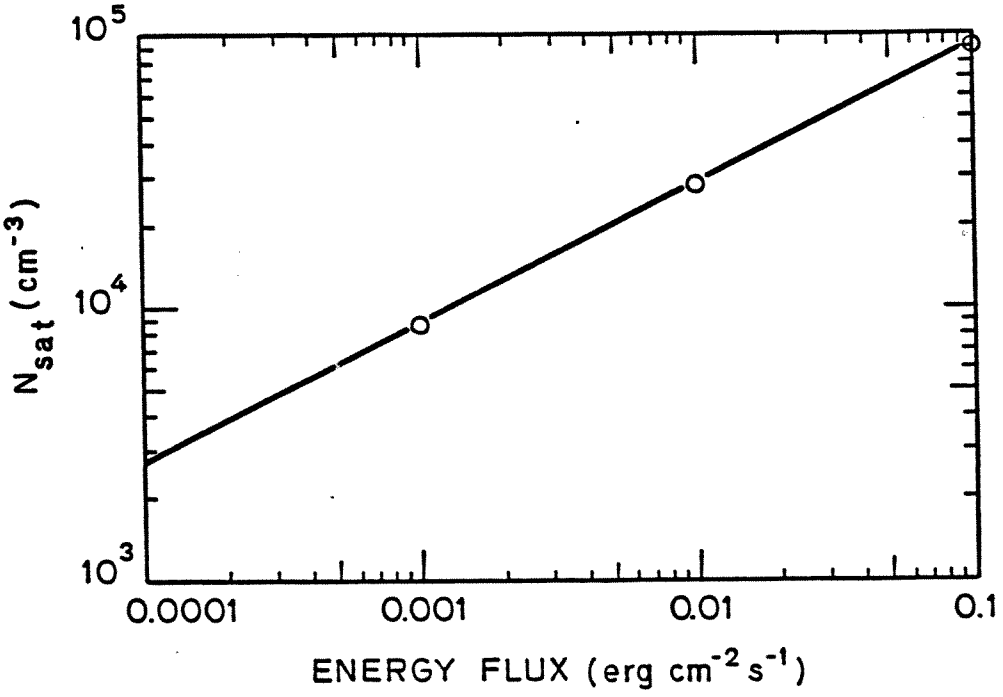

Figure 4.10 Saturation density at 170 km height as a function of energy flux for 1 keV precipitation.

corpuscular ionization recovery periods can be understood by noticing again from figure 4.3 that ionization due to monoenergetic precipitation is more localized in height than is photoionization. While rates of recombination should be the same in each case for the same instantaneous density, the decay coefficient also reflects the losses which result from diffusion. From equation (4.5) it can be seen that losses associated with diffusion will depend not only on the local density, but also on the vertical density gradient. Larger local density gradients in the case of corpuscular ionization will result in a greater temporal change in concentration and therefore a larger value for the decay coefficient than obtained for recovery from photoionization.

Although the decay of ionization is not described by an exponential function, the instananeous rate of change can be treated as such in order to define an equivalent relaxation time τ_d (Ratcliffe, 1972).

Let $$\frac{dN}{dt} = -(\alpha N)N$$

then $$N(t) = N_o e^{-\frac{t}{\tau_d}}$$

where $$\tau_d = (\alpha N)^{-1}$$

The equivalent relaxation time for normal decay after sunset and during the recovery period following 1 keV electron precipitation are plotted as a function of density in figure 4.11. The figure shows that as the

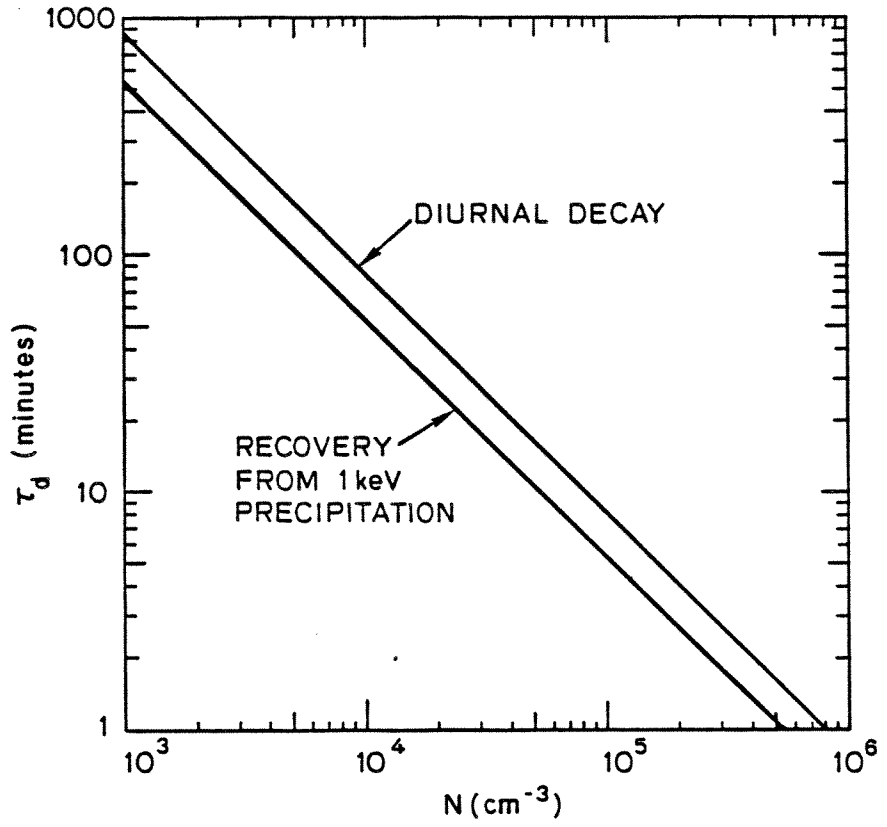

Figure 4.11 Equivalent relaxation time at 170 km height as a function of density

density decreases, the relaxation time increases and the recovery process slows down. The fastest change will therefore occur when the density is greatest. For ionization caused by precipitation we can compare the time constant for buildup and the shortest possible relaxation time constant, which is the value associated with the saturation density. For the cases where energy fluxes are 0.1, 0.01 and 0.001 erg cm^{-2} s^{-1}, the time constant ratio $\tau_d(N_{sat})/\tau_b$ is 1.16, 1.25 and 2.22, respectively. Thus the buildup is always faster than the decay.

Since the equivalent relaxation time varies with density, as shown in figure 4.11, it is useful to define an effective time constant for

exponential decay (τ_d^*) as the time required for the density to decrease to 1/e of the amount that the saturation density is greater than the normal diurnal density (N_D). Thus,

$$N(t) = N_D(t) + (N_{sat}-N_D(t))\, e^{-\left(\frac{t - t_{off}}{\tau_d^*}\right)}$$

where t_{off} is the time when precipitation ends and recovery begins. The density at a time when $t = t_1 = t_{off} + \tau_d^*$ can be found through iteration since the diurnal density is also time varying. For the first iteration the diurnal density at $t=t_1$ is assumed to be the same as when the precipitation is turned off (i.e. $N_D(t_1)=N_D(t_{off})$). The density therefore decays from N_{sat} at $t=t_{off}$ to an approximate value when $t=t_1$ given by

$$N(t_1) \simeq \frac{1}{e}\, N_{sat} + (1 - \frac{1}{e})\, N_D(t_{off})$$

The time when the approximate value of $N(t_1)$ is reached can be found from figure 4.8 or from equation (4.15) where $\alpha=1.9\times10^{-6}$ cm^3/min and $N_o=N_{sat}$. Now an updated value of the diurnal density $N_D(t_1)$ can be obtained from figure 4.8 or from equation (4.15) where $\alpha=1.2\times10^{-6}$ cm^3 per minute and $N = N_D(t_{off})$. The iteration continues, using the updated values, until the effective time constant for decay is defined to sufficient precision.

Effective time constants for decay have been calculated for the saturation densities associated with the three energy fluxes of 1 kev precipitation shown in figure 4.8. For fluxes of 0.1, 0.01 and 0.001

erg cm^{-2} s^{-1} the effective time constants are about 7.5, 22 and 38.5 minutes, respectively. The effective exponential decay is plotted as a straight dotted line in figure 4.8. A comparison between the rates of buildup and decay can be seen in figure 4.9. The recovery from an enhancement of ionization caused by 1 keV electrons generally is about 50 percent slower than the buildup.

Chapter V

DETECTION OF PERSISTENT ELECTRON PRECIPITATION USING IONOGRAMS

A. Introduction

The first pulsed observations of the ionosphere were made by Breit and Tuve in 1926. Today the pulse-echo technique is the most widely used method for obtaining a profile of the ionospheric electron density. In practice, a short pulse (typically less than 1 msec) is transmitted at a given frequency in the range of 0.2 to 20 MHz. The wave propagates to a height in the ionosphere where it is reflected and then the echo is received back on the ground after a delay of a few milliseconds. The delay between transmission and reception of a pulse can be measured by various techniques. The simplest of these uses an oscilloscope to display the amplitude of the receiver output as a function of time, where the start of the sweep is synchronized with the beginning of the transmitter pulse. Multiplying the measured delay by the speed of light gives us an equivalent total distance which the wave would have traveled if it had propagated entirely through free space. If the wave ray direction is assumed to deviate negligibly from the vertical, then a virtual height is defined as being half of the total equivalent path.

The pulse-echo technique can be used at a single frequency to monitor fluctuations in the virtual height at a particular density level. However, if the frequency is varied, then the virtual height over a range of density levels is found. In the sweep frequency mode,

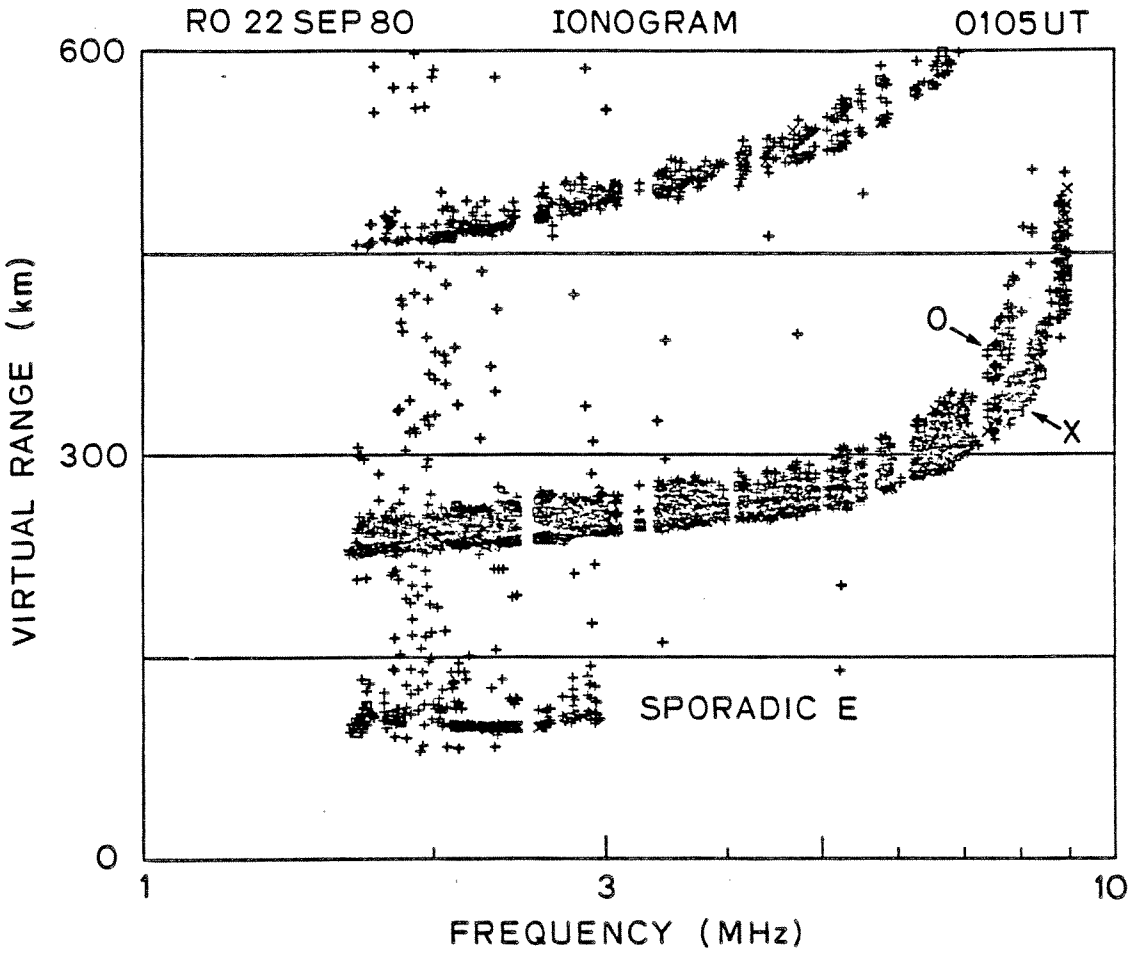

Figure 5.1 Post-sunset ionogram from Roberval, Quebec

the transmitter and receiver frequencies are stepped synchronously. The usual display for a sweep frequency ionosonde plots virtual height as a function of wave frequency. This can be done most easily by using an oscilloscope with the receiver amplitude controlling the z-axis intensity. The y-axis (virtual height) sweep is synchonized with the start of the transmission, as before, and the x-axis deflection is controlled by a voltage ramp which is proportional to the log of the frequency.

In recent years, sophisticated digital techniques of data processing have been applied to the return echoes in real time

(e.g. Wright, 1969; Paul, et al., 1974). An example of a typical post-sunset digital ionogram obtained at Roberval, Quebec is shown in figure 5.1. Both ordinary (O) and extraordinary (X) traces are evident. Echoes from the decaying E layer would be seen below 1.6 MHz at the time of the example if the lower frequencies had been transmitted. The example shows sporadic E layer echoes which are returned up to about 3 MHz. At most of the frequencies transmitted the signals penetrate through the E layer to the F_2 region. At frequencies above the critical values for each mode, HF waves will pass through the ionosphere and no echoes are returned.

B. Refractive Index

In an isotropic ionized medium the group velocity of a wave (v_g) is directly proportional to the index of refraction (n).

$$v_g = n\ c$$

In free space the index of refraction is unity for all frequencies and the group velocity is simply the speed of light. However, for an ionized gas in the presence of a magnetic field, such as is the case for the ionospheric plasma, the refractive index and group velocity depend in a complicated way on the frequency of the wave, direction of propagation and parameters which describe the medium.

For ionospheric sounding with HF waves, free space propagation can be assumed between the ground and the lower ionospheric boundary (i.e. the daytime D region or nighttime E region). As the wave penetrates

into the ionosphere, the refractive index and group velocity vary because of an increase in the electron density with height. When the group velocity decreases, the pulse envelope is said to be retarded by the medium. The effect of retardation is to cause a large portion of the total measured delay to occur near the top of the path.

Eventually a height may be reached where the vertical component of v_g goes to zero and the wave is reflected. Snell's Law states that at a plane interface between two homogeneous media,

$$n_1 \sin \phi_i = n_2 \sin \phi_r = \text{constant}$$

where ϕ_i and ϕ_r are the angles of incidence and refraction, respectively, as measured between the wave normal and the perpendicular to the interface. For vertical incidence, the wave normal is also perpendicular to the interface plane and therefore $\phi_i = \phi_r = 0^o$. Figure 5.2 shows that the vertical incidence wave normal (as indicated by the direction of the wave number k) is aligned with the normal to the interface plane (i.e. the z direction). A wave vertically incident on a horizontally stratified medium will therefore penetrate with its wave normal vertical at all heights. The presence of a magnetic field, however, will impose an anisotropy on the refractive index and the direction of energy flow (i.e. the ray direction) will in general differ from the wave normal direction. The ray path will be considered in the following section.

The height profile of the complex refractive index for a wave of a given frequency can be obtained by applying the Appleton-Hartree

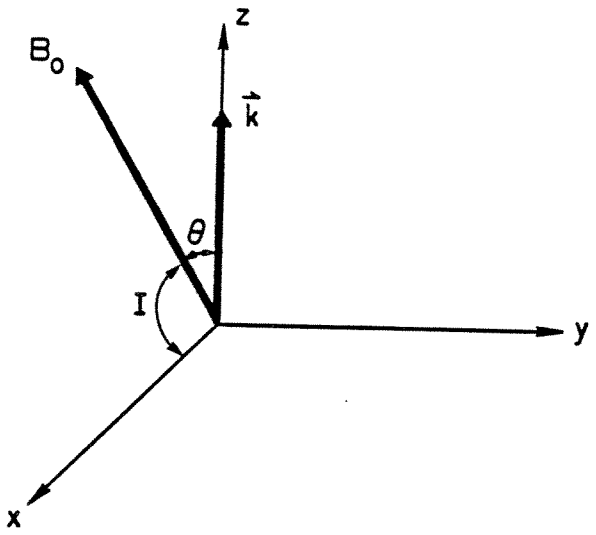

Figure 5.2 Orientation of wave normal relative to the direction of the magnetic field for vertical incidence

dispersion equation to a known density profile. The standard form of the general expression (e.g. Budden, 1961; Kelso, 1964) when the effects of ions are neglected is given by

$$n_{\pm}^2 = 1 - \frac{X}{(1-jZ) - \frac{Y_T^2}{2(1-X-jZ)} \pm \left[\frac{Y_T^4}{4(1-X-jZ)^2} + Y_L^2\right]^{1/2}}$$

where

$$X = \left(\frac{\omega_o}{\omega}\right)^2 = \left(\frac{f_o}{f}\right)^2$$

$$Y_T = Y \cos\alpha$$

$$Y_L = Y \cos\gamma$$

$$Y = \frac{\omega_H}{\omega} = (Y_L^2 + Y_T^2)^{1/2}$$

$$Z = \frac{\nu}{\omega}$$

f_o is the plasma frequency = $(80.6 \times 10^{-6}\ N)^{1/2}$ (MHz)

N is the plasma density (cm^{-3})

Cos α and cos γ are the direction cosines of the components of the magnetic field which are transverse and logitudinal, respectively, to the direction of the wave normal. At heights above the E region the collision frequency (ν) can be neglected and the dispersion equation reduces to

$$n_{\pm}^2 = 1 - \frac{2X(1 - X)}{2(1 - X) - Y_T^2 \pm \left[Y_T^4 + 4Y_L^2(1 - X)^2\right]^{1/2}} \qquad (5.1)$$

The dispersion equation has two solutions, each describing the refractive index for a characteristic wave propagating in the birefringent medium. For transverse propagation, the characteristic wave associated with the upper sign is called the ordinary mode while the other, associated with the lower sign, is called the extraordinary mode. For other orientations of the wave normal with respect to the magnetic field it is sometimes difficult to distinguish between the modes based on the polarization of the waves. The usual convention of naming the modes is to use the sign rule as defined for transverse propagation.

Figure 5.3 shows a plot of the square of the refractive index (e.g. Davies, 1965; Kelso, 1964) as a function of the normalized plasma frequency (X) for the cases where Y<1 in panel (a) and Y>1 in panel (b). General solutions to equation (5.1) are restricted to the shaded regions bounded by the solutions for longitudinal and transverse propagation. Vertical cross-hatched areas are associated with the ordinary mode (+) and horizontal cross-hatched areas indicate the extraordinary mode (-).

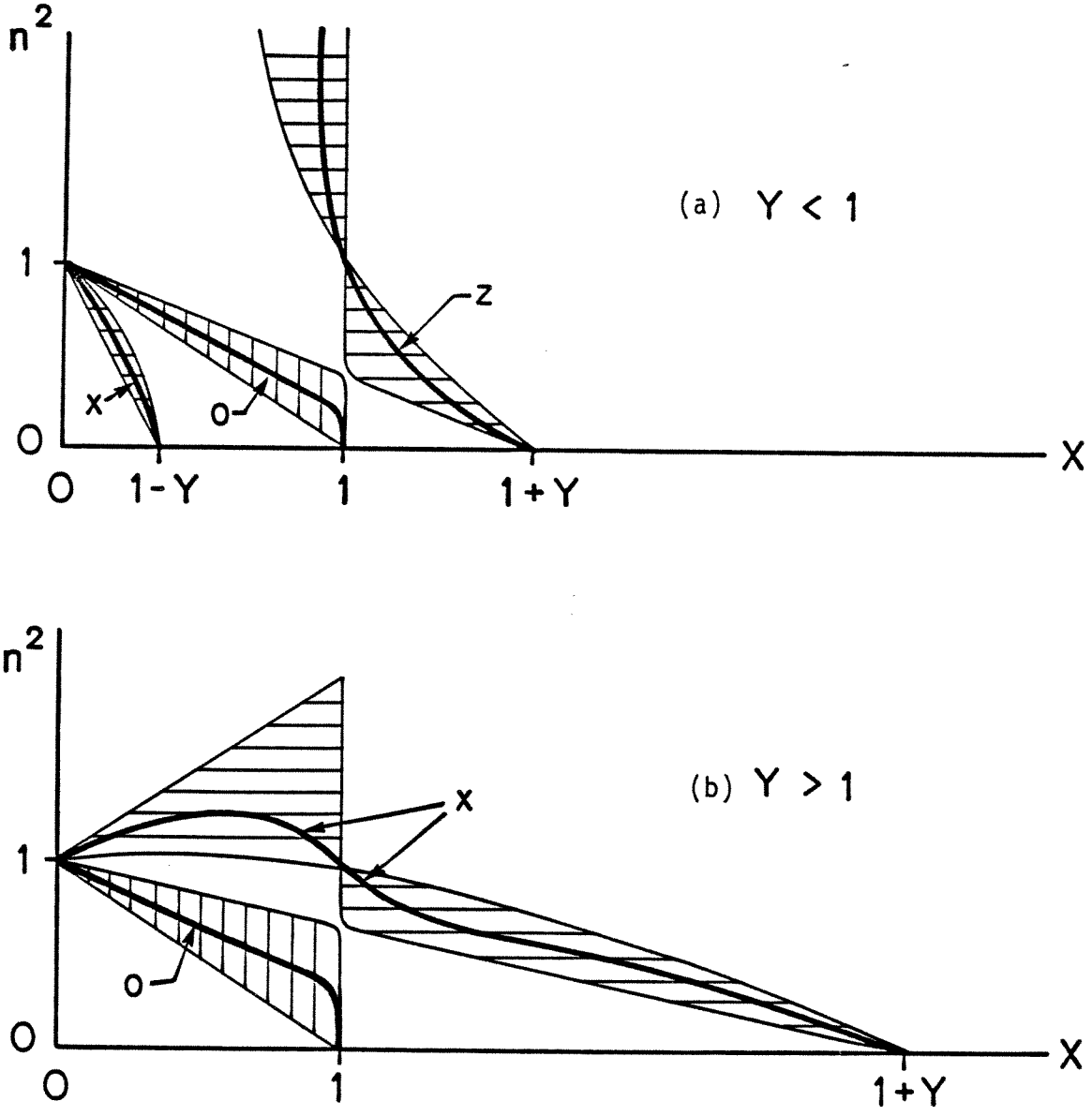

Figure 5.3 Dispersion curves for cases where a) Y < 1 and b) Y > 1

The refractive index is unity for free space (i.e. X=0) propagation. For the ordinary mode, both when Y<1 and when Y>1, the refractive index decreases to zero as the normalized plasma frequency increases to X=1. For the extraordinary X mode when Y<1, the critical value of the normalized plasma frequency where n=0 is obtained at X=1-Y. An additional branch seen in figure 5.3a reaches a critical value at X=1+Y. This branch is also due to the lower sign in equation (5.1) and is known as the extraordinary Z mode. At middle and high latitudes, wave energy from the ordinary mode can couple to the Z mode (Eckersley, 1950; Rydbeck, 1950). However in this report the discussion will concentrate on the dominant ordinary O and extraordinary X modes.

When Y>1 the extraordinary mode dispersion is more complicated. For normalized plasma frequencies of X<1, the wave propagates in the whistler mode and the refractive index is greater than one. For wave frequencies which are less than the plasma frequency (X>1), the extraordinary mode refractive index is less than one and goes to zero at a critical value of X=1+Y.

Reflection of a vertical incidence wave occurs when the refractive index goes to zero. The height of reflection (h_r) for a vertically incident wave of a given frequency can be obtained directly from a known density profile. For the ordinary mode the density at the reflection height is given by,

$$X_r = 1$$

$$f_{o_r} = f$$

$$N(h_r) = \frac{f^2}{80.6 \times 10^{-6}} \quad cm^{-3} \qquad (5.2a)$$

where the wave frequency (f) is in units of MHz. For the extraordinary mode, when Y<1,

$$X_r = 1 - Y$$

$$f_{o_r} = f(1-Y)^{1/2}$$

$$N(h_r) = \frac{f^2(1 + Y)}{80.6 \times 10^{-6}} \quad cm^{-3} \qquad (5.2b)$$

and when Y 1,

$$X_r = 1 + Y$$

$$f_{o_r} = f(1+Y)^{1/2}$$

$$N(h_r) = \frac{f^2(1 + Y)}{80.6 \times 10^{-6}} \quad cm^{-3} \qquad (5.2c)$$

A height profile of the refractive index for a wave of a given characteristic mode and frequency can be obtained from a known density profile through application of equation (5.1). The applicable branch of the dispersion relation is determined by the choice of signs and on whether Y<1 or Y>1. The gyrofrequency varies slowly over the range of ionospheric heights and thus a constant f_H of 1.5 MHz is a good approximation at a geomagnetic latitude of 60 degrees.

The refractive index for a 2 MHz ordinary mode wave is shown as a function of height in figure 5.4 for a typical density profile at 2230 local time, obtained from the model ionosphere seen at t=0 in figure 4.6. In the lower ionosphere the refractive index for the 2 MHz wave is nearly the same as it is for free space. At greater heights the plasma

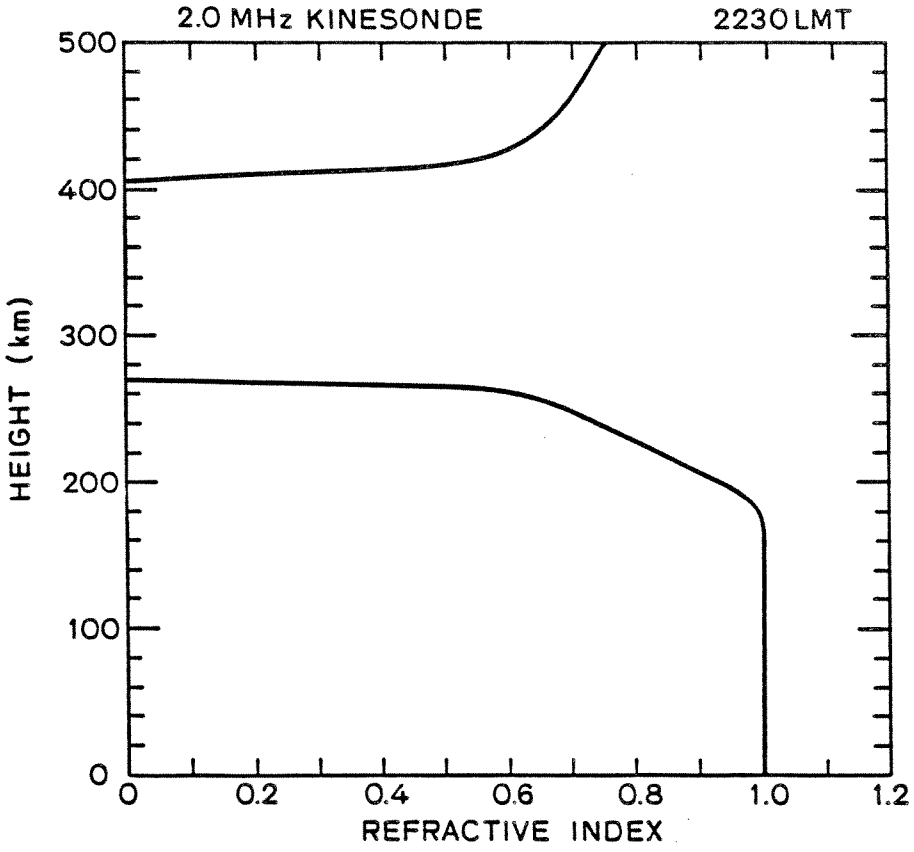

Figure 5.4 Height profile of refractive index for an ordinary mode 2 MHz wave

density increases and the refractive index decreases until it reaches zero at the reflection height for a vertically incident wave. The rapid decrease within about 5 km of the reflection height shows that the greatest retardation of the group velocity occurs near the top of the path. A similiar refractive index curve is seen above the height of the density profile maximum. A vertically incident topside sounder signal transmitted from a satellite will penetrate downward until its refractive index also goes to zero at a reflection height.

C. Group Path

The apparent distance traveled by an HF signal is referred to by

names such as the group path, equivalent path, apparent path, or virtual path. It is obtained by supposing that the pulse travels in free space at the speed of light (c). Thus the group path is

$$P' = c\ t'$$

where t' is the measured group delay time between transmission of a pulse and reception of the echo returned from the ionosphere. The group delay can be expressed in terms of the integral over the path of the wave group velocity (v_g), such that

$$t' = \int_{path} \frac{ds}{v_g}$$

At the top of the path, for a vertically incident wave, the group velocity goes to zero and therefore the integral cannot be solved in this form. However, a solution can be obtained if we express the integral in terms of the phase velocity. Using the definitions of phase velocity ($v_p = \omega/k$) and group velocity ($v_g = \partial\omega/\partial k$), we can write

$$\frac{1}{v_g} = \frac{\partial k}{\partial \omega} = \frac{\partial(\omega/v_p)}{\partial \omega}$$

Differentiating,

$$\frac{1}{v_g} = \frac{1}{v_p} + \omega \frac{\partial(1/v_p)}{\partial \omega}$$

The group path now can be written as

$$P' = c\int_{path}\left[\frac{1}{v_p} + f\frac{\partial(\frac{1}{v_p})}{\partial f}\right]ds$$

where $f=2\pi\omega$. While the phase velocity goes to infinity at the top of the path, it appears in the denominator of the integrand and thus the integral converges. Using the definition of the index of refraction $n=c/v_p$,

$$P' = \int_{path} n\ ds + f\int_{path}\frac{\partial n}{\partial f}\ ds \qquad (5.3)$$

Thus the group path is found from integrals of the refractive index and its frequency derivative, both of which are well behaved over the path.

D. Virtual Height

A wave which is vertically incident on a horizontally stratified ionosphere will penetrate with its wave normal vertical at each height as required by Snell's Law. The presence of the geomagnetic field, however, imposes an anisotropy on the index of refraction, causing the ray direction to deviate from the vertical. As a result, the point of reflection can be displaced horizontally several kilometers from the point where the wave enters the ionosphere.

The reflection point displacement can be illustrated by considering the Poeverlein (1949) method for graphical construction of typical ray paths as shown in the upper panels of figure 5.5. Panel (a) applies to the ordinary mode, while (b) and (c) describe the extraordinary mode

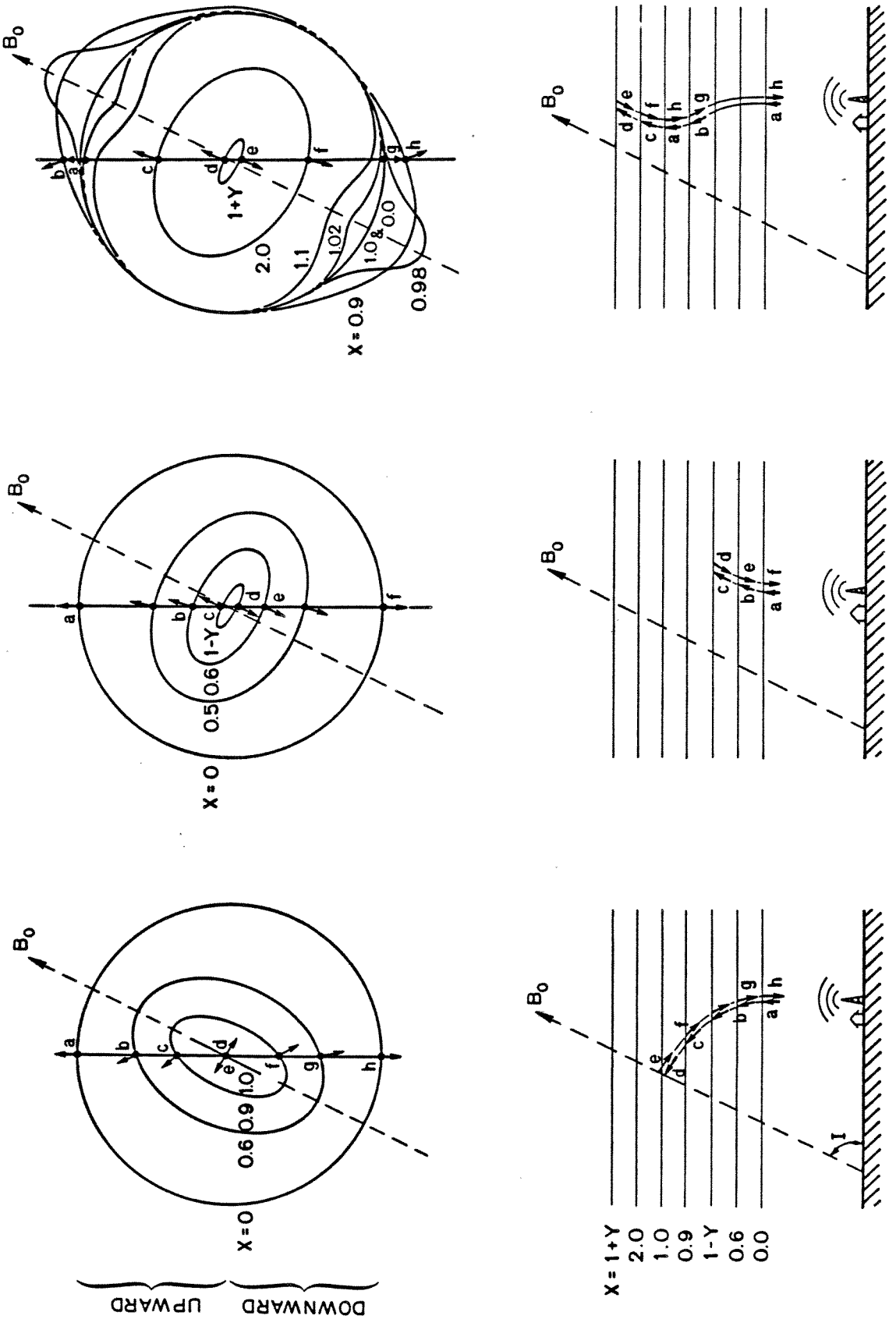

Figure 5.5 Refractive index surfaces and ray paths for a) ordinary mode, and extraordinary mode when b) Y<1 and c) Y>1

cases where $Y<1$ and $Y>1$, respectively. The refractive index surfaces at successive heights are drawn as concentric ellipsoids with major axes aligned with the magnetic field in the case of the ordinary mode and perpendicular to the field direction for the extraordinary mode. The isotropic propagation below the ionosphere, for which $X=0$, is represented by a spherical surface of unit radius. At greater altitudes X increases, causing the refractive index, and thus the dimension of the ellipsoid, to vary until finally $n=0$ at the top of the path for all but pure longitudinal propagation of the ordinary mode. The ray direction is always normal to the refractive index surface. At the reflection point, the ray direction for the ordinary wave is perpendicular to the magnetic field while for the extraordinary wave it is nearly parallel to the field direction when $Y\cong 0$ or $Y>>1$.

Traces of the ray directions as the waves penetrate to the reflection points are constructed in the lower panels of figure 5.5. The levels of constant X are drawn to show relative order and no height scale should be inferred from the figure. Because the waves are vertically incident, they will retrace their paths after reflection and exit the ionosphere at the points where they entered. The ordinary wave reflection point is always displaced away from the magnetic equator. The extraordinary wave reflection point is displaced towards the equator in the case where $f>f_H$ ($Y<1$). When $f<f_H$ ($Y>1$), the extraordinary wave can propagate in the whistler mode and the ray direction is deviated away from the equator until the wave has penetrated to a height where $f=f_H$ ($X=1$). Since the reflection point for the $f<f_H$ ($Y>1$) case is at a height where $X=1+Y$, the wave propagates beyond the $X=1$ height into a

region where the extraordinary mode refractive index is less than one and the ray is then deviated towards the equator.

The amount of horizontal displacement of the reflection point will depend on the height at which the index of refraction goes to zero. Lower frequency waves will be displaced less since they do not penetrate far into the ionosphere. At middle or higher latitudes the magnetic dip angle is large and vertical incidence approaches the direction of the geomagnetic field. The normals to successive refractive index surfaces then all have orientations close to the field direction and the net displacement of the reflection point is small.

It is common practice to neglect the horizontal displacement of the reflection point when considering middle and high latitude soundings. The group path can then be used to approximate an equivalent free space height of reflection, usually referred to as the virtual height, given by

$$h' = P'/2 \tag{5.4}$$

The virtual height at a given frequency can be determined through integration of equation (5.3) when the density (and therefore the refractive index) profile is known.

E. Ionogram Changes due to Precipitation

An ionogram is a plot of virtual heights corresponding to a range of wave frequencies. HF waves up to a critical frequency will be reflected from the ionosphere. The critical frequency is determined by

the condition for reflection for a wave penetrating to the height of maximum electron density. At frequencies above the critical frequency, waves will be retarded, but not reflected by the medium.

A simulated ionogram can be obtained from a model density profile such as any of those presented in the examples of chapter 4. The procedure begins by determining a height profile of the refractive index for a given wave frequency by applying equation (5.1) to the model density profile. A second frequency is then chosen very close to the first (typically within 1 percent) and a similiar height profile is obtained for the refractive index at that frequency. From the two profiles, a third profile is calculated which expresses the variation with height of the frequency derivative of the refractive index. Therefore at height h_j,

$$\left.\frac{\Delta n}{\Delta f}\right|_{h_j} = \frac{n(f)_j - n(f + \Delta f)_j}{\Delta f}$$

where Δf is the frequency offset between the two waves. The refractive index and its frequency derivative are each integrated over the path from the bottom of the ionosphere to the reflection height. The virtual heights at the given frequency for the ordinary and extraordinary modes are then calculated as indicated in equation (5.3). A repetition of the procedure for a sweep of frequencies up to the critical frequency then provides data which can be plotted in the usual form of virtual heights as a function of frequency. The resulting ionogram will show characteristics which depend on the density profile.

The model ionogram shown in figure 5.6a is typical of the nighttime

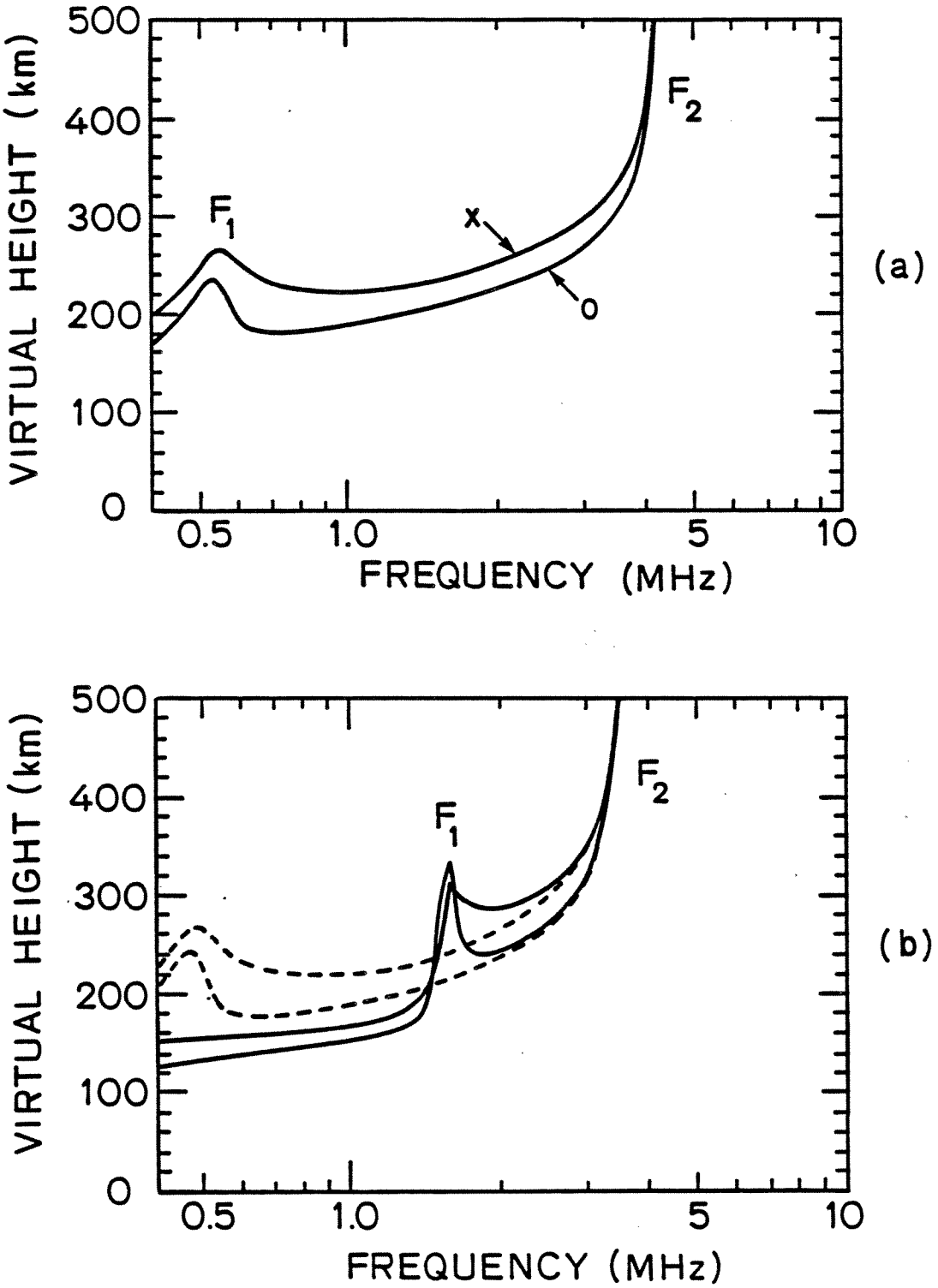

Figure 5.6 Model nighttime ionograms at a) 2230 LMT before and b) 2330 LMT after one hour of precipitation

mid-latitude ionosphere in the absence of electron precipitation and is calculated using the density profile at 2230 local time (t=0) from figure 4.6a. Both the ordinary and extraordinary traces are shown. The critical frequency for the ordinary mode ($f_o F_2$) is slightly less than for the extraordinary mode ($f_x F_2$). A noticeable feature of the ionogram is a virtual height maximum at about 500 kHz due to the contour of the density profile (see figure 4.6a) at a true height of about 160 km. This slowly decaying remnant of the daytime F_1 layer persists throughout the night. The sharpness of a virtual height maximum depends on the gradient of the density with height. If a layer of ionization is present in the profile such that the density decreases above and below the layer maximum, then the gradient will be zero at the height of the maximum density and a cusp will appear in the ionogram at a frequency which penetrates to the layer maximum.

A continuous precipitation of 1 keV electrons with an energy flux of 0.01 erg cm^{-2} s^{-1} is then allowed to enhance the density profile for one hour (t=60) as shown in figure 4.6a. The resulting ionogram appearing in figure 5.6b shows that the virtual height maximum associated with the F_1 region has moved to a much higher frequency. This is a direct indication of the increase in density in that region. The development of the virtual height maximum into a sharp cusp shows that a definite layer has formed. A quantitative determination of the density at the F_1 region maximum can be made by applying equation (5.2) to the cusp frequency.

F. VLF Transmissions to Induce Ionogram Changes

The characteristic changes seen in figure 5.6 result from a continuous precipitation of 1 keV electrons with an energy flux of 0.01 erg cm^{-2} s^{-1}. Such fluxes are expected to be precipitated by 5 kHz waves of intensities of less than 10 pT at L=4 (Inan et al., 1978). A controlled source of VLF waves at that latitude is the transmitter at Siple Station (Helliwell and Katsufrakis, 1974). A few satellite measurements of the transmitter signals in the magnetosphere (Inan et al., 1977) have shown typical intensities of about 0.3 pT before amplification through cyclotron resonant interactions. Wave growth of 30 dB is common for VLF signals propagating though the magnetosphere (Stiles and Helliwell, 1977). Assuming this much growth for a 0.3 pT input, then wave intensities of up to 10 pT can be expected for the Siple transmitter signals in the equatorial region.

In order for an ionospheric layer to be formed by energetic electron precipitation, the time averaged ion production must exceed the losses due to recombination, diffusion and transport. If the precipitation occurs as bursts, then the ionosphere begins to recover between successive events and the time required to cause a detectable change in an ionogram will be increased. For the quickest build up, therefore, a continuous precipitation of the maximum possible flux density is required. To achieve this, the VLF transmitter should be operated at the greatest practical power with a 100 percent duty cycle.

The frequency of the transmitted signal should be chosen to optimize the likelihood of scattering energetic electrons into the loss

cone. A proposed format would cover a limited bandwidth of about 500 Hz centered on a frequency determined by the operator to be the most responsive to the transmitter. Since amplification of the signal by the magnetosphere is essential for wave intensities great enough to cause measurable precipitation effects, the decision as to which frequency is most responsive should be based on real-time observations of exploratory signals at the conjugate point or of the two hop echos at the transmitter site.

The growth of coherent VLF transmitter signals in the magnetosphere can be suppressed by echces of signals transmitted earlier at the same frequency (Raghuram et al., 1977). The echoes are believed to reduce the coherence of the total signal present in the growth region. The echo-induced suppression can be as much as 20 dB and should be avoided by varying the frequency at a rate which insures that the echo is always well separated in frequency from later signals arriving at the same time in the growth region. This criterion is well satisfied by a frequency ramp with a slope of 100 Hz/sec. While both ascending and descending ramps can avoid echo-induced suppression, ascending ramps have the disadvantage that the higher frequency portions of the ramp can be suppressed by rising emissions which are triggered by echoes of the lower frequencies portions of the ramp. For this reason, the proposed VLF transmitter format employs a continuous succession of 5 second long descending frequency ramps at a slope of 100 Hz/sec in a 500 Hz band about the most responsive frequency. At intervals of 15 minutes, exploratory ramps of the same slope should be transmitted over a wider range of frequencies so that the operating frequency band can be

evaluated. The exploratory ramps should be transmitted in segments, followed by a brief key up period during which the operator has an opportunity to examine the VLF spectrum for transmitter echoes.

During the VLF transmitter operation the ionosonde should generate ionograms with a high resolution in frequency so that small changes in the density profile can be detected. Of particular interest will be the formation of cusps in the ionogram as well as frequency changes of cusps already formed at an existing layer maximum. Since the build up of ionization due to precipitation is a relatively slow process with an effective time constant on the order of tens of minutes (figure 4.9), an ionogram sampling rate of one in every five minutes should be adequate for identifying the predicted effect.

Chapter VI

EFFECT OF WAVE-INDUCED PRECIPITATION ON KINESONDE PHASE

A. Introduction

A pulsed HF radar system can be used to measure the phase path at a single frequency. This operating mode is simpler than the sweep frequency mode because the transmitter and receiver tuning are fixed. The RF phase is sometimes obtained by counting cycles of a high frequency (e.g. 4 MHz) local reference oscillator between the start of the transmitted pulse and the first zero crossing of the IF receiver output. In more elaborate systems such as the kinesonde (Paul et al., 1974), multiple antennas and frequencies permit a determination of the direction of arrival for the echoes.

A digital HF radar was operated at Roberval, Quebec from July 1980 until July 1981. A survey of the variability of the phase of fixed frequency kinesonde signals suggests that while the phase can be rapidly varying at times, often the phase changes are quite slow. Figure 6.1 shows three typical phase variations at Roberval. While the figure shows only advancing phase, the data contain an equal proportion of records in which the phase is retarded. The various sources of the background phase variations are considered in section C of this chapter. The phase changes through 360 degrees at various rates, yet successive cycles show the same sense of rotation. This indicates that the total phase change has an amplitude of many cycles. The typical background phase change oscillates between retarding and advancing with a period of

several minutes.

Under certain conditions the echoes reflected from the F region are widely spread in measured delay time. This is known as spread F and is a nighttime phenomenon which can occur at any latitude. It is generally believed to be caused by scattering of the sounder signals from ionospheric irregularities, both in the vertical and horizontal directions. In middle latitudes it is seen most often after midnight during times of increased magnetic activity (Davies, 1965). The frequency of occurrence increases with sunspot number (Pierce, 1957) and is greatest in the local winter at middle latitudes. In figure 6.2a, a sample ionogram shows spread F observed at Roberval just prior to sunrise in December. A subsequent phase sounding at a fixed frequency of 1.8 MHz shows a general lack of coherency, illustrated in the phase plot of figure 6.2b. The spread F events represent a departure from the usual slowly varying kinesonde phase changes. The search for phase perturbations associated with wave-induced precipitation should obviously avoid intervals of spread F occurrence.

If wave-induced precipitation can be detected as a perturbation in the phase of a fixed frequency sounder signal, then it may be possible to modulate the observed effect by using a VLF transmitter as a source of waves to drive the magnetospheric loss cone scattering. In an analogous situation, another controlled source of ionospheric disturbance has been seen to perturb the phase of HF radar echoes at the Arecibo observatory during June and July, 1981 (L.M. Duncan, private communications). An ionospheric heating experiment was conducted using the Arecibo 1000 foot diameter reflector to transmit CW radio waves at a

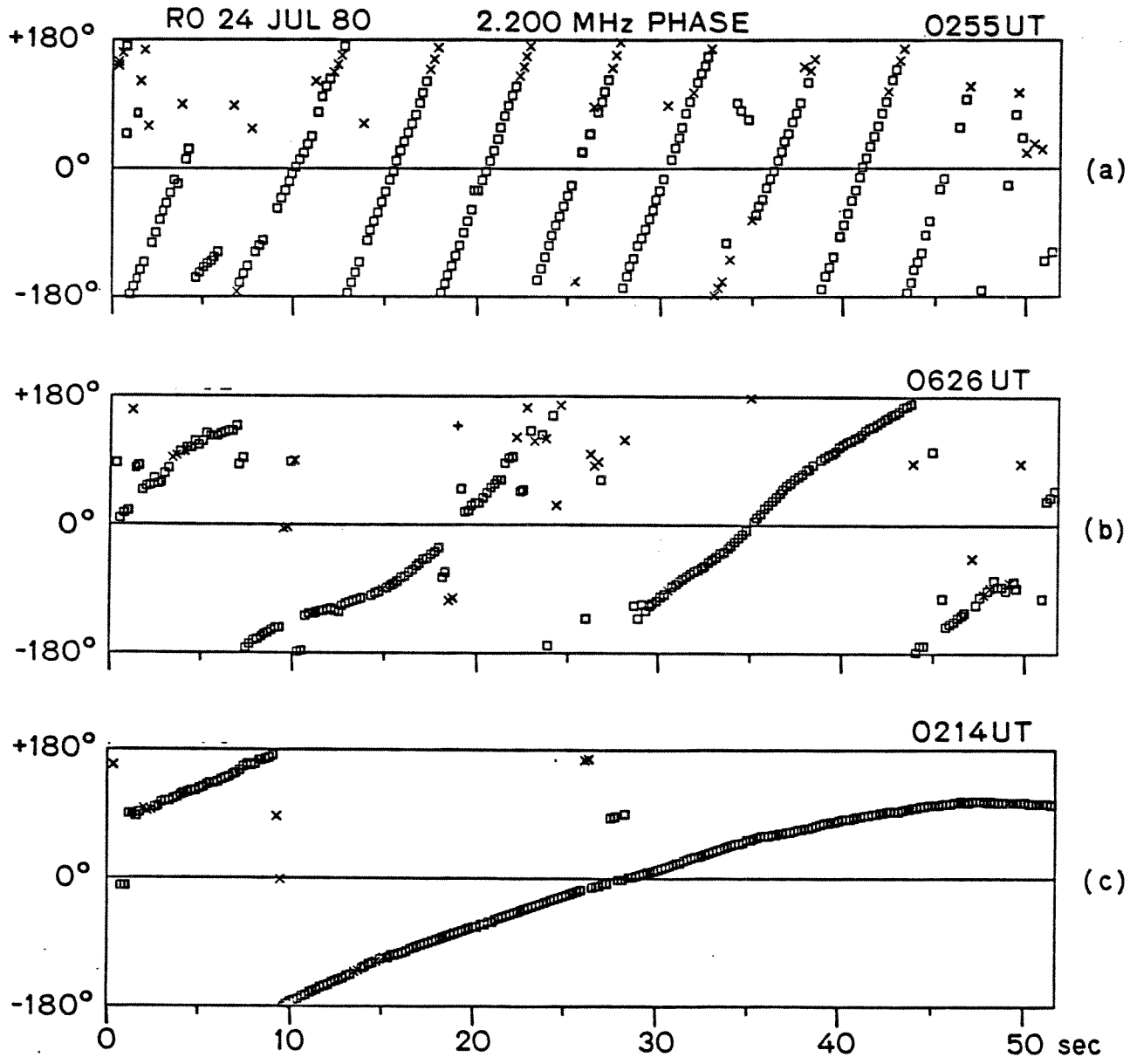

Figure 6.1 Background phase variations at Roberval

frequency of 5.1 MHz. The nominal transmitter power was 300 to 400 kW and the antenna gain was 25 dB. The transmitter was keyed using a 50 percent duty cycle with "on" times of 10, 60 and 120 seconds. The HF radar was operated at several fixed frequencies including 3.31, 4.30, 6.01 and 6.81 MHz. The initial results obtained on several occassions between about 1400 and 1600 local time showed distinct perturbations of the phase of the HF radar echoes at each frequency synchronized with the heating pulses.

B. Phase Path

In chapter 5 the measured group delay time was used to find the virtual reflection height. The group path was defined as the equivalent distance a wave packet would have traveled in free space during the measured time between transmission and reception of the pulse. The phase path has a similar definition. It is the distance that a surface of constant phase would transit in free space during the same time interval. Since the phase and group velocities are in general not the same, the phase and group paths will also tend to be different.

The phase delay time can be expressed in terms of the integral over the path of the phase velocity (v_p), such that

$$t = \int_{path} \frac{ds}{v_p}$$

The corresponding phase path is

$$P = c\ t = c \int_{path} \frac{ds}{v_p}$$

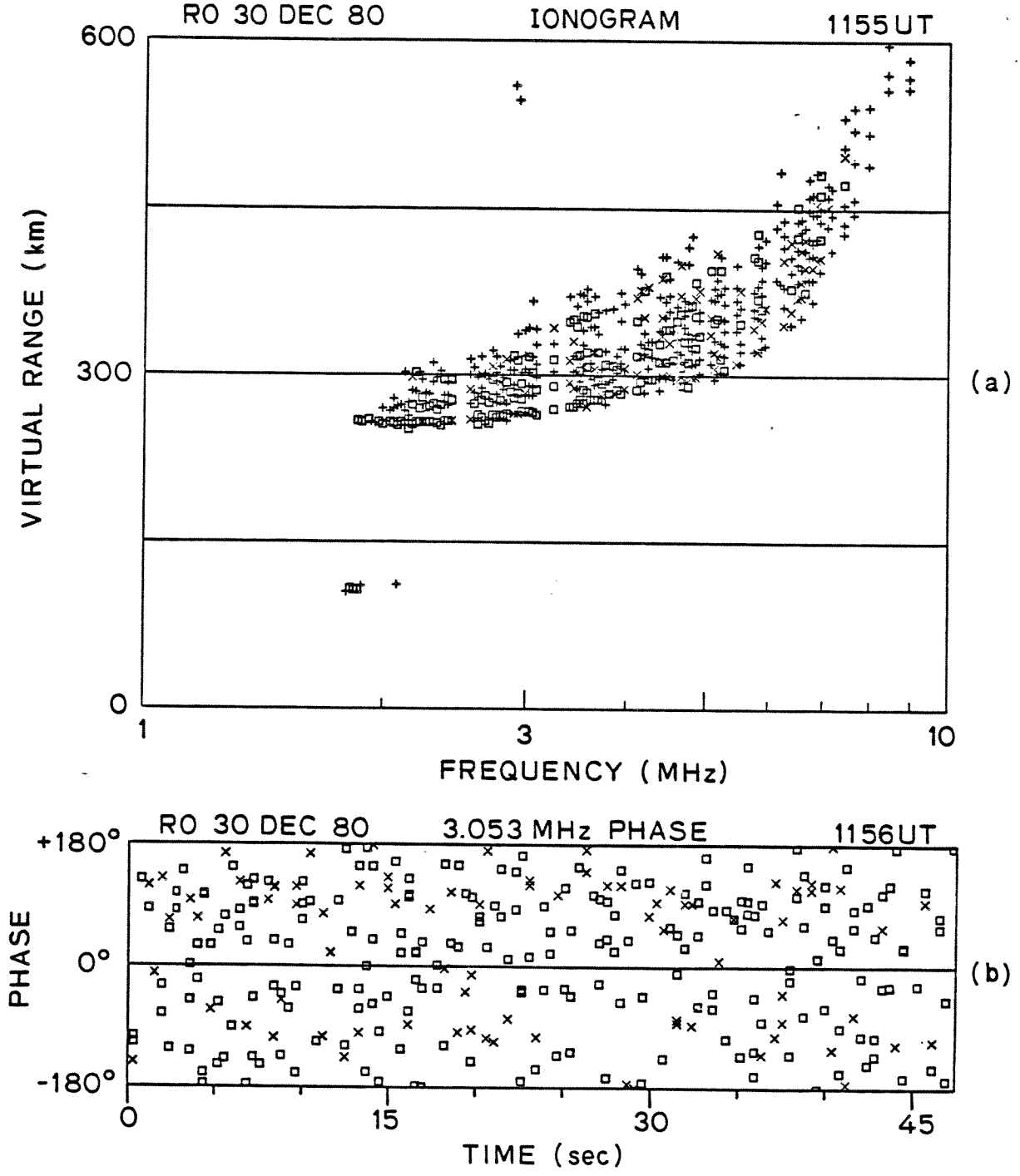

Figure 6.2 Spread F and associated phase variations

Now since $n=c/v_p$,

$$P = \int_{path} n \, ds \qquad (6.1)$$

At the top of the path for a vertical incidence wave the refractive index goes to zero and the phase path integral converges. The computation can therefore be made more easily than in the case of the group path integral (equation 5.3). The refractive index as a function of height can be found for each mode by solving equation (5.1) when a density profile is known. In section D, density profiles presented in chapter 4 will be used to calculate the temporal change in the phase path during precipitation events.

The phase height of a wave of a given frequency (f) is defined as one half of the total phase path.

$$h^* = P/2$$

The definition is analogous to the relation between the group height and the total group path in that it also assumes that the deviation of the ray path from the vertical is negligible. The total phase delay is given by

$$\phi = \frac{2\pi f}{c} P = \frac{4\pi f}{c} h^* \qquad (6.2)$$

Changes in the phase of an ordinary mode signal caused by density changes along the path will be in the opposite sense from the density

changes. This is a result of the density dependence of the refractive index. From figure 5.3 it can be seen that as the density increases (increasing X) the refractive index at a given frequency will decrease. The phase path integral (equation 6.1), and thus the phase, will therefore decrease with an increase in density. The phase of an extraordinary mode signal will also change in the opposite sense from the density change when Y<1. For Y>1, figure 5.3b shows that the extraordinary mode refractive index will first increase and then decrease with increasing density. The sense of the total phase change in that case will depend on the value of Y.

C. Phase Fluctuations

HF signals reflected by the ionosphere show phase changes which have time periods ranging from several seconds to several hours. Phase height variations of solar-cycle or seasonal scale also exist (Wright, 1974), however these will be of such a long period as not to be noticeable in most kinesonde data. It is against this noisy background that we will look for phase changes induced by precipitation. It is useful, therefore, to consider the magnitude, period and frequency of occurrence of typical phase disturbances. These parameters are summarized from the following discussion in Table 6.1.

Phase height fluctuations can be caused by vertical motions of the entire reflecting layer or by changes of the layer thickness. Vertical displacements of a layer will be associated with acoustic gravity waves and motions of the plasma due to neutral winds, while changes in the layer thickness will result from density changes. The most significant

changes in the ionospheric density profile occur in association with the diurnal cycle. As the ionosphere relaxes after sunset, the reflection height for an HF signal of a given frequency will slowly increase.

During about 50 percent of winter nights at mid-latitudes in either hemisphere, large scale vertical convection is observed between about midnight and 0600 local time (Wright, 1971). The downward motion is believed to be driven by neutral winds in the F region rather than by electrostatic fields. Such events often are characterized by the F region density profile lowering by as much as 150 km. At the lower altitudes recombination proceeds more rapidly and much of the ionization is lost. Such profile lowering of the F region often causes a pre-sunrise increase in the E region density.

Traveling ionospheric disturbances (TID) is a term first used by Munro (1958) to describe undulations which propagate horizontally in the F region at about 500 km/hr. They are observed nearly every day and usually occur as a single wave with a period in the range of 4 minutes to 1 hour. The vertical amplitude of the phase height motion in the F region can be as much as 20 km (Davies and Jones, 1971).

Ionospheric pressure waves of shorter period (typically 5 to 15 minutes) are almost always present. Sometimes referred to as ripples, the waves have phase height amplitudes of about 2 km during times of magnetic quiet, but can be as large as 16 km during magnetic storms (Davies and Baker, 1968). Ripples are believed to be responsible for scintillations in the amplitude and phase of radio wave echoes. The effect has been considered statistically by Booker et al. (1950) as one of diffraction from an irregular screen.

Table 6.1

SOURCES OF KINESONDE PHASE HEIGHT VARIATIONS IN THE F-REGION

DISTURBANCE	PERIOD	AMPLITUDE	OCCURRENCE	REFERENCE
Large vertical layer motions at mid-latitudes	6 hrs	150 km	50% of winter nights 00-06 LMT	Wright (1971)
Earthquake induced acoustic gravity waves	0.5-90 min	60 km	rare	Row (1966) Alaskan quake 28 MAR 64
Solar flare X-ray and UV ionization enhancements	0.5-15 min	45 km	150 per year (day only)	Agy, Baker, and Jones (1965)
Traveling Ionospheric Disturbance (TID's)	4-60 min	20 km	daily	Davies and Jones (1971)
Ionospheric pressure waves (ripples)	5-15 min 5-15 min	2 km 16 km	magnetic quiet magnetic storms	Davies and Baker (1966)
Nuclear exposion induced acoustic gravity waves	0.5-10 min	3.0 km	rare	Baker and Davies (1968)
Sudden commencements of magnetic storms	0.5-2 min	3 km	several times per month	Chan, Kanellakos, and Villard (1962)
Periodic fluctuations with micropulsations	1 min	1.5 km	once every 4 months	Davies and Baker (1966)
Electron precipitation induced by VLF waves	1-15 sec	3 km	20-90 minute intervals several times per year	present report

Occasionally, geomagetic micropulsations are observed in correlation with periodic fluctuations in the phase height of HF signals (Jacobs and Watanabe, 1964). The typical reflection height changes have peak-to-peak amplitudes of about 1.5 km and periods of the order of one minute. These events occur at mid-latitude sites on an average of only about three times per year and the cause is not understood (Davies and Baker, 1966).

Large phase height perturbations can be caused by sudden increases in ionization due to x-ray and EUV radiation emitted during solar flares. Called "sudden frequency deviations" (SFD) by Chan and Villard (1963), the increase in ionization causes the phase of a radio wave propagating through the enhanced ionosphere to be perturbed on a time scale of less than 15 minutes. The most frequently observed duration is about 4 minutes (Agy, Baker and Jones, 1965). A common technique for observing SFD's is to monitor the frequency of a transmitter such as WWV for sudden changes. If a short baseline exists between the transmitter and receiver, then vertical incidence can be assumed. An equivalent phase height variation can then be calculated by interpreting the observed sudden frequency deviation as resulting from a doppler shift due to the vertical motion of a supposed reflector at the top of a free space path (e.g. Row, 1966; Davies and Baker, 1966). For a stationary transmitter and receiver, the instantaneous velocity of a moving reflector can be expressed by the doppler formula as

$$v_r = c \frac{f_R - f_T}{f_R + f_T}$$

where f_T and f_R are the transmitted and received frequencies, respectively, and the wave is assumed to propagate at the speed of light. By measuring the temporal change in received frequency, we obtain the time varying velocity of the supposed reflector. The maximum vertical displacement is found by integrating the doppler velocity over the interval for which the frequency changes in one sense. An increase in frequency (i.e. "blue shift") indicates that the supposed reflector has moved downward. While sudden frequency deviations occur as often as 150 times per year (Agy, Baker and Jones, 1965), they happen only during the day since the phenomenon is caused by bursts of solar radiation.

Most SFD's show frequency changes of only a few Hertz at 10 MHz, but one large event reported by Davies and Baker (1966) resulted in a change in frequency of 50 Hz for WWV at 10 MHz in a 60 second interval. Assuming that the frequency changed at a constant rate, then the average velocity of the supposed reflector was 0.75 km/sec and the total phase height displacement was about 45 km.

Magnetic sudden commencements also cause perturbations to the phase and frequency of radio waves propagating in the ionosphere. The frequency variation of a typical event is characterized by a sudden change during the initial 30 to 120 seconds, followed by a ringing which lasts for about 10 minutes (Chan, Kanellakos and Villard, 1962). A magnetic sudden commencement event reported by Davies and Baker (1966) showed a 7 Hz frequency change of WWV at 10 MHz during the initial 30 seconds. Interpreting this as a doppler shift due to the motion of a supposed reflector at the top of a free space path, we obtain an effective phase height change of about 3 km. Sudden commencement events

occur at a rate of several per month.

The various sources of phase height variations are summarized in table 6.1 in order of decreasing amplitude. Also included is a very large amplitude effect which can result from acoustic gravity waves generated by earthquakes. An observation of a vertical incidence 4 MHz signal at Boulder, Colorado (Row, 1966) showed a 1.2 Hz doppler shift in about 22 minutes associated with the Alaskan earthquake of March 28, 1964. The equivalent phase height change was calculated to be 57 km by integrating the actual phase change. While earthquakes are large scale events, they are also quite rare.

Another type of acoustic gravity wave event included for comparison results from the low altitude atmospheric detonation of nuclear weapons. Fortunately such events are banned by international agreement, yet it is interesting to note that early observations (Baker and Davies, 1968) showed phase height changes of as much as 3 km at a distance of over 7000 km from the blast.

D. Precipitation Induced Phase Changes

In chapter 5 we have seen that long enduring precipitation of 1 keV electrons with an energy flux of 0.01 erg cm^{-2} s^{-1} can cause changes in the density profile large enough to be detectable through examination of a sequence of ionograms. However, experimental evidence of electron precipitation induced by discrete VLF waves (e.g. Rosenberg et al., 1971; Foster and Rosenberg 1976; Helliwell et al., 1980) has shown that the events are usually of short duration, typically less than 15 seconds. While the energy flux during a single event has been inferred

to be as much as 0.1 erg cm^{-2} s^{-1} (Helliwell et al., 1980), the total energy deposited during a short burst of precipitation would only result in a very small change in the character of an ionogram. The time required to sweep through the range of ionosonde frequencies of interest with the necessary resolution to detect such changes is about 20 seconds for a typical ionosonde. As a result, the data may lack sufficient time resolution to identify the transient events.

For transient events, a more responsive technique of observation is to monitor phase changes of fixed frequency transmitter signals. At night the ionospheric densities are much less than during the day and therefore the enhancements due to precipitation represent a proportionally larger change. Thus the nighttime phase perturbations will be larger than those occurring during the day. During the daytime the kinesonde phase is generally more stable than at night. It is not obvious whether a greater signal to noise ratio would exist during the day or night. In this report we shall consider only the nighttime case. Further study could address the comparison between day and night signal to noise ratios.

The choice of frequencies to monitor for phase perturbations depends on the expected energy spectrum of the precipitated electrons. For a relatively hard spectrum, the height of maximum ionization will be in the D or E region while for a softer spectrum it will be in the F region. If the frequency transmitted is too low, the wave will be reflected below the region enhanced by corpuscular ionization and no perturbation in phase will be seen. If a frequency close to the critical frequency (f_0F_2) is chosen, then the wave will penetrate

through the enhanced region and be reflected from the F_2 region. An increase in density at any height below the reflection level will increase the local phase velocity and therefore decrease the total phase path. However the magnitude of the phase path change will depend on the change in the refractive index profile, which in turn depends on the wave frequency. For a given density profile enhancement, the refractive index profile is changed more for lower frequencies, thus a phase path sounder should be operated at the lowest frequency which penetrates the enhanced region. For 1 keV electrons, the ionization enhancement occurs below about 200 km, as shown in figure 4.6a. The initial density at 2230 local time at that height is $3 \times 10^{-4} cm^{-3}$. The wave frequency for reflection at that height is found from equation (5.2a) to be 1.5 MHz.

In order to examine the phase perturbation of a fixed frequency signal during precipitation, transient events were simulated using the model ionosphere program described in chapter 4. The density profile was calculated at coarse steps of time (every 15 minutes) beginning in the mid-afternoon (1500) and proceeding to 2229:50 local time. The time step was then reduced to 0.1 second so that the changes in the density profile would be small between successive steps. At 2230:00 local time the nighttime profile is represented by the "t=0" curve in figure 4.6a. A precipitation flux of 1 keV electrons with an energy density of 0.01 erg cm^{-2} s^{-1} is then turned on and the density begins to increase, particularly in the region near the height of maximum ionization (i.e. about 170 km for 1 kev electrons). The buildup of ionization is exponential as can be seen from figure 4.8.

In figure 6.3 the phase of a 1.5 MHz ordinary mode kinesonde signal

is shown as a function of time for cases where the 0.01 erg cm^{-2} s^{-1} precipitation flux persists for 1, 5 and 15 seconds. Prior to the beginning of precipitation, the nighttime ionosphere is slowly decaying and thus, as we have discussed, a decrease in electron density results in an increase in the phase of a fixed frequency signal. The diurnal phase advance for a 1.5 MHz signal at 2230 local time is about 90 degrees per minute. During the precipitation event the phase suddenly becomes retarded as the density along the phase path increases.

When the precipitation is abruptly terminated, the instantaneous change in density goes from increasing due to corpuscular ionization to decreasing due mainly to recombination. The kinesonde phase therefore abruptly changes from retarding to advancing. The rate of phase advance following the density enhancement event will be slightly greater than the diurnal rate since, as can be seen in figure 4.11, the recovery time constant is density dependent.

Figure 6.3 shows that the total phase change will depend on the duration of the precipitation. The rate of phase change is greatest during the initial stage of the event and decreases with time as the ionization tends towards saturation. The precipitation pulses of 1, 5 and 15 second durations cause the phase of a 1.5 MHz signal to change by about 2.9, 12.3 and 26.4 cycles respectively. Using equation (6.2) we find that this corresponds to phase height changes (Δh^*) of about 0.3, 1.2 and 2.6 km, respectively, where

$$\Delta h^* = \frac{\Delta \phi c}{4\pi f}$$

While these phase height changes are small compared to the changes associated with large vertical layer motions or traveling ionospheric disturbances, they are of much shorter duration and therefore the slowly varying background can be filtered out. Most of the higher frequency components of the background phase height variations listed in table 6.1 occur as transient events correlated with other observable phenomena such as solar flares or sudden commencements of magnetic storms. Since VLF wave induced precipitation events can be expected to occur as a repeatable phenomenon during an interval of some tens of minutes, it should not be difficult to distinguish them from single transient events. Periodic fluctuations correlated with magnetic micropulsations occur infrequently and can be identified through simultaneous observations of the magnetic field strength.

The dominant component of the background phase height variation with a period of less than 15 minutes is due to ionospheric pressure waves. During magnetic storms these "ripples" can be of quite large amplitude, but are less (about 2 km) during magnetic quite conditions. The limiting time rate of change of the phase height for ripples during magnetic quiet conditions can be found by assuming that the undulations have an amplitude of 2 km and a period of 300 seconds, and therefore can be represented as

$$h^* = \bar{h} + 2 \sin(\pi t/150)$$

where $\bar{h}$ is the average phase height. The derivative of this expression,

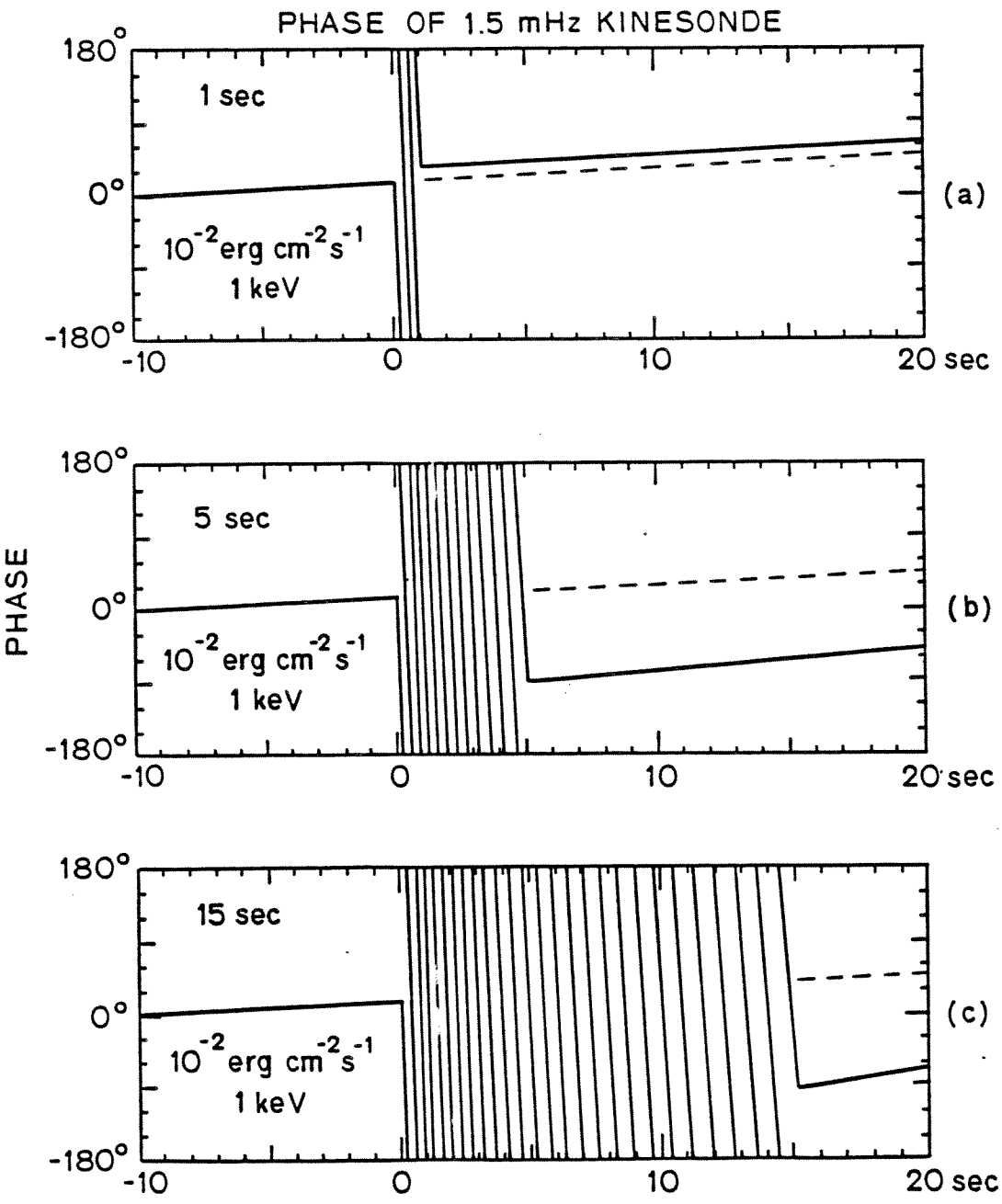

Figure 6.3 Simulated phase changes due to 0.01 erg cm^{-2} s^{-1} flux of 1 keV electron precipitation for a) 1 sec b) 5 sec and c) 15 sec

given by

$$dh^*/dt=\pi/75 \cos(\pi t/150)$$

gives the instantaneous time rate of change of the phase height. The greatest rates of change can be found by evaluating the derivative at t=0 and t=150. Thus we obtain $dh^*/dt=\pm 42$ m/sec for the limiting phase height changes associated with ionospheric pressure waves. At 1.5 MHz this would result in a maximum rate of change in phase of about 150 degrees per second. Such rapid phase changes are sometimes seen in the kinesonde data at Roberval, Quebec; however the usual background varies more slowly.

A perturbation to the rate of phase change will go unnoticed in a plot such as figure 6.1 unless there is a substantial change of slope. It is useful to define a smallest detectable negative change of slope of 45 degrees per second as being the least which we will consider likely to attract our attention, even in the presence of simultaneous VLF wave data which would point to particular times. The model results shown in figure 6.3 for a 0.01 erg cm^{-2} s^{-1} flux of 1 keV electrons predict a change in phase with a negative slope of about 1000 degrees per second for the perturbed phase of a 1.5 MHz signal. This far exceeds the assumed negative change of slope threshold and thus we would expect to detect this event against a background of ionospheric pressure waves.

Figure 6.4 shows the effect of reducing the precipitation flux of the 1 keV electrons. A factor of ten reduction to 0.001 erg cm^{-2} s^{-1} causes the phase to change by only 165 degrees in 5 seconds. The

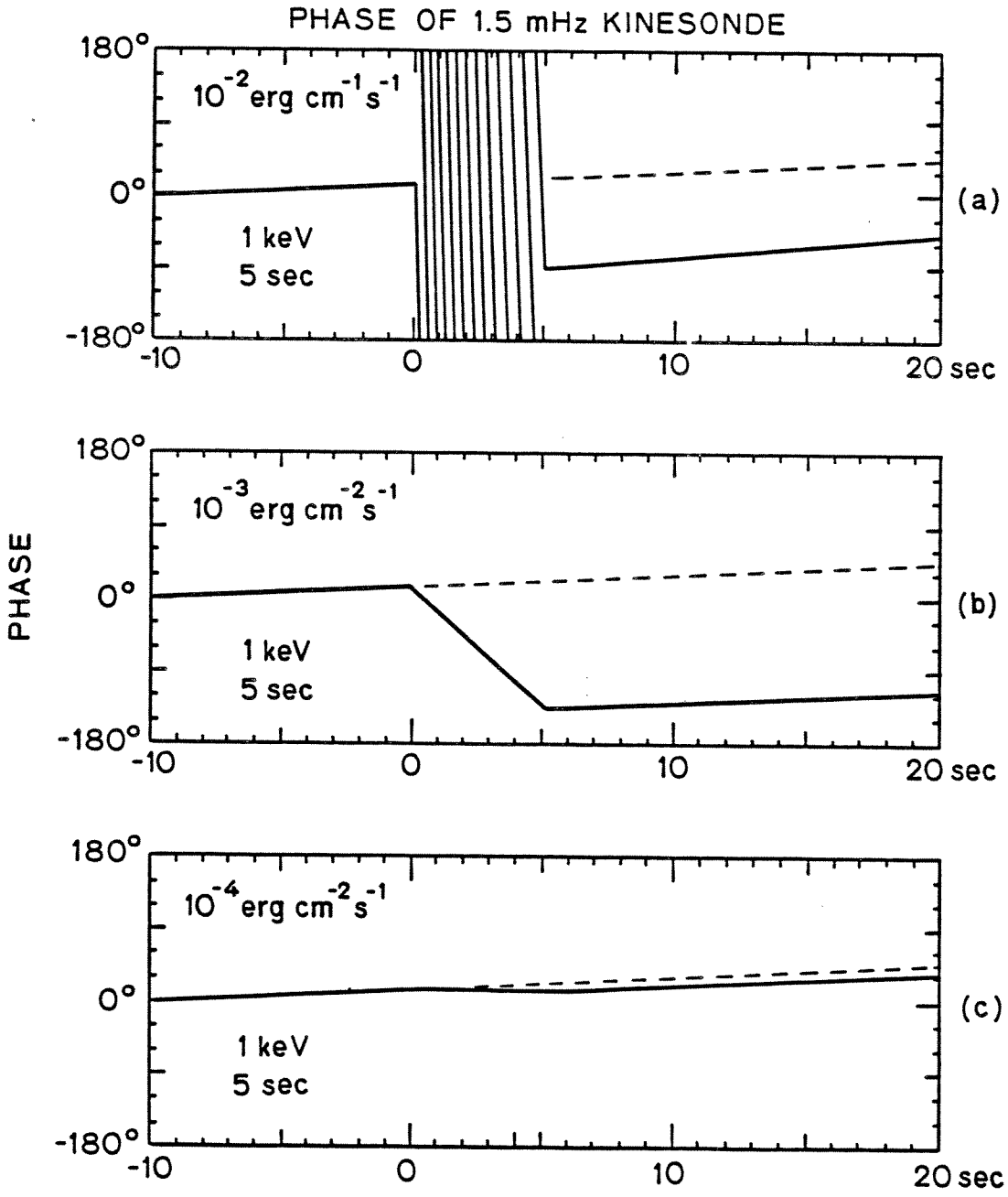

Figure 6.4 Simulated phase changes due to 5 second precipitation of 1 keV electrons for a) 0.01 b) 0.001 and c)0.0001 erg cm^{-2} s^{-1} energy fluxes

average rate of change in phase is therefore less than the assumed minimum for detection. A further factor of ten reduction of the flux shows in figure 6.4c that the phase perturbation (3 degrees/second) is negligible.

These results show that a minimum energy flux of a few times 10^{-3} erg cm^{-2} s^{-1} is necessary for direct detection of 1 keV electron precipitation using the kinesonde phase monitoring technique. For lesser energy fluxes, the sensitivity could be increased by integrating many events. For detection of small phase changes associated with precipitation induced by the VLF transmitter at Siple station, an appropriate method of integration is epoch superpositioning in which the transmitter key-on time is used to synchronize the integration of successive intervals. Assuming a constant delay between the injection of VLF waves and the arrival of precipitating electrons, then the kinesonde phase perturbations due to precipitation will add coherently while the random background phase will add as incoherent noise.

Compared to the rates of phase change on the order of several hundred degrees per second predicted in figure 6.3 for 0.01 erg cm^{-2} s^{-1} precipitation of 1 keV electrons, the phase fluctuations for ripples are slowly varying and can be filtered out. A technique of digital filtering which could be applied to the phase data would be to first smooth the data using a moving average. The result would in effect be low pass filtered and should be characterized by the phase fluctuations of the background. A high pass filtering of the original phase data can be achieved by subtracting the low passed results.

E. VLF Transmissions to Induce Changes in Kinesonde Phase

In chapter 5 it was suggested that a VLF transmitter such as that operated at Siple station could be used to stimulate electron precipitation which might result in a modification of the density profile. While the sweep frequency ionosonde was considered as an instrument for detecting long enduring events, photometers and x-ray detectors show evidence that short events occur. The kinesonde phase measurement technique is well suited to the detection of such events.

The transmitter format described in chapter 5 was proposed to induce a continuous precipitation flux of energetic electrons. The intention there was to form an ionospheric layer in which the processes of production and loss would approach a steady state. The rate of build up of ionization caused by 1 keV precipitation was found to be dependent on the energy flux, as is shown in figure 4.9. The instantaneous rate of decay of ionization when the source of precipitation is removed depends on the density at a given time, as shown in figure 4.11. The greatest rate of change in the density profile, and therefore in the phase of a fixed frequency sounder signal, will occur when the initial density is well below the saturation level. A transmitter which might control the precipitation flux should therefore be keyed with a duty cycle which ensures that the ionosphere has ample time to recover after each pulse of corpuscular ionization.

The time required for ionization to build up to a given density at a height of 170 km can be calculated as a function of the duty cycle of the precipitation flux. For various duty cycles, equations which

describe the ionization buildup (4.15) and decay (4.16) can be used to find the time necessary for the ionization to increase by 1/e of the amount by which the saturation density exceeds the initial density. The initial density is assumed to be 4.8×10^3 cm^{-3} which is shown in figure 4.8 to correspond to 2230 local time. The results plotted in figure 6.5 show that a duty cycle of less than 50 percent will guarantee that layer saturation will be avoided for energy fluxes of up to 0.1 erg cm^{-2} s^{-1} of 1 keV electrons.

A proposed transmitter format designed to cause phase modulation of a fixed frequency sounder signal through controlled precipitation will use simple 500 Hz bandwidth descending ramps. A one minute transmission might consist of a five second ramp and two ten second ramps, each followed by a keyup period of equal duration to give a 50 percent duty cycle. The final 10 seconds of each minute would also call for the transmitter key to be up, providing additional time for the recovery from corpuscular ionization. The duration of the transmitted ramps is 10 seconds or less so that any resulting phase path changes will be detectable after the data has been high-pass filtered to remove the slow variations of the background phase.

A fixed frequency sounder should be synchronized to obtain continuous high time resolution phase path data both during key-down and key-up times of the VLF transmissions. Some digital HF radar systems require overhead time to write the acquired data to tape. This could be scheduled for the last 10 second recovery period of the 1 minute sequence. The experiment would be optimized by a field researcher who could adjust the frequency of the VLF transmitter to maximize the

observed wave growth and the frequency of the HF radar to probe to a reflection height just above the region where corpuscular ionization was suspected.

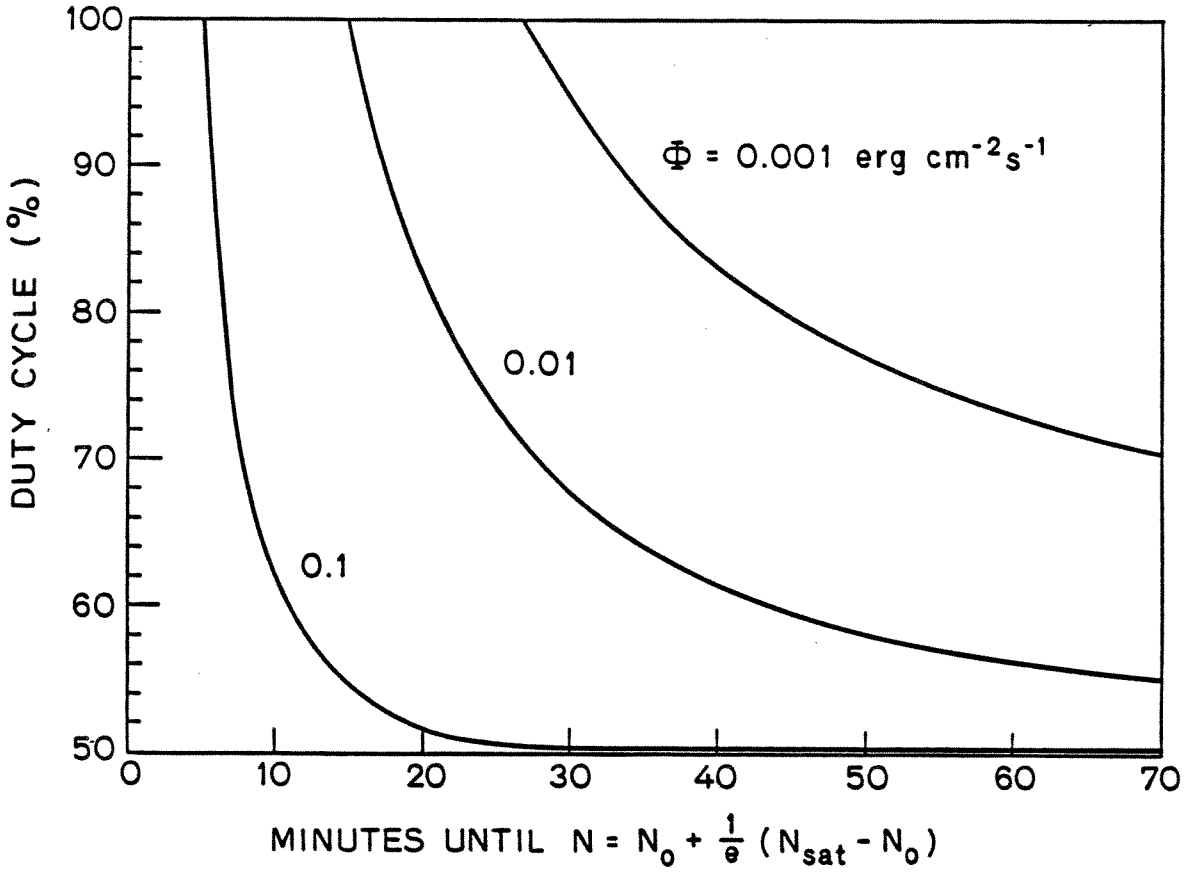

Figure 6.5 Time necessary to reach specific density as a function of duty cycle

Chapter VII

SUMMARY AND RECOMMENDATIONS

In this chapter we shall summarize the contributions of the present work and offer recommendations for further investigations. This report suggests possible field experiments which could be used to extend the detection of precipitation to lower energies. It also points to further ionospheric modeling exercises which could be done in order to predict the detectability of daytime precipitation using the technique of monitoring the phase of a fixed frequency HF signal.

A. Summary

A computational model is described in chapter 2 which provides a means of determining the shape of a pulse of wave-induced electron precipitation. For a wave of a given frequency, the resonance condition is satisfied by electrons of increasing energies at increasing latitudes. Thus in the model a whistler-mode wave is assumed to scatter electrons of various energies into the loss cone as it propagates along the field line. There is a tendency for the faster electrons which are scattered by the wave after it has passed the equator to catch up with the slower ones interacting sooner, close to the equator. At the foot of the field line the precipitating electrons in a range of energies can arrive at nearly the same time after interacting with the wave in a field aligned region extending several thousand kilometers on both sides of the equator. The precipitation flux pulse can be found by summing the contributions of all segments of the interaction region, at each instant of time.

In order to find the energy flux as a function of the time that the electrons arrive at the foot of the field line, it is necessary to model the momentum change of each electron which resonates with the wave. This requires that the electron distribution in energy and pitch angle be known. A numerical technique of following the momentum perturbations of a significant sample of particles in order to determine the loss cone flux (e.g. Inan, 1977) is usually costly in terms of computer time. In this report we have considered only the temporal shape of the energy flux pulse and not the magnitude. Our approach has been to normalize the loss cone energy flux contribution of each segment along the field line by the loss cone energy flux resulting from interactions at the equator. Normalized scattering efficiency coefficients are introduced to study how the pulse shape is affected by wave growth and an energy dependence in the duration of resonance interactions. The latter term is found to have little effect on the pulse shape for a distribution which diminishes as the square of the electron energy. Wave growth, on the other hand is found to have a pronounced effect on the shape of the pulse. When a constant amplitude wave scatters electrons with equal efficiency everywhere along the path, the energy flux at either end of the field line resulting from direct or mirrored precipitation has been found to have a general shape described by a slow rise and fast decay. If the wave grows in amplitude as it propagates along the field line, then the slowly rising leading edge of the precipitation pulse will be less apparent and the general shape will become more symmetric, showing both a fast rise and decay.

We also have considered the effect on the pulse shape of varying

the duration of the interacting wave train. Increasing the duration of the wave causes an increase in the relative magnitude of the precipitation flux since more segments of the interaction region are contributing at the same time. When all segments of the interaction region are contributing to the total flux, then the magnitude of the precipitation energy flux will saturate, provided that the reservoir of electrons available for scattering into the loss cone has not been appreciably depleted by previous interactions. For the L=4.2 field line when N_{eq}=100 cm^{-3}, saturation occurs after about 1 second for the direct mode of precipitation and after about 2 seconds for the mirrored mode.

The arrival time model allows us to compare for the first time the predicted shape and mean arrival time of the energy flux pulse due to the direct and mirrored modes of precipitation at conjugate ends of the field line. In general, the direct mode produces more sharply defined energy flux pulses. For the mirrored mode, the precipitating electrons must traverse a longer path, resulting in a greater spread between those of high and low energies. The mean arrival times predicted for precipitation at the wave injection site, as shown in figure 2.6, will be substantially different for the direct and mirrored modes. At the conjugate point (i.e. wave echo site), however, the combinations of wave and particle travel times result in nearly the same mean arrival times for the direct and mirrored modes. This means that observed precipitation at the wave echo site often may not be unambiguously identified as resulting from only one mode. At the wave injection site this ambiguity does not exist.

The new method of calculating the mean arrival time of the energy

flux pulse has provided us with a tool to examine correlation events involving VLF waves and effects of electron precipitation. A comparison of the results of the model to time delays observed between the arrival of the waves and particles can readily tell us whether cyclotron resonant pitch angle scattering in the equatorial region is a plausible explanation of the effect. It also can help us to distinquish between the direct and mirrored modes for precipitation at the wave injection site.

In chapter 3 we have compared several correlated events with the mean arrival times predicted by the model. the January 2, 1971 x-ray events correlated with whistler-triggered emissions were found by Rosenberg et al. (1971) to be the result of the mirrored mode of precipitation. The direct mode was discounted because of an absence of correlated VLF events at the conjugate end of the field line. Although the correlation was made at the wave echo site where the arrival time model has shown that it is often difficult to distinguish between mean arrival times for the direct and mirrored modes, the low electron densities along the path at that time tended to maximize the time differences predicted by the model for the two modes. While the model results for the mirrored case showed good agreement with the observations, those for the direct mode were about 400 milliseconds out of agreement. The model thus adds support to the mirrored mode of precipitation suggested by Rosenberg et al. (1971).

The model was also applied to the July 24, 1977 photometer events correlated with whistlers at Siple station. Earlier modeling (Helliwell et al., 1980) which calculated electron arrival times but not the energy

flux, had suggested that the mirrored mode of precipitation couldn't explain the data because of an apparently large spread in arrival times for that case. The normalized energy flux computation in the present model includes a realistic energy distribution function. High energy electrons make a smaller contribution to the total precipitation energy flux than low energy ones because they are fewer in number. Our reevaluation of the July 24, 1977 correlation shows that both the direct or mirrored modes of precipitation are in agreement with the observations.

At the wave injection site the mean arrival times for the direct and mirrored modes should be widely separated. In an attempt to correlate optical emissions with bursts of VLF noise at the wave injection site, a photometer was installed at Roberval, Quebec. Photometric events correlated with whistlers were detected during a 90 minute period on August 30, 1979 (Doolittle, 1980). The time of arrival of the precipitating electrons relative to the time the wave was launched by a lightning strike showed conclusively for each event that the precipitation occurred by the direct mode.

In the introductory chapter we have considered various techniques which can be used to detect wave-induced electron precipitation. The minimum energy flux thresholds for detection by each method have been compiled from the literature and are listed for comparison in table 1.2. We have for the first time determined the energy flux threshold for detecting wave-induced electron precipitation by monitoring perturbations in the phase of a high frequency radar signal.

In order to examine the effect of precipitation on an HF radar

signal, we have modeled the perturbation in the ionospheric density profile which would result from loss cone fluxes of 1.0 keV electrons believed to be typical of wave-induced scattering events. The model ionosphere program computes the electron and ion density profiles in height by solving the continuity, heat and momentum transfer equations simultaneously. An additional term is included in the production function to account for corpuscular ionization.

If a continuous flux of precipitating electrons falls on the ionosphere, the electron density at a given height will initially increase due to the additional source of ionization. Eventually, however, the loss processes of recombination, diffusion and transport will balance the increased production and a steady state will be reached. The rate of ionization buildup increases with an increase in energy flux. At the height of maximum production for 1 keV electron precipitation (170 km), we find that the time constants of ionization buildup for fluxes of 0.001, 0.01 and 0.1 erg cm^{-2} s^{-1} are about 27, 15 and 5 minutes, respectively.

During the recovery period following a precipitation event, the enhancement in the ionospheric density profile decays at a rate which depends on the instantaneous value of the local density. For enhancements caused by 1 keV electron precipitation, the decay at 170 km is found to proceed faster than the normal diurnal rate following sunset. This difference is explained by the fact that ionization caused by a monoenergetic beam will be more localized in height than that caused by solar EUV radiation. Ionization losses due to diffusion are dependent on the density gradient and will therefore be greater when the

profile has localized enhancements.

The effect of wave-induced precipitation on the group path of an HF radar signal reflecting in the ionosphere is discussed in chapter 5. While the group path tends to be an insensitive means of detecting transient bursts of small (0.1 erg cm^{-2} s^{-1}) fluxes, our modeling results show that long enduring events can cause sufficient density enhancements to be detectable in a sequence of ionograms. The virtual height of reflection will be lowered as the density along the path of propagation increases. When the precipitation causes a localized increase in the vertical gradient of the density profile, then a cusp may begin to develop in the ionogram. As the precipitation continues, the cusp will be seen at progressively higher frequencies, as shown in figure 5.6.

A more sensitive technique of measuring changes in the propagation characteristics of the ionosphere is provided by monitoring the phase of an HF signal. We have simulated the temporal change in phase due to precipitation by using the ionospheric model to generate a sequence of density profiles. At each step in time the phase is determined through integration of the phase path for a given frequency. A pulse of precipitation is found to cause an immediate retardation of the phase. If the flux continues for a long time, the ionization buildup will saturate and the phase will stabilize.

Perturbations in the phase of an HF signal caused by wave-induced electron precipitation will occur against a background of phase fluctuations due to other causes. A review of the literature describing the components of variations in the background phase is compiled in

table 6.1. The background phase fluctuations are found to generally occur at periods longer than the 1 to 15 seconds duration of typical precipitation bursts. It should therefore be possible to filter out the slower variations when searching phase data for the precipitation effect. The shortest fluctuation period shown in table 6.1 is 30 seconds, giving a rate of background phase variation of 12 degrees per second. We have assumed that the slowest rate of phase retardation due to precipitation which could be directly observed against the fluctuating background is about three times that, or 45 degrees per second.

A reduction in the magnitude of the precipitation flux will result in a slower rate of phase retardation, as can be seen in figure 6.4. For a monoenergetic beam of 1 keV electrons, our simulation results show that precipitation fluxes greater than about 0.002 erg cm^{-2} s^{-1} should be detectable by the phase monitoring technique. We have therefore shown that in comparison to other methods listed in table 1.2, HF radar phase measurements provide one of the most sensitive ground based means for detecting low energy electron precipitation.

B. Suggestions for Future Work

The relative arrival times of VLF waves and precipitating electrons observed on three occasions have been compared in chapter 3 with the times predicted by the model developed in chapter 2. The comparisons show that the observed time delays are consistent with precipitation by the direct mode to the wave injection site and by the mirrored mode to the wave echo site. In each of these modes the scattering occurs during

the first pass of the wave through the equatorial region. It is understandable that echoes of a VLF wave might be less effective in scattering electrons into the loss cone since the amplitude will diminish with each successive hop unless wave growth along the path is greater than the reflection losses. While the data reviewed suggest that the first hop waves may be most important for causing precipitation, many more cases should be examined to determine whether scattering is also observed in correlation with the echoes.

Simultaneous observations of wave-induced precipitation effects at both ends of the Siple-Roberval field line could be used to check an asymmetry in conjugate mirror heights suggested by Barish and Wiley (1971). Conjugate observations also could remove the ambiguity as to whether precipitation at Siple Station may result from the second pass of the wave through the interaction region (Helliwell et al., 1980).

VLF navigation and communication transmitters are usually much more powerful than the experimental transmitter at Siple Station. In a preliminary study, Inan (1981) has computed spatial contours of the expected precipitation energy flux in the vicinity of VLF transmitters NAA (Cutler, Me.), NPG (Jim Creek, Wa.), NSS (Annapolis, Md.) and OMEGA (N.D.). Although optical emissions of the type correlated with whistlers have not yet been seen in correlation with the Siple transmitter, it is reasonable to suppose that the greater power of the utility VLF stations may cause photometrically observable light enhancements. A future experiment, therefore would be to operate a photometer in the vicinity of such a utility transmitter site to search for this effect.

The ionospheric model described in chapter 4 solves the heat equation at each step in time to determine the electron and ion temperatures. Wave-induced electron precipitation will introduce an additional source of heat production in the thermal computations. It has been assumed in the modeling undertaken thus far that the ionospheric heating is negligible during a typical (15<seconds, <0.1 erg cm^{-2} s^{-1}) precipitation burst. The heat production term due to precipitation has therefore been omitted in order to simplify the calculations. For long enduring precipitation, however, ionospheric heating may slightly alter the model density profile. Future modeling could include heat production in order to quantify the effect.

Another minor factor not included in the nighttime ionospheric model is ionization due to EUV radiation back-scattered by particles in the geocorona (i.e. sunlit space surrounding the earth). While the additional production from this source is certainly small compared to daylight EUV radiation, it may contribute significantly to the nighttime density profile in the lower E region (Voss and Smith, 1977). The nighttime ionization due to back-scattered EUV could be introduced into the simulations by including an additional production term in the continuity equation. The production from back-scattered EUV will be nearly constant on the time scale of the burst-like precipitation events.

The ionospheric effects examined in this report have resulted from precipitation of a narrow gaussian (i.e. monoenergetic) distribution of electrons with a characteristic energy of 1 keV. The height of peak ionization for 1 keV electrons occurs at about 170 km. Higher energy

electrons will penetrate further into the atmosphere and will result in an ionization enhancement at a lower height. The existing simulation program could be used to examine ionospheric modification caused by precipitating electrons with energies up to about 10 keV. Electrons with energies greater than 10 keV will penetrate into the D region which is below the lower boundary of the model.

By assuming that the beam of precipitating electrons is monoenergetic we have simplified the computations to obtain a first order calculation of the magnitude of the ionization enhancement. A refinement of our modeling procedure could be made by specifying the energy spectrum of the precipitation flux. The total corpuscular ionization rate $q(h_i)$ at each step in height could then be calculated by integrating over all energies the product of the distribution function $f(E)$ and a function $g(E,h)$ describing the energy dependence of the ionization rate per unit incident flux.

$$q(h_i) = \int_E f(E)\ g(E,h)\ dE$$

Values of the latter function for a range of energies at any height could be found by using the analysis discussed in the appendix.

The ionospheric modeling of ionization enhancements due to wave-induced electron precipitation have thus far only been done for the nighttime case. A similar study could be made for the daytime case to determine whether the effect is detectable by HF radar measurements. The increased ionospheric densities during the daytime will tend to diminish the relative magnitude of a density enhancement caused by a

precipitation flux. The question of detectability, however, cannot be answered without calculating the magnitude of the density profile enhancement since daytime background temporal variations in the phase of fixed frequency HF radar echoes will also be less.

The variations in the phase of HF radar echoes have typical periods ranging from several seconds to several hours. Fourier analysis could be used to determine the spectral components of the phase variations in sequences of fixed frequency HF radar data. By applying the method to a large volume of data, it would be possible to statistically determine the rate of occurrence of various components of phase fluctuation under conditions of magnetic quiet and disturbance during both day and night.

Appendix

HEIGHT PROFILES OF CORPUSCULAR IONIZATION RATE

The ionization rates (cm^{-3} s^{-1}) per unit incident flux (cm^{-2} s^{-1}) have been calculated as a function of altitude by Banks et al. (1974) for selected monoenergetic electron beams with energies of $0.42 \leq E_0 \leq 10$ keV. Their approach used an extended Fokker-Planck method to determine the distribution in energy along the path into the atmosphere. The ionization rate height profiles for several energies are shown in figure 4.3. The profiles for intermediate energies can be found through interpolation. In this section we describe the interpolation scheme used in the model discussed in chapter 4.

An approximation of the corpuscular ionization rate height profile can be made by assuming that its shape is given by a function of the type used by Chapman (1931) to describe the ionization rate profile which results from solar radiation. The corpuscular ionization rate will then be described by

$$Q = \exp\left[Y_1 + 1 - z - \exp(-z)\right] \qquad \text{A.1}$$

where Y_1 defines the production rate at the peak of ionization and z is the distance above the height (Y_2) of the peak measured in units of the scale height (H), as given by

$$z = \frac{h - Y_2}{H}$$

The scale height is assumed to follow a quadratic variation with true height, such that

$$H = Y_3 + Y_4 h + Y_5 h^2$$

The corpuscular ionization rate per unit incident flux at any height (h) can be found by specifying values for Y_1, Y_2, Y_3, Y_4 and Y_5. These will depend on the initial energy of the precipitating electrons and can be obtained through interpolation between values of the coefficients associated with the several profiles published by Banks et al. (1974). Table A.1 lists the coefficients obtained by fitting equation A.1 to the profiles of figure 4.3 using the method of least squares.

Table A.1

Coefficients of production function
for selected monoenergetic electron beams

E_0 (keV)	Y_1	Y_2	Y_3	Y_4	Y_5
0.42	-13.80	247	-37.0	0.435	-0.000670
0.8	-12.70	182	-34.0	0.420	-0.000660
2	-11.30	132	-33.5	0.387	-0.000627
5	- 9.44	114	-25.2	0.303	-0.000519
10	- 8.81	105	-14.7	0.201	-0.000304

The coefficients at intermediate energies are found by interpolating in table A.1. An alternate approach would be to derive analytical expressions for each of the coefficients by fitting least

square polynomials to the tabulated values. A Fortran subroutine is shown in table A.2 which accepts a given height and electron initial kinetic energy and returns the corpuscular ionization rate ($cm^{-3}\ s^{-1}$) per unit incident flux ($cm^{-3}\ s^{-1}$). The routine calls a further subroutine (NTRP) which performs a cubic spline interpolation to find the coefficients needed to solve equation A.1. Examples of profiles at energies of 0.5 and 1.0 keV found using the subroutine are plotted as dashed curves in figure 4.3.

Table A.2

Subroutine to find ionization rate
for a given height and initial energy

```
      SUBROUTINE COLION (H,E,Q)
C     GIVEN HEIGHT H (KM) AND INITIAL ENERGY E (KEV), FIND IONIZATION
C     RATE Q (PER CM**3 PER SEC) PER UNIT INCIDENT FLUX (PER CM**2 PER SEC).
      COMMON/BLK1/YE1,YE2,YE3,YE4,YE5
      COMMON/BLK2/EØ
      DIMENSION EØ(5),YE1(5),YE2(5),YE3(5),YE4(5),YE5(5)
      DATA YE1/-13.8,-12.7,-11.3,-9.44,-8.81/
      DATA YE2/247.,182.,132.,114.,1Ø5./
      DATA YE3/-37.,-34.,-33.5,-25.2,-14.7/
      DATA YE4/Ø.435,Ø.42Ø,Ø.387,Ø.3Ø3,Ø.2Ø1/
      DATA YE5/-Ø.ØØØ67Ø,-Ø.ØØØ66Ø,-Ø.ØØØ627,-Ø.ØØØ519,-Ø.ØØØ3Ø4/
C
C
      CALL NTRP (EØ,YE1,E,Y1,5)
      CALL NTRP (EØ,YE2,E,Y2,5)
      CALL NTRP (EØ,YE3,E,Y3,5)
      CALL NTRP (EØ,YE4,E,Y4,5)
      CALL NTRP (EØ,YE5,E,Y5,5)
C
C
      Z=(H-Y2)/(Y3+Y4*H+Y5*H*H)
      Q=EXP(Y1-1.-Z-EXP(-Z))
      RETURN
      END
```

REFERENCES

Agy, V., D.M. Baker and R.M. Jones, Studies of solar flare effects and other ionospheric disturbances with a high frequency Doppler technique, NBS Technical note 306, 1965.

Angerami, J.J., A whistler study of the distribution of thermal electrons in the magnetosphere, Tech. Rep. No. 17, Radioscience Laboratory, Stanford Electronics Laboratories, Stanford University, Stanford, Calif., 1966.

Angerami, J.J., and D.L. Carpenter, Whistler studies of the plasmapause in the magnetosphere, 2, Equatorial density and total tube electron content near the knee in magnetospheric ioization, J. Geophys. Res., 71, 711, 1966.

Antoniadis, D.A., Determination of thermospheric quantities from ionospheric radio observations using numerical simulation, Tech. Report No. 18, Radioscience Laboratory, Stanford Electronics Laboratories, Stanford University, Stanford, Calif., 1976.

Baker, D.M., and K. Davies, Waves in the ionosphere produced by nuclear explosions, J. Geophys. Res., 73, 448-451, 1968.

Banks, P.M., Ion temperature in the upper atmosphere, J. Geophys. Res., 72, 3365, 1967.

Banks, P.M., and A.F. Nagy, Concerning the influence of elastic scattering upon photoelectron transport and escape, J. Geophys. Res., 75, 1902, 1970.

Banks, P.M., and G. Kockarts, Aeronomy, Academic Press, New York, Chapter 22, 1973.

Banks, P.M., C.R. Chappell, and A.F. Nagy, A new model for the Interaction of auroral electrons with the atmosphere: spectral degradation, backscatter, optical emissions, and ionization, J. Geophys. Res., 79 (10), 1459-1470, 1974.

Barish, F.D., and R.E. Wiley, Worlds contours of conjugate mirror locations, J. Geophys. Res., 75, 6342, 1970.

Bates, D.R., The auroral spectrum and its interpretation, Physics of the Upper Atmosphere, edited by J.A. Ratcliffe, Academic Press, New York and London, pp. 307-310, 1960.

Bernhardt, P.A., C.G. Park, and P.M. Banks, Depletion of the F2-region ionosphere and the protonosphere by the release of molecular hydrogen, Geophys. Res. Letters, 2, 341, 1975.

Booker H.G., J.A. Ratcliffe and D.H. Shinn, Diffraction from an irregular screen with applications to ionospheric problems, Phil. Trans. Royal Soc. of London, 242, 579, 1950.

Breit, G., and M.A. Tuve, A test of the existance of the conducting layer, Phys. Rev., 28 (3), 554-573, Sept. 1926.

Budden, K.G., The Wave-Guide Mode Theory of Wave Propagation, Logos Press, 1961.

Carpenter, D.L., Whistler evidence of a "knee" in the magnetospheric ionization density profile, J. Geophys. Res., 68, 1675, 1963.

Carpenter, D.L., Whistler studies of the plasmapause in the magnetosphere; temporal variations in the position of the knee and some evidence on plasma motions near the knee, J. Geophys. Res., 71, 693-709, 1966.

Carpenter, D.L., Ogo 2 and 4 VLF observations of the asymmetric plasmapause near the time of SAR arc events, J. Geophys. Res., 76, 3644, 1971.

Carpenter, D.L., F. Walter, R.E. Barrington and D.J. McEwen, Alouette 1 and 2 observations of abrupt changes in whistler rate and of VLF noise variations at the plasmapause: a satellite-ground study, J. Geophys. Res., 73(9), 2929-2940, 1968.

Carpenter D.L., J.C. Foster, T.J. Rosenberg, and L.J. Lanzerotti, A subauroral and mid-latitude view of substorm activity, J. Geophys. Res., 80 (31), 4279-4286, 1975.

Chamberlain, J.W., Physics of the Aurora and Airglow, Academic Press, New York and London, 1961.

Chan, K.L., and O.G. Villard, Jr. Sudden frequency deviations induced by solar flares, J. Geophys. Res., 68, 3197-3224, 1963.

Chapman, S., The absorption and dissociative or ionizing effect of monochromatic radiation in an atmosphere on a rotating earth, Proc. Phys.Soc., 43, 26, 1931.

Chappell, C.R., K.K. Harris, and G.W. Sharp, Ogo 5 measurements of the plamasphere during observations of stable auroral red arcs, J. Geophys. Res., 76, 3257, 1971.

Crank, J., and P. Nicolson, A practical method for numerical evaluation of solutions of partial differential equations of the heat-conduction type, Proc. Camb. Phil. Soc., 43, 50, 1947.

da Rosa, A.V., Thermal behavior of the ionosphere and observations of the exosphere and the ionosphere by means of distant earth satellites, Tech. Report No. 2, Radioscience Laboratory, Stanford Electronics Laboratories, Stanford University, Stanford, Calif., 28-37, 1965.

da Rosa, A.V., The theoretical time-dependent behaviour of the ionospheric electron gas, J. Geophys. Res., 71, 4107, 1966.

Davidson, G., and M. Walt, Loss cone distributions of radiation belt electrons, J. Geophys. Res., 82, 48, 1977.

Davies, K., Ionospheric Radio Propagation, NSB Monograph 80, 1965.

Davies, K. and J.E. Jones, Three-dimensional observations of traveling ionospheric disturbances, J. Atmos. Terr. Phys., 33, 39-46, 1971.

Dingle, B., and D.L. Carpenter, Electron precipitation induced by VLF noise bursts at the plasmapause and detected at conjugate ground stations, J. Geophys. Res., 86, 4597-4606, 1981.

Donat, H., H. Reme, and J. M. Bosqued, Interaction des electrons avec l'atmosphere, application au cas d'une aurore diffuse, Ann. Geophys., 27, 1, 1971.

Doolittle, J.H., Photometrically detected precipitation bursts at the conjugate point of Siple Station, Antarctic Journal, 15 (5), 207, 1980.

Doolittle, J.H., W.C. Armstrong, J.P. Katsufrakis and D.L. Carpenter Wave-induced particle precipitation effects at Siple Station, Antarctic Journal, 13 (4), 204, 1978.

Eckersley, T.L., Coupling of the ordinary and extraordinary rays in the ionosphere, Proc. Phys. Soc. (London), 63 (361B), 49-58, 1950.

Fehsenfeld, F.C., A.L. Schmeltekopf, and E.E. Ferguson, Some measured rates for oxygen and nitrogen ion-molecule reactions of atmospheric importance, including $O^+ + N_2 \rightarrow NO^+ + N$, Planet. Space Sci., 13, 219, 1965.

Foster J.C., and T.J. Rosenberg, Electron precipitation and VLF emissions associated with cyclotron resonance interactions near the plasmapause, J. Geophys Res., 81 (13), 2183-2192, 1976.

Foster, J.C., T.J. Rosenberg and L.J. Lanzerotti, Magnetospheric conditions at the time of enhanced wave-particle interactions near the plasmapause, J. Geophys. Res., 81 (13), 2175-2181, 1976.

Grun, A.E., Lumineszenz, photometrische messungen der energie absorption in strahlungsfeld von elektronenquellen eindimensionaler fall in luft, Z. Naturforsch., 12a, 89, 1957.

Hamlin, D.A., R. Karplus, R.C. Vik, and K.M. Watson, Mirror and azimuthal drift frequencies for geomagnetically trapped particles, J. Geophys. Res., 66, 1, 1961.

Hargreaves, J.K. and R.D. Sharp, Electron precipitation and ionospheric radio absorption in the auroral zones, Planet. Space Sci., 13, 1171, 1965.

Helliwell, R.A., Whistlers and Related Ionospheric Phenomena, Stanford University Press, Stanford, Calif., 1965.

Helliwell, R.A., A theory of discrete VLF emissions from the magnetosphere, J. Geophys. Res., 72., 4773, 1967.

Helliwell, R.A., J.P. Katsufrakis and M.L. Trimpi, Whistler-induced amplitude perturbation in VLF propagation, J. Geophys. Res., 78, 4697-4688, 1973.

Helliwell, R.A., and J.P. Katsufrakis, VLF wave injection into the magnetosphere from Siple Station, Antarctica, J. Geophys. Res., 79 (16), 2511, 1974.

Helliwell, R.A., S.B. Mende, J.H. Doolittle, W.C. Armstrong and D.L. Carpenter, Correlations between 4278 Angstrom optical emissions and VLF wave events observed at L=4 in the Antarctic, J. Geophys. Res., 85, 3376-3386, 1980.

Herman, J.R., and S. Chandra, The influence of varying solar flux on ionospheric temperatures and densities: a theoretical study, Planet. Space Sci., 17, 815, 1969.

Hunter, D.M., F.E. Roach and J.W. Chamberlain, A photometric unit for the airglow and aurora, J. Atmos. Terr. Phys., 8, 345, 1956.

Inan, U.S., Non-linear gyroresonant interactions of energetic particles and coherent VLF waves in the magnetosphere, Tech. Report No. SEL-77-026, Radioscience Lab., Stanford Electronics Labs., Stanford, Calif., 1977.

Inan, U.S., A preliminary study of particle precipitation induced by VLF transmitter signals, Tech. Rep. No. E477-1, Radioscience Laboratory, Stanford University, Stanford, Calif., 1981.

Inan, U.S., T.F. Bell, D.L. Carpenter and R.R. Anderson, Explorer 45 and Imp 6 observations in the magnetosphere of injected waves from the Siple Station VLF transmitter, J. Geophys. Res., 82, 1177, 1977.

Inan, U.S., T.F. Bell, and R.A. Helliwell, Nonlinear pitch angle scattering of energetic electrons by coherent VLF waves in the magnetosphere, J. Geophys. Res., 83, 3235, 1978.

Johnson, C.Y. Ion and neutral composition of the ionosphere, Annals of the ISQY, 5, 1969.

Jones, A.V., Aurora, D. Reidel Publ. Co., Dordrecht, Holland, 105, 1974.

Kelso, J.M., Radio Ray Propagation in the Ionosphere, McGraw-Hill, New York, 1964.

Laasonen, P., Uber eine methode zur losung der warmeleitungsgleichung, Acta Math., 31, 309, 1949.

Lewis, H.W., Multiple scattering in an infinite medium, Phy. Rev., 78, 526, 1950.

Maeda, K., Diffusion of low energy auroral electrons in the atmosphere, J. Atmos. Terr. Phys., 27, 257, 1965.

Mantas, G.P., Electron collision processes in the ionosphere, Aeronomy Report No. 54, Aeronomy Laboratory, Department of Electrical Engineering, University of Illinois, 1973.

Mitra, A.P., A review of D-region processes in non-polar latitudes, J. Atmos. Terr. Phys., 30, 1065, 1968.

Munro, G. H., Traveling ionospheric disturbances in the F region, Australian J. Phys., 11, 91, 1958.

Nagy, A.F., and P.M. Banks, Photoelectron fluxes in the ionosphere, J. Geophys. Res., 75, 6260, 1970.

Nagy, A.F., W.B. Hanson, R.J. Hoch, and T.L. Aggson, Satellite and ground observations of a red arc, J. Geophys. Res., 77, 3613, 1972.

Omholt, A., The Optical Aurora, Springer-Verlag, Heidelberg, 1971.

Park, C.G., Methods of determining electron concentrations in the magnetosphere from nose whistlers, Tech. Rept. No. 3454-1, Radioscience Lab., Stanford Electronics Labs., Stanford University, Calif., 1972.

Park, C.G., and P.M. Banks, Influence of thermal plasma flow on the mid-latitude nighttime F2 layer: Effects of electric fields and neutral winds inside the plasmasphere, J. Geophys. Res., 79, 4662, 1974.

Park, C.G., and P.M. Banks, Influence of thermal plasma flow on the daytime F2 layer, J. Geophys. Res., 80, 2819, 1975.

Paul, A.K., J.W. Wright and L.S. Fedor, The interpretation of ionospheric radio drift measurements, IV. Angle-of-arrival and group path (echolocation measurements from digitized ionospheric soundings: The group path vector, J. Atmos. Terr. Phys., 36, 193-214, 1974.

Pierce, J. A., Intercontinental frequency comparison by very low frequency radio transmissions, Proc. IRE, 45, 798, 1957.

Poeverlein, H., Strahlwege von radiowellen in der ionosphare II, Z. Angew. Phys., 1(11), 517-525, 1949.

Raghuram, R., T.F. Bell, R.A. Helliwell and J.P. Katsufrakis, Echo-induced suppression of coherent VLF transmitter signals in the magnetosphere, J. Geophys. Res., 82, 2787-2796, 1977.

Ratcliffe, J.A., An introduction to the ionosphere and magnetosphere, Cambridge University Press, London, 1972.

Ratcliffe, J.A., and K. Weekes, Physics of the Upper Atmosphere, edited by J.A. Ratcliffe, Academic Press, New York, 377, 1960.

Rees, M.H., Auroral ionization and excitation by incident energetic electrons, Planet. Space Sci., 11, 1209-1218, 1963.

Rees, M.H., Auroral electrons, Space Sci. Rev., 10, 413-441, 1969.

Rees, M.H., and D. Luckey, Auroral electron energy derived from ratio of spectroscopic emissions, 1, model computations, J. Geophys. Res., 79, 5181, 1974.

Richtmeyer, R.D., Difference methods for initial value problems, Interscience, New York and London, 96-109, 1957.

Roble, R.G., The calculated and observed diurnal variation of the ionosphere over Millstone Hill on 23-24 March 1970, Planet. Space Sci., 23, 1017-1033, 1975.

Rosenberg, T.J., R.A. Helliwell, and J.P. Katsufrakis, Electron precipitation associated with discrete very low freqency emissions, J. Geophys. Res., 76, 8445, 1971.

Rosenberg, T.J., J. Bjordal, H. Trefall, G.J. Kvifte, A. Omholt and A. Egeland, Correlation study of auroral luminosity and x-rays, J. Geophys. Res., 76, 122, 1971a.

Rosenberg, T.J., J.C. Siren, D.L. Matthews, K. Marthinsen, J.A. Holtet, A. Egeland, D.L. Carpenter and R.A. Helliwell, Conjugacy of electron microbursts and VLF chorus, J. Geophys Res., 86, 5819-5832, 1981.

Row, R.V., Evidence of long-period acoustic-gravity waves launched into the F region by the Alaskan earthquake of March 28, 1964, J. Geophys. Res., 71, 343-345, 1966.

Rydbeck, O.E.H., Magneto-ionic triple splitting of ionospheric waves, J. Appl. Phys., 21 (12), 1205-1214, 1950.

Schield, M.A., and L.A. Frank, Electron observations between the inner edge of the plasma sheet and the plasmasphere, J. Geophys. Res., 75, 5401, 1970.

Smith, R.L., The use of nose whistlers in the study of the outer iono sphere, Tech. Rep. No.6, Radioscience Laboratory, Stanford Electronics Laboratories, Stanford University, Stanford, Calif., 77-82, 1960.

Spencer, L.V., Theory of electron precipitation, Phys. Rev., 98, 1597, 1955.

Spiegel, M.R., Schaum's Outline of Theory and Problems of Statistics, 89-91, McGraw-Hill, New York, 1961.

Spitzer, L., Jr., Physics of fully ionized gases, Interscience, 1962.

Stadsnes, J., and B. Maehlum, Scattering and absorption of fast electrons in the upper atmosphere, Internal Report, Norw. Def. Res. Estab., Kjeller, Norway, 1965.

Stein, J.A. and J.C.G. Walker, Models of the upper atmosphere for a wide range of boundary conditions, J. of Atmos. Sci., 22, 11 (1965).

Stiles, G.S., and R.A. Helliwell, Stimulated growth of coherent VLF waves in the magnetosphere, J. Geophys. Res., 82 (4), 523, 1977.

Stolarski, R.S., Analytic approach to photoelectron transport, J. Geophys. Res., 77, 2862, 1972.

Stubbe, P., Temperature dependence of the rate constants for the reactions $O^+ + O_2 \rightarrow O_2^+ + O$ and $O^+ + N_2 \rightarrow NO^+ + N$, Planet. Space Sci., 17, 1221, 1969.

Thorne, R.M., Wave-particle interactions in the magnetosphere and ionosphere, Rev. Geophys. Space Phys., 13, 291, 1975.

Waldman, H., Coupling between the ionosphere and the protonosphere and its implications on the long-term variations of the ionospheric electron content, Tech. Report No. 13, Radioscience Laboratory, Stanford Electronics Laboratories, Stanford University, Stanford, Calif., 1971.

Walker, J.C.G., Analytic representation of upper atmosphere densities based on Jacchia's static diffusion models, J. Atmos. Sci.,22, 462, (1965).

Walt, M., W.M. MacDonald, and W.E. Francis, Penetration of auroral electrons into the atmosphere, Physics of the Magnetosphere, edited by R.L. Carovillano, D. Reidel, Dordrecht, Netherlands, pp. 534-555, 1969.

Westerlund, L.H., The auroral electron energy spectrum extended to 45 eV, J. Geophys. Res., 74, 351, 1969.

Whitten, R.C., and I.G. Poppoff, Ion kinetics in the lower ionosphere, J. Atmos. Sci., 21, 117, 1964.

Wright, J.W., Some current developments in radio systems for sounding ionospheric structure and motions, Proc. IEEE, 57, 481-486, 1969.

Wright, J.W., Horizontal drifts accompanying large vertical motions of the nocturnal F region, Planet. Space Sci., 19, 1327-1337, 1971.

Wright, J.W., The interpretation of ionospheric drift measurements, VII. Diffraction methods applied to E region echo fading: Evidence of a focusing model, J. Atmos. Terr. Phys., 36, 721-740, 1974.

Voss, H.D., and L.G. Smith, Energetic particles and ionization in the nighttime middle and low latitude ionosphere, Aeronomy Rep. No. 78, Aeronomy Laboratory, University of Illinois, Urbana, Illinois, 1977.